12-2018

Utilizing Converter-Interfaced Sources for Frequency Control with Guaranteed Performance in Power Systems

Yichen Zhang
University of Tennessee, yzhan124@vols.utk.edu

To the Graduate Council:

I am submitting herewith a dissertation written by Yichen Zhang entitled "Utilizing Converter-Interfaced Sources for Frequency Control with Guaranteed Performance in Power Systems." I have examined the final electronic copy of this dissertation for form and content and recommend that it be accepted in partial fulfillment of the requirements for the degree of Doctor of Philosophy, with a major in Electrical Engineering.

Kevin Tomsovic, Seddik Djouadi, Major Professor

We have read this dissertation and recommend its acceptance:

Yilu Liu, Xiaopeng Zhao, Joe Chow

Accepted for the Council:
Carolyn R. Hodges

Vice Provost and Dean of the Graduate School

(Original signatures are on file with official student records.)

Utilizing Converter-Interfaced Sources for Frequency Control with Guaranteed Performance in Power Systems

A Dissertation Presented for the

Doctor of Philosophy

Degree

The University of Tennessee, Knoxville

Yichen Zhang

December 2018

To my family

Acknowledgments

I would like to express my deepest appreciation and gratitude to my academic co-advisors Dr. Kevin Tomsovic and Dr. Seddik Djouadi for their time and dedication, great guidance and support during my study. Their noble scientific research spirits have deeply reshaped my thinkings and behaviors. Their constant support and persistency to solve problems from new perspectives and to bring novel insights established a life goal for me, brought me into the world of research, inspired me to perform better research and to dream beyond my limitations. Moreover, with their wonderful personality they always understood and supported me in my academic experience and personal life.

My acknowledgments also go to my committee, Dr. Yilu Liu, Dr. Xiaopeng Zhao and Dr. Joe Chow for their support, guidance, helpful comments and suggestions. I also would like to thank Dr. Hector Pulgar-Painemal and Dr. Donatello Materassi for their invaluable discussions. I am also thankful to Dr. Jin Dong, Dr. Alexander Melin, Dr. Mohammed Olama and Dr. Guodong Liu from Oak Ridge National Laboratory for providing me ideas, help and support. I am very thankful to CURENT for providing me an amazing atmosphere and facilities to conduct my research. In addition, I would like to thank my colleagues and friends for the camaraderie and their assistance in research and personal life. Particularly, I would like to thank my officemate M. Ehsan Raoufat, who has been sitting aside with me for five years and provided me numerous help.

And last but not least, I would like to express my appreciation and love to my family for their unconditional love and support, which made it possible for me to finish this work.

Science cannot solve the ultimate mystery of nature. And that is because, in the last analysis, we ourselves are a part of the mystery that we are trying to solve.

- by Max Planck

Abstract

To integrate renewable energy, converter-interfaced sources (CISs) keep penetrating into power systems and degrade the grid frequency response. Control synthesis towards guaranteed performance is a challenging task. Meanwhile, the potentials of highly controllable converters are far from fully developed. With properly designed controllers the CISs can not only eliminate the negative impacts on the grid, but also provide performance guarantees.

First, the wind turbine generator (WTG) is chosen to represent the CISs. An augmented system frequency response (ASFR) model is derived, including the system frequency response model and a reduced-order model of the WTG representing the supportive active power due to the supplementary inputs.

Second, the framework for safety verification is introduced. A new concept, region of safety (ROS), is proposed, and the safe switching principle is provided. Two different approaches are proposed to estimate the largest ROS, which can be solved using the sum of squares programming.

Third, the critical switching instants for adequate frequency response are obtained through the study of the ASFR model. A safe switching window is discovered, and a safe speed recovery strategy is proposed to ensure the safety of the second frequency dip due to the WTG speed recovery.

Fourth, an adaptive safety supervisory control (SSC) is proposed with a two-loop configuration, where the supervisor is scheduled with respect to the varying renewable penetration level. For small-scale system, a decentralized fashion of the SSC is proposed under rational approximations and verified on the IEEE 39-bus system.

Fifth, a two-level control diagram is proposed so that the frequency of a microgrid satisfies the temporal logic specifications (TLSs). The controller is configured into a scheduling level and a triggering level. The satisfaction of TLSs will be guaranteed by the scheduling level, and triggering level will determine the activation instant.

Finally, a novel model reference control based synthetic inertia emulation strategy is proposed. This novel control strategy ensures precise emulated inertia by the WTGs as opposed to the trial and error procedure of conventional methods. Safety bounds can be easily derived based on the reference model under the worst-case scenario.

Table of Contents

List of Tables

List of Figures

Chapter 1

Introduction

The work in this dissertation is inspired by complex behaviors introduced by the multi-mode converter-interfaced devices (CIDs) in the time scale of seconds. As such devices keep penetrating into the power networks, the induced complex behaviors have more significant impact on power system dynamics, and particularly, the frequency response. Control synthesis towards guaranteed performance is a challenging task. Meanwhile, the potentials of highly controllable converters are far from fully developed under current control approaches. With properly designed controllers, the CIDs can not only eliminate the negative impacts on the grid, but also provide performance guarantees. This dissertation aims at establishing systematic frameworks for controller synthesis towards guaranteed performance and focuses on the frequency control problem.

This chapter first describes the background and motivation in Section 1.1 and 1.2, respectively, followed by the outline of this dissertation in Section 1.3 and the main contributions in Section 1.4.

1.1 Background

The power electronic converters have become a bridge between unified power systems and diverse fashions of sources and loads. They are highly controllable because of the fast regulating time and flexible programmability whereby desired functionalities can be integrated. The converter-interfaced sources (CISs) like wind turbine and photovoltaic

generators are mostly controlled as current sources (also known as the grid-feeding mode) and operate at the maximum power point tracking (MPPT) mode. They are required to switch to the grid-supporting modes like the inertia emulation after major disturbances [65]. On the other hand, a CIS can be controlled as a voltage source (also known as the grid-forming mode) to provide frequency and voltage regulations in weak networks and microgrids [90]. Varieties of droop control modes [103] as well as the virtual synchronous generator (VSG) mode [56] have been developed. In addition, the point of load converters (POLCs) in motor drives, computer power supplies, and compact fluorescent lighting typically make the load behaviors to be constant power, which contributes to the voltage instability. Compensation topologies such as the power buffer [111] and the electric spring [95] have been integrated in the POLCs to stabilize the grid during events and meet safe load operation requirements. These multi-mode CIDs have altered the characteristics of traditional power systems, among which the frequency response has changed dramatically.

1.1.1 Traditional Frequency Control and Response

Frequency of power systems represents the active power balance between generations and loads, and is determined by the rotating speed of synchronous generators. Traditionally, frequency regulations are accomplished purely by synchronous generators. A feedback loop is built that uses the frequency measurement to adjust the output of the synchronous generator so that the power balance can be met. In this case, the frequency response is mainly determined by the parameters of the synchronous generators and their frequency control loops. Based on time scales, frequency response can be categorized into three periods, i.e., inertial response, primary control response and secondary control response. The inertial and primary control responses have a similar time scale of seconds, while the secondary control response has a slower time scale, which is tens of seconds to minutes. Thus, the secondary control response is out of scope of this dissertation and will not be discussed.

- Inertial response. When a power imbalance occurs, the kinetic energy stored in synchronous generators or motor loads transfers automatically into electric power due to the electromagnetic coupling. The transferred electric power is denoted as

the inertial response. Physically, the combined moment of inertia of the synchronous machine and turbine governs the energy transfer rate, and thus, mainly determines the rate of change of frequency (ROCOF) after a disturbance. In power system analysis, the inertia characteristics is represented by the inertia constant, defined as the kinetic energy in watt-seconds at rated speed divided by the VA base, which mathematically serves as the time constant of the swing equation. The inertial response occurs within the very first few seconds following a change in the system frequency.

- Primary control response. The primary control is responsible for demand-supply balance following a large disturbance and ensures the synchronous machines operate at constant speed. It is denoted as electric power from all resources that eliminates the imbalance. The primary response can be provided by governors within generators as well as loads. A governor is a local feedback controller that senses the frequency and acts on the prime mover of the generator. It receives the mechanical output reference from a proportional feedback control, which defines the variation in power output in steady state with respect to a variation in frequency and is known as the droop. Interruptible load resources can improve the primary response by disconnecting from the grid when the frequency reaches a pre-defined value [10]. The primary response is mainly determined by the proportional gain and the dynamics of the governors and turbines. It becomes increasingly dominant as the mechanical inputs increase.

1.1.2 Current Status Under Increasing Renewable Penetration

Inadequacy

As traditional plants have been partially replaced by wind, photovoltaic and other alternative sources, frequency response has degraded, particularly in areas with high levels of penetration. The response discussed here is specifically referred to the transient period, that is, the period before frequency achieves steady state. In most CISs, the inherent electromagnetic couplings are either fairly weak, such as the double fed induction machine (DFIM)-based wind turbine generator (WTG) [67], or totally decoupled, like the full converter-based WTG [58], which results in the reduction of the system inertia. For example,

during the year 2012, several occasions took place in Germany where around 50% of overall load demand was covered by wind and photovoltaic units for a few hours. The regional inertia within the German power system dropped to dramatically lower levels than usual due to the temporary lack of rotating masses connected to the system [106].

Decline in the primary control response has been observed in the Eastern Interconnection of the United States. North American Electric Reliability Council (NERC) has defined the primary control response (NERC Glossary 7) mathematically as the net change in a balancing area's net actual interchange for a change in interconnection frequency, denoted as β and measured in MW/0.1Hz. Theoretically, it should be increasing with the increase of load and generation. Since 1994, the Eastern Interconnection β has declined roughly 20 percent even though it should have been increasing in proportion to a 20 percent increase in customer demand [70]. It is partially due to the deployments of renewable sources as they normally operate at the maximum or near-maximum output, which allows little or no headroom for the under-frequency response.

Inadequacy of frequency response is mainly referred to noncompliance with minimum ROCOF constraints associated with generators ROCOF relays (ROCOF inadequacy) and instantaneous minimum frequency requirements associated with under-frequency load shedding (UFLS) relays (nadir inadequacy) [16]. Currently, the latter one is of concerns as larger excursions of frequency and tie-line power may trigger unnecessary relay actions, in which case the system has adequate capacity to attain a safe steady state. This type of actions is denoted as the transient relay action in [84] and becomes more of a threat for safe and efficient operations in networks with high renewable penetration.

Variability

Intermittent outputs from renewable sources require the commitments of tradition plants to be more frequent and variable. Therefore, the inertia in a connection will become increasingly time-variant. In December 2012, based on the recorded power dispatch data in Germany, the aggregated system inertia constant is estimated to be changing from 5.5 to 3 seconds [106]. Even at the same time, different locations could have different penetration levels, and thus frequency dynamics become differently fast in individual areas. Time and

space-variant system inertia will make the availability of frequency control services more uncertain, increasing the risk of larger frequency deviations and even collapses. Contrary to the unnecessary UFLS, a UFLS relay set for high inertia situation may not arrest the decline when the current inertia is low. With continuous deployments of renewable sources, larger inertia variations will take place in shorter time windows. Situational awareness and adaptivity are of great importance for frequency control.

1.1.3 Frequency Control with Converter-Interfaced Sources

Currently, grid-supportive functions of the grid-feeding CISs to improve system frequency have been under intensive studies. Among all CISs, WTGs are preferred to be integrated with grid-supportive functions due to the large amount of available kinetic energy. Other sources will have to operate at certain de-load conditions or integrate with energy storage units. Bases on mechanisms, the existing methods can be divided into two categories, that is, supplementary signal-based approaches [18, 46, 47, 50, 53, 65] and synchronization signal-based approaches [30, 35, 120, 121].

The most common and representative method is to provide an additional signal associated with the measured grid frequency deviation or its differential to the torque/power or speed reference value to be tracked [35]. Then, the inertial response is associated with the ROCOF, which can be generated by filtering the frequency through a washout filter [46], while the synthetic primary control response corresponds to the frequency deviation. The obtained responses, however, degrade from the desired ideal ones due to low-pass filters in the loop, responding time to commands [17] and the WTG speed recovery effect [23]. Besides emulating standard responses, any pre-defined signals can be sent whereby the amount of supportive active power can be precisely controlled [47]. For off-shore wind farms connected with high-voltage direct current (HVDC) transmission networks, the energy stored in the DC-link can be combined with the kinetic energy to provide a longer support duration [39, 53].

The other type of approaches is to mimic the power-angle relation of traditional synchronous generators by means of modifying either the phase-lock loop (PLL) [30, 35] or the active power controller [120, 121]. The angle used by the Park's transformation for

synchronization is no longer obtained through the vector alignment, but calculated using the swing dynamics. Thus, inertia, load-damping effect and droop characteristics can be provided [121]. The synthetic responses obtained using this type of methods are assessable and programmable. However, since the controller has to operate at all time for CISs to maintain synchronization, it will respond to any size of disturbances and de-load from the MPPT mode.

1.2 Motivation and Objective

Although considerable numbers of approaches have been proposed, utilizing these functions towards adequate frequency response, i.e., bounded within the defined safety [1] limits for a given set of contingency events, is challenging. On the other hand, both academia [10, 84, 106] and industry [14, 16] have proposed the adequacy of frequency response as a new task, which is also the ultimate objective in this dissertation.

One of the most challenging aspects lies in the hybrid behaviors of CISs. Most CISs operate at the MPPT mode during most times for efficient energy extraction, but switch to grid-supportive modes in time during certain events to ensure response adequacy. Switchings are supervised via deadbands and other thresholds. These deadbands prevent CISs to respond to small frequency fluctuations in the grid and thus guarantee more power extraction. However, a large deadband may limit the opportunity for CISs to provide timely sufficient support during a disturbance. This is a crucial trade-off between economic and reliable operations.

The aforementioned issue leads to the two following questions: Under a certain disturbance, can the designed supportive modes preserve the desired frequency adequacy? If so, what is the largest deadband that preserves the adequacy? These questions arise from actual power system operations faced by transmission system operators (TSO) such as, the Hydro-Québec [14]. However, as pointed out in [108], the available responding time (equivalent to the deadband setting) for CISs to maintain bounded frequency response is

[1] The term *safety* is adopted from the control literature and in this context means a well-defined and allowable operating region. A safe response means the trajectories of all concerned states stays within defined safety limits.

usually unclear as illustrated in Fig. 1.1. Few methods have been proposed to answer the above questions beyond extensive simulations. On one hand, most deadband designs are not associated with varying efforts of different grid-supportive modes. On the other hand, fixed deadbands may not be able to handle a high penetration condition as the commitments of synchronous generators could change dramatically over time due to the stochastic characteristics of renewable sources. In this dissertation, reachability is introduced and a systematic framework is established to analyze and synthesize the switchings.

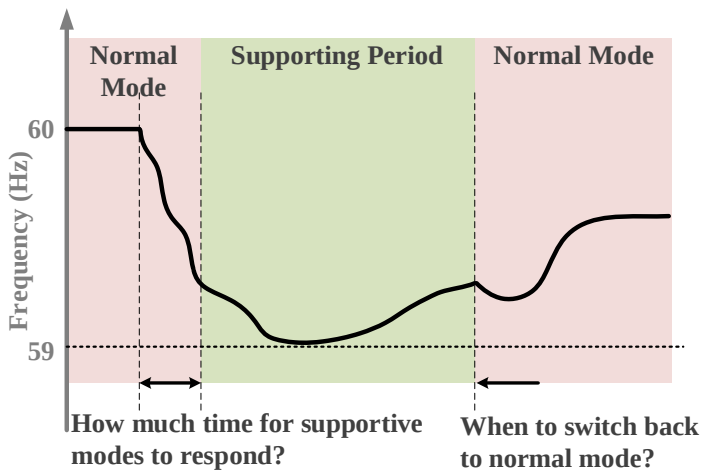

Figure 1.1: Challenges of synthesizing support modes in CIS as the switching instants between modes to achieve an adequate frequency response are still unclear.

Another challenge is that the synthetic responses are not ideal and difficult to assess. The main reason is the prime mover dynamics. Take inertia emulation using WTG as an example. Frequency measurement should be sent to the scaled differentiator $K\frac{\mathrm{d}}{\mathrm{d}t}$ whereby the ideal synthetic inertia constant will be K. However, since the transfer rate from kinetic energy to electric power in WTG is not constant due to turbine dynamics, the real emulated inertia constant degrades from K as illustrated in Fig. 1.2 and is time-varying [126]. In addition, the level of degradation depends differently on variable sources. These uncertain factors make the assessment of contribution from CIS difficult or even impossible, let alone coordination to achieve response adequacy. It is also the case for most synchronization signal based approaches as usually the prime mover dynamics are not considered [120, 121]. Thus, the question would be is there a certain control configuration such that the emulated response

can be ideal. In this dissertation, model matching techniques are proposed to address the aforementioned issues.

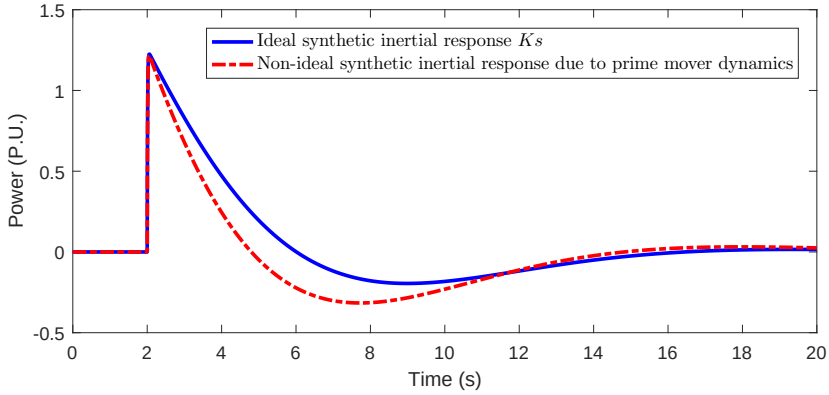

Figure 1.2: Real emulated inertial response degrades from the ideal one due to prime mover dynamics.

From the control diagram perspective, the control synthesis problems are addressed by two different means. The first one focuses on supervision or switching of a hybrid controller with known structure, including control input, to satisfy the control specifications. The second one is to design a structure, such as dynamic feedback loop, so that the generated control input completes the objective. Thus, the control design part of this dissertation is spitted into two parts: switching synthesis and input synthesis.

1.3 Dissertation Outline

This dissertation is organized in following chapters:

In Chapter 2, necessary models for frequency control are developed. The system frequency response (SFR) model and the center of inertia (COI) frequency are discussed. As a representative CIS, the WTG is selected as the actuator. An universal model reduction technique called selective modal analysis (SMA)-based model reduction is applied to the WTG. By combining the SFR model and the reduced-order model of the WTG, an augmented SFR (ASFR) is obtained. The emulated inertial and primary control responses are approximately evaluated as the corresponding coefficients in the swing equation for the purpose of intuition.

In Chapter 3, the approaches on safety verification and their applications in power systems are discussed, particularly the so-called barrier certificate method. Then, algorithmic solutions for the barrier certificate method are provided as the preliminaries.

In Chapter 4, a new concept *region of safety* (ROS) is proposed whereby the safe switching principle is concluded. The largest ROS is interpreted in the sense of the backward reachability. To estimate the largest ROS, an iterative algorithm and the occupation measure-based optimization formulation are proposed, respectively. Geometry interpretation of the occupation measure-based formulation is given. Both approaches as well as the reviewed methods are validated on a numerical example. The pros and cons of the two approaches are discussed. Based on the framework, first the switching instants (equivalent to the thresholds) for multi-mode WTGs towards response adequacy are analyzed on a single-area system. Secondly, an adaptive safety supervisory control (SSC) is proposed, which allows to accommodate a scheduling loop for robustness against variations of the system inertia. The proposed SSC is first verified on a microgrid in Simulink, and then implemented on the IEEE 39-bus system in Transient Security Assessment Tool (TSAT). Finally, the proposed controller is implemented on the Hardware Test Bed (HTB) at Center for Ultra-Wide-Area Resilient Electric Energy Transmission Networks (CURENT).

In chapter 5, a two-level control diagram is proposed so that the frequency of a diesel-wind mixed microgrid satisfies the temporal logic specifications (TLSs). The mixed integer linear programming (MILP) based model checking method is introduced so that the control problem with TLSs an be converted into a numerical optimal control (NOC) problem. The controller is configured into a scheduling level and a triggering level. In the scheduling level, a series of Boolean control signals are computed by solving the NOC problem, where the frequency response predicted by the ASFR satisfies the defined specifications under a given worse-case contingency. In addition, the scheduling level will constantly re-schedule the signal based on the operating condition and varying specifications. The triggering level will measure the frequency and detect whether a severe contingency close to the worst case is happening. Once such a contingency is detected, the scheduled signals are applied to the WTGs. Finally, the control performance is verified on the nonlinear 33-node based microgrid in Simulink.

In chapter 6, a novel model reference control (MRC) based synthetic inertia emulation strategy is proposed. The reference model is designed to have a similar structure to the frequency response model with desired inertia. Through active power measurement and state feedback, the WTG generates additional active power to guarantee that the diesel generator speed follows the frequency from the reference model. This novel control strategy ensures precise emulated inertia by the WTG as opposed to the trial and error procedure of conventional methods. This controller is also robust against parameter uncertainty. By guaranteeing performance, safety bounds can be easily derived based on the reference model under the worst-case scenario. Then, adequate response can be achieved by scheduling the inertia according to the operating point of the network. Moreover, the capability of coordinating multiple WTGs to provide required inertia under the proposed control is verified on the nonlinear 33-node based microgrid in Simulink. Finally, the proposed controller is implemented on the HTB at CURENT.

In chapter 7, the work in this dissertation is summarized and suggestions for future work is provided.

1.4 Summary of Contributions

The contributions of this dissertation are summarized as follows:

- An ASFR model is derived, where a reduced-order model of the WTG representing the supportive energy associated with the supplementary signals is incorporated. The emulated inertial and primary control responses are approximately evaluated as the corresponding coefficients in the swing equation. As a result, the equivalent inertia and load-damping constants become time-varying.

- The set theory-based safety verification is introduced to provide guidelines for multi-mode WTGs to maintain adequate frequency response. A new concept, ROS, is proposed, and the safe switching principle is interpreted. The largest ROS is explained in the sense of the backward reachability.

- Two different schemes to estimate the largest ROS are proposed. First, an iterative algorithm based on the barrier certificate theory is proposed. To further provide convergence proof, a mathematically intuitive formulation based on the occupation measure in the functional space is established. Geometry interpretation of this formulation is given. Coincident results by both methods as well as the reviewed approaches are obtained. Pros and cons of the two approaches are discussed.

- The switching instants for multi-mode WTGs to ensure adequate frequency response are obtained through the study of the ASFR model of a single-area system. A safe switching window is discovered and a safe speed recovery strategy is proposed to guarantee the safety of the second frequency dip.

- An adaptive SSC is proposed with a two-loop configuration, where the supervisor is scheduled with respect to the renewable penetration level. The SSC is enable to timely switch the WTGs to emulate inertial response and provide the real-time margin to the critical limit, that is, the remaining available time for a safe switching. The proposed controller is first verified on a single-machine three-phase nonlinear microgrid model in Simulink, and then implemented on the phasor domain IEEE 39-bus system with more than 50% renewable penetration in TSAT in a decentralized fashion. Finally, the controller is verified experimentally on the HTB at CURENT.

- The TLSs are considered in the frequency control problem. The mixed integer linear programming (MILP) based model checking method is introduced so that the control problem with TLSs is converted into a NOC problem. A two-level control diagram is proposed to accommodate the NOC problem, which cannot be solved in real time under occurrence of events. The configuration is verified on the nonlinear 33-node based microgrid.

- A novel MRC based synthetic inertia emulation strategy is proposed. This novel control strategy ensures precise emulated inertia by the WTG as opposed to the trial and error procedure of conventional methods, and is also robust against parameter uncertainty. Adequate response is achieved by scheduling the inertia according to the operating

point of the network. Moreover, the capability of coordinating multiple WTGs to provide required inertia under the proposed control is verified on the nonlinear 33-node based microgrid in Simulink. Finally, the proposed controller is implemented on the HTB at CURENT.

Chapter 2

Power System Modeling for Frequency Control

This chapter aims at establishing the mathematical models for frequency control problems. To maintain feasible computation complexity, models that are most relevant to frequency dynamics are extracted, which turn out to be the mechanical components and their corresponding controllers. The traditional SFR is discussed in Section 2.1. The WTG model and the SMA-based model reduction is presented in Section 2.2. The ASFR is derived in Section 2.3 by closing the interacting loop between the SFR and WTG whereby the support is quantified approximately. Part of the results in this chapter appeared in [126] and [110]

2.1 System Frequency Response

Frequency in power systems is governed by the rotating speed of all connected synchronous generators. During a disturbance, individual machines are retarding or accelerating at different rates. In this section, the frequency response of a single synchronous generator is discussed first. Then, the regional or systemic frequency represented by individual or group behaviors of synchronous generators are derived.

2.1.1 Synchronous Generators

A synchronous generator consists of the prime mover, turbine, speed governor, exciter and synchronous machine. In addition, it may be equipped with the automatic generation control (AGC) and power system stabilizer (PSS). Among all components, the swing motion of the electric machine, turbine and speed governor mainly determine the frequency response of a synchronous generator. The associated dynamics can be expressed using a set of simplified ordinary differential equations as follows [94]

$$\begin{aligned} \Delta\dot{\omega} &= \frac{1}{2H}(\Delta P_m - \Delta P_e) \\ \Delta\dot{P}_m &= \frac{1}{\tau_{\text{ch}}}(\Delta P_v - \Delta P_m) \\ \Delta\dot{P}_v &= \frac{1}{\tau_{\text{gv}}}(-\Delta P_v - \frac{1}{R}\Delta\omega) \end{aligned} \tag{2.1}$$

where ω is the speed of the synchronous machine and H is the inertia constant of the synchronous machine. R is the droop setting of the speed governor. τ_{ch} and τ_{gv} is the time constant of the turbine and governor, respectively. P_m, P_e and P_v are mechanical power, electric power and valve position, respectively.

The mechanical part of a synchronous machine expressed in (2.1) can be denoted as the frequency response model. The electric power variation ΔP_e reflects the demand and is regarded as the disturbance input to the equations. The frequency responses of a synchronous generator using nonlinear simulation in Transient Security Assessment Tool (TSAT) [82] and its corresponding frequency response model in the form of (2.1) are compared in Fig. 2.1. The response in blue is obtained by imposing the simulated ΔP_e on the frequency response model. As shown, the mechanical components of a synchronous generator are sufficient to represent its frequency characteristics.

In order to use the equations independent from algebraic constraints, a simplified net power change equation in [91] is employed

$$\Delta P_e = \Delta P_d + D\Delta\omega \tag{2.2}$$

where ΔP_d is the non-frequency-sensitive demand change, and $D\Delta\omega$ is the frequency-sensitive demand change. D is denoted as the load-damping effect and expressed as percent change in load divided by percent change in frequency.

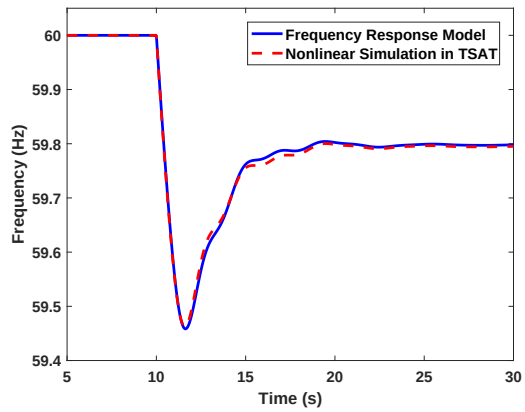

Figure 2.1: Response comparison of the frequency response model and nonlinear simulation in TSAT.

2.1.2 COI Frequency

Actually, the frequency either in a plant, a balancing authority or an interconnection is an averaged behavior of groups of generators. Regional frequency can be obtained by vertically averaging unit frequencies. This averaging eventually leads to the system frequency. During the averaging, the MVA ratings or inertia can be used as the weighting factors, leading to the MVA-weighted averaged frequency [63, 64] or the COI frequency [5, 104]. The COI frequency, or frequency at the equivalent inertial center, can be described by the so-called SFR models, which can be obtained by adding the power equations in (2.1) and (2.2) of all synchronous generators

$$\begin{aligned}
\sum_i 2H_i\Delta\dot{\omega}_i &= \sum_i \Delta P_{m,i} - \sum_i \Delta P_{d,i} - \sum_i D_i\Delta\omega_i \\
\sum_i \tau_{\mathrm{ch},i}\Delta\dot{P}_{m,i} &= \sum_i \Delta P_{v,i} - \sum_i \Delta P_{m,i} \\
\sum_i \tau_{\mathrm{gv},i}\Delta\dot{P}_{v,i} &= -\sum_i \Delta P_{v,i} - \sum_i \frac{1}{R_i}\Delta\omega_i
\end{aligned} \tag{2.3}$$

Define the following terms as

$$
\begin{aligned}
&H_c = \frac{\sum_i H_i S_i}{\sum_i S_i}, \quad \omega_c = \frac{\sum_i H_i \omega_i}{\sum_i H_i} \\
&\Delta P_M = \frac{\sum_i \Delta P_{m,i}}{\sum_i S_i}, \quad \Delta P_D = \frac{\sum_i \Delta P_{d,i}}{\sum_i S_i}, \quad \Delta P_V = \frac{\sum_i \Delta P_{v,i}}{\sum_i S_i},
\end{aligned}
\tag{2.4}
$$

where S_i is the MVA rating of synchronous generator i. The terms H_c and ω_c are denoted as the COI and COI frequency, respectively. Then, Eq. (2.3) can be further simplified as follows

$$
\begin{aligned}
&2H_c \Delta\dot{\omega}_c = \Delta P_M - \Delta P_D - \overline{D}\Delta\omega_c \\
&\overline{\tau_{\text{ch}}}\Delta\dot{P}_M = \Delta P_V - \Delta P_M \\
&\overline{\tau_{\text{gv}}}\Delta\dot{P}_V = -\Delta P_V - \frac{1}{\overline{R}}\Delta\omega_c
\end{aligned}
\tag{2.5}
$$

with unknown parameters $\overline{D}$, $\overline{R}$, $\overline{\tau_{\text{ch}}}$ and $\overline{\tau_{\text{gv}}}$, which can be calculated using the approach in [6] or estimated using measurement data. In this dissertation proposal, we assume that these parameters have been obtained. Eq. (2.5) is a typical SFR model, and can be regarded analytically as the common mode of the system.

While being ignored by the SFR model, individual machines (areas) will actually oscillate about the inertial center. The magnitude of deviation from the COI frequency is determined by the electric distance to the inertial center, which is further determined by the line impedance. Based on this fact, extra margins can be added to the safety limit to prevent the frequency of individual machines (areas) from reaching the UFLS zone. Thus, in this dissertation proposal the objective is to guarantee the adequacy of the COI frequency, which is also the research target in most related works [25, 59, 63, 64].

2.2 WTG Modeling and Model Reduction

Among all CISs, the WTGs are preferred to be integrated with grid-supportive functions due to the large amount of stored kinetic energy. Therefore, WTGs are chosen as the actuators.

2.2.1 Wind Power and Wind Turbine

The power contained in the form of kinetic energy in the wind crossing at a speed v_{wind} [m/s] and surface A_{wt} [m^2] is expressed by [1]

$$P_{\text{wind}} = \frac{1}{2}\rho \underbrace{\pi R_t^2}_{A_{wt}} v_{\text{wind}}^3 \quad [\text{W}] \tag{2.6}$$

where ρ is the air density, R_t is the radius of the wind turbine in meter and A_{wt} is the wind turbine swept area. The power extracted by the wind turbine from P_{wind} can be expressed as

$$P_M = \frac{1}{2}\rho \underbrace{\pi R_t^2}_{A_{wt}} v_{\text{wind}}^3 C_P(\lambda, \theta_t) \quad [\text{W}] \tag{2.7}$$

The term $C_P(\lambda, \theta_t)$ is the power coefficient, which is a dimensionless parameter that expresses the energy extraction efficiency of a wind turbine, and is often as a function of the tip speed ratio λ and the pitch angle θ_t [degree].

Let ω_T be the turbine speed, ω_M and ω_R be the rotor mechanical and electric speed of the electric machine, respectively, all in rad/s. Let k be the gear ratio between the turbine and the machine, p be the pole pair number of the electric machine. Then

$$\omega_R = p \times \omega_M = p \times k \times \omega_T \quad [\text{rad/s}] \tag{2.8}$$

Note that the relation in (2.8) is also the same for their bases denoted by the overline

$$\overline{\omega}_R = p \times \overline{\omega}_M = p \times k \times \overline{\omega}_T \quad [\text{rad/s}] \tag{2.9}$$

Therefore, these speeds are the same in per unit (denoted as p.u. for short)

$$\omega_r = \omega_m = \omega_t \quad [\text{p.u.}] \tag{2.10}$$

And the tip speed ratio is

$$\lambda = \frac{v_{tip}}{v_{\text{wind}}} = \frac{R\omega_T}{v_{\text{wind}}} = \frac{R\omega_R}{pkv_{\text{wind}}} = \frac{R\omega_r\overline{\omega}_R}{pkv_{\text{wind}}} \tag{2.11}$$

A common used expression for the power coefficient is [86]

$$C_p = 0.22\left(\frac{116}{\lambda_i} - 0.4\theta_t - 5\right)e^{-\frac{12.5}{\lambda_i}} \tag{2.12}$$

where

$$\lambda_i = \left(\frac{1}{\lambda + 0.08\theta_t} - \frac{0.035}{\theta_t^3 + 1}\right)^{-1} \tag{2.13}$$

The theoretical maximum value of the power coefficient is 0.593, i.e., $C_{P,\max} = 0.593$, which is the so-called Betz's limit [1].

The mechanical torque input to the electric machine reads

$$T_M = \frac{P_M}{\omega_M} \quad [\text{Nm}] \tag{2.14}$$

The ratings of the WTG in this dissertation proposal is arranged as follows. For simplicity, instead of aggregating hundreds of WTGs in a wind farm, we will use one electric machine with the desired rating and scale the wind turbine up closely to this rating as shown in Fig. 2.2.

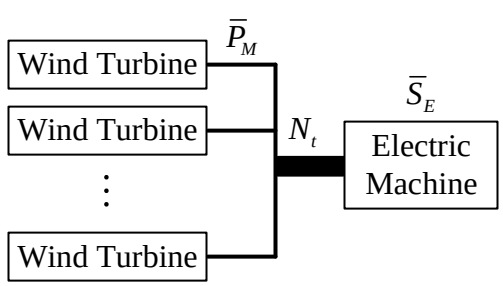

Figure 2.2: Aggregating wind turbines to an electric machine with desired rating.

It is necessary to use the electric MVA base of the machine $\overline{S}_E$ to define the torque base since $\overline{S}_E$ is the base of the swing equation where the mechanical torque in per unit appears.

The torque base for the electric machine reads

$$\overline{T} = \frac{p\overline{S}_E}{\overline{\omega}_R} \quad \text{[Nm]} \tag{2.15}$$

and the mechanical torque input from the wind turbine with respect to the electric machine base can be expressed as

$$T_m = \frac{N_t T_M}{\overline{T}} = \frac{N_t P_M}{\omega_M}\frac{\overline{\omega}_R}{p\overline{S}_E} = \frac{N_t P_M}{\overline{S}_E}\frac{\overline{\omega}_R}{p\omega_M} = \frac{N_t P_M}{\overline{S}_E}\frac{\overline{\omega}_R}{\omega_R} = \frac{N_t P_M}{\overline{S}_E}\frac{1}{\omega_r} \quad \text{[p.u.]} \tag{2.16}$$

where N_t is the scaling parameter. In addition, we have

$$T_m = \frac{P_m}{\omega_r} \quad \text{, If } \overline{S}_E = N_t\overline{P}_M \tag{2.17}$$

$$T_m = \frac{P_m}{\omega_r}\frac{N_t\overline{P}_M}{\overline{S}_E} \quad \text{, If } \overline{S}_E \neq N_t\overline{P}_M \tag{2.18}$$

where $\overline{P}_M$ is the base of a single wind turbine and usually takes the value of the nominal mechanical power output.

2.2.2 WTG Modeling

In the time scale of inertial and primary control response, the most relevant dynamics in a WTG are the induction machine and its speed regulator via the rotor-side converter (RSC). The RSC controller regulates the power output and rotor speed of the WTG simultaneously by adjusting the electromagnetic torque. Normally the frequency supportive functions are integrated within this subsystem. The grid-side converter (GSC) simply feeds the power from the RSC into the grid by regulating the DC-link voltage. The responding time of the DC voltage regulation is usually much faster than that of the RSC current loop for stability reasons. As a result, the GSC and its corresponding controller are less relevant to the frequency supportive functions, and can be omitted for theoretical studies (not in simulations) similarly in [51, 66]. In addition, the WTG can be assumed to operate at partial loaded condition, and the pitch control can be omitted.

Detailed procedures of modeling WTGs will not be described here. A fifth-order DFIM-based WTG model with parameters is given in Appendix B.1. Meanwhile, a third-order DFIM-based model adopted from [86] is used in some of the case studies, and thus given in Appendix B.2.

2.2.3 Selective Modal Analysis based Model Reduction

To reinforce the analysis in the following chapters, a reduced-order model of the WTG is derived. The SMA-based model reduction has proven to be successful in capturing the active power dynamics of WTGs [86] and is chosen for our study. Different from [86], the reduced-order model here aims at representing the effect of the supplementary control on the active power variation of WTGs.

The supplementary input u_s is assumed to be made up of the ROCOF $K_{\text{ie}}\Delta\dot{\omega}$, system frequency deviation $K_{\text{pc}}\Delta\omega$ and flexible input u_f, where K_{ie} and K_{pc} are the controller gains. The wind speed can be assumed as a fixed value during the time window of the transient frequency response, and thus its variation Δv_{wind} is equal to zero. Given Q_g^*, the differential-algebraic model of the WTG in Appendix B.1 can be linearized about an equilibrium point corresponding to a specific wind speed v_{wind}^* and terminal voltage magnitude V_s^* (also given in Appendix B.1) to obtain the linearized differential-algebraic model as follows

$$\begin{aligned} \begin{bmatrix} \Delta\dot{x} \\ 0 \end{bmatrix} &= \begin{bmatrix} A_s & B_s \\ C_s & D_s \end{bmatrix} \begin{bmatrix} \Delta x \\ \Delta y \end{bmatrix} + \begin{bmatrix} M_{s1} \\ N_{s1} \end{bmatrix} \Delta\dot{\omega} + \begin{bmatrix} M_{s2} \\ N_{s2} \end{bmatrix} \Delta\omega + \begin{bmatrix} M_{sf} \\ N_{sf} \end{bmatrix} u_f \\ \Delta P_g &= \begin{bmatrix} E_s & F_s \end{bmatrix} \begin{bmatrix} \Delta x \\ \Delta y \end{bmatrix} \end{aligned} \tag{2.19}$$

where

$$x = [\psi_{qs}, \psi_{ds}, \psi_{qr}, \psi_{dr}, \omega_r, x_1, x_2, x_3, x_4]^T \tag{2.20}$$

$$y = [v_{qr}, v_{dr}, i_{qr}, i_{dr}, P_g, Q_g, i_{ds}, i_{qs}]^T \tag{2.21}$$

Using Kron reduction on Eq. (2.19) yields the following state-space model

$$\begin{aligned} \Delta\dot{x} &= A_{\text{sys}}\Delta x + B_{\text{sys1}}\Delta\dot{\omega} + B_{\text{sys2}}\Delta\omega + B_{\text{sys}f}u_f \\ \Delta P_g &= C_{\text{sys}}\Delta x + D_{\text{sys1}}\Delta\dot{\omega} + D_{\text{sys2}}\Delta\omega + +D_{\text{sys}f}u_f \end{aligned} \tag{2.22}$$

where

$$\begin{aligned} A_{\text{sys}} &= A_s - B_s D_s^{-1} C_s & C_{\text{sys}} &= E_s - F_s D_s^{-1} C_s \\ B_{\text{sys1}} &= M_{s1} - B_s D_s^{-1} N_{s1} & D_{\text{sys1}} &= -F_s D_s^{-1} N_{s1} \\ B_{\text{sys2}} &= M_{s2} - B_s D_s^{-1} N_{s2} & D_{\text{sys2}} &= -F_s D_s^{-1} N_{s2} \\ B_{\text{sys}f} &= M_{sf} - B_s D_s^{-1} N_{sf} & D_{\text{sys}f} &= -F_s D_s^{-1} N_{sf} \end{aligned}$$

At the equilibrium point, the matrix of the participation factors, and eigenvalues of A_{sys} are shown in (2.23) and (2.24). The WTG rotor speed $\Delta\omega_r$ is closely related to its active power output, and the mode where $\Delta\omega_r$ has the highest participation would capture the relevant active power dynamics. As shown, $\Delta\omega_r$ has the highest participation at 85% in the mode

$\lambda_8 = -0.26$. Thus, this mode is selected as the most relevant mode as $\lambda_r = \lambda_8$.

$$
\begin{array}{c}
\psi_{qs} \\ \psi_{ds} \\ \psi_{qr} \\ \psi_{dr} \\ \omega_r \\ \omega_f^* \\ x_1 \\ x_2 \\ x_3 \\ x_4
\end{array}
\begin{bmatrix}
0.0008 & 0.0188 & 0.4866 & 0.4866 & 0.0000 & 0.0000 & 0.0000 & \mathbf{0.0000} & 0.0000 & 0.0000 \\
0.0181 & 0.0050 & 0.4894 & 0.4894 & 0.0000 & 0.0001 & 0.0000 & \mathbf{0.0000} & 0.0000 & 0.0000 \\
0.0013 & 0.9531 & 0.0133 & 0.0133 & 0.0003 & 0.0195 & 0.0000 & \mathbf{0.0000} & 0.0000 & 0.0000 \\
0.9698 & 0.0040 & 0.0099 & 0.0099 & 0.0113 & 0.0003 & 0.0011 & \mathbf{0.0000} & 0.0000 & 0.0000 \\
0.0000 & 0.0003 & 0.0000 & 0.0000 & 0.0000 & 0.0004 & 0.0001 & \boxed{\mathbf{0.8505}} & 0.0038 & 0.1471 \\
0.0000 & 0.0000 & 0.0000 & 0.0000 & 0.0000 & 0.0000 & 0.0000 & \mathbf{0.0025} & 0.9961 & 0.0003 \\
0.0000 & 0.0000 & 0.0000 & 0.0000 & 0.0000 & 0.0000 & 0.0000 & \mathbf{0.1470} & 0.0001 & 0.8526 \\
0.0012 & 0.0000 & 0.0000 & 0.0000 & 0.0038 & 0.0001 & 0.9973 & \mathbf{0.0000} & 0.0000 & 0.0000 \\
0.0000 & 0.0187 & 0.0005 & 0.0005 & 0.0183 & 0.9617 & 0.0000 & \mathbf{0.0000} & 0.0000 & 0.0000 \\
0.0088 & 0.0001 & 0.0003 & 0.0003 & 0.9662 & 0.0179 & 0.0015 & \mathbf{0.0000} & 0.0000 & 0.0000
\end{bmatrix}
\tag{2.23}
$$

$$
\lambda = \begin{bmatrix} -1070 & -691 & -5.45 \pm 397i & -13.5 & -13.6 & -2.68 & \mathbf{-0.26} & -0.001 & -0.05 \end{bmatrix}
\tag{2.24}
$$

Since only $\Delta\omega_r$ is considered as the most relevant state, the other states are less relevant and denoted as $z(t)$. Eq. (2.22) can be rearranged as

$$
\begin{aligned}
\begin{bmatrix} \Delta\dot{\omega}_r \\ \dot{z} \end{bmatrix} &= \begin{bmatrix} A_{11} & A_{12} \\ A_{21} & A_{22} \end{bmatrix} \begin{bmatrix} \Delta\omega_r \\ z \end{bmatrix} + \begin{bmatrix} B_{r1} \\ B_{z1} \end{bmatrix} \Delta\dot{\omega} + \begin{bmatrix} B_{r2} \\ B_{z2} \end{bmatrix} \Delta\omega + \begin{bmatrix} B_{rf} \\ B_{zf} \end{bmatrix} u_f \\
\Delta P_g &= \begin{bmatrix} C_r & C_z \end{bmatrix} \begin{bmatrix} \Delta\omega_r \\ z \end{bmatrix} + D_{\text{sys1}}\Delta\dot{\omega} + D_{\text{sys2}}\Delta\omega + D_{\text{sys}f} u_f
\end{aligned}
\tag{2.25}
$$

The less relevant dynamics are

$$
\dot{z} = A_{22} z + A_{21}\Delta\omega_r + B_{z1}\Delta\dot{\omega} + B_{z2}\Delta\omega + B_{zf} u_f \tag{2.26}
$$

And the most relevant dynamic is described by

$$
\Delta\dot{\omega}_r = A_{11}\Delta\omega_r + A_{12} z + B_{r1}\Delta\dot{\omega} + B_{r2}\Delta\omega + B_{rf} u_f \tag{2.27}
$$

In (2.27), z can be expressed by the following expression

$$\begin{aligned} z(t) = & \underbrace{e^{A_{22}(t-t_0)}z(t_0) + \int_{t_0}^{t} e^{A_{22}(t-\tau)}A_{21}\Delta\omega_r(\tau)d\tau}_{\text{response without control input}} + \underbrace{\int_{t_0}^{t} e^{A_{22}(t-\tau)}B_{zf}u_f(\tau)d\tau}_{\text{response under flexible input}} \\ & + \underbrace{\int_{t_0}^{t} e^{A_{22}(t-\tau)}B_{z1}\Delta\dot{\omega}(\tau)d\tau}_{\text{response under inertia emulation}} + \underbrace{\int_{t_0}^{t} e^{A_{22}(t-\tau)}B_{z2}\Delta\omega(\tau)d\tau}_{\text{response under primary frequency control}} \end{aligned} \tag{2.28}$$

Using the most relevant mode λ_r, $\Delta\omega_r(\tau)$ can be expressed as [86]

$$\Delta\omega_r(\tau) = c_r v_r e^{\lambda_r \tau} \tag{2.29}$$

where λ_r is the relevant eigenvalue, v_r is the corresponding eigenvector and c_r is an arbitrary constant. The accuracy of (2.29) is guaranteed by the dominant participation of $\Delta\omega_r$ in the mode λ_r, which can be used in solving the first integral in (2.28). Since A_{22} is Hurwitz and its largest eigenvalue is much smaller than λ_r, the natural response will decay faster and can be omitted. The essential reason is that A_{22} represents electro-magnetic dynamics which are faster than the electro-mechanical dynamics represented by λ_r. Then, the response without the control inputs in (2.28) will approximately equal to the forced response represented as follows

$$\underbrace{e^{A_{22}(t-t_0)}z(t_0) + \int_{t_0}^{t} e^{A_{22}(t-\tau)}A_{21}\Delta\omega_r(\tau)d\tau}_{\text{response without control input}} \approx (\lambda_r I - A_{22})^{-1}A_{21}\Delta\omega_r \tag{2.30}$$

The ROCOF $\Delta\dot{\omega}$, the stabilized frequency deviation $\Delta\omega$ are assumed to be fixed during the time window of interests, then the corresponding integrals in (2.28) are easily calculated as

$$\underbrace{\int_{t_0}^{t} e^{A_{22}(t-\tau)}B_{z1}\Delta\dot{\omega}(\tau)d\tau}_{\text{response under inertia emulation}} \approx (-A_{22})^{-1}B_{z1}\Delta\dot{\omega} \tag{2.31}$$

$$\underbrace{\int_{t_0}^{t} e^{A_{22}(t-\tau)}B_{z2}\Delta\omega(\tau)d\tau}_{\text{response under primary control}} \approx (-A_{22})^{-1}B_{z2}\Delta\omega \tag{2.32}$$

Approximating the integral associated with u_f in (2.28) as

$$\underbrace{\int_{t_0}^{t} e^{A_{22}(t-\tau)} B_{zf} u_f(\tau) d\tau}_{\text{response under flexible input}} \approx (-A_{22})^{-1} B_{zf} u_f + \delta_f u_f \tag{2.33}$$

Eq. (2.33) is obtained by first assuming the flexible input u_f as a constant and compensating the induced error by a parameter uncertainty δ_f.

Finally, the reduced-order WTG model with the control inputs is

$$\begin{aligned} \Delta\dot{\omega}_r &= A_{\text{rd}}\Delta\omega_r + B_{\text{rd1}}\Delta\dot{\omega} + B_{\text{rd2}}\Delta\omega + (B_{\text{rd}f} + \Delta_{f,B})u_f \\ \Delta P_g &= C_{\text{rd}}\Delta\omega_r + D_{\text{rd1}}\Delta\dot{\omega} + D_{\text{rd2}}\Delta\omega + (D_{\text{rd}f} + \Delta_{f,D})u_f \end{aligned} \tag{2.34}$$

where

$$A_{\text{rd}} = A_{11} + A_{12}(\lambda_r I - A_{22})^{-1} A_{21}, \quad C_{\text{rd}} = C_r + C_z(\lambda_r I - A_{22})^{-1} A_{21} \tag{2.35}$$

$$B_{\text{rd1}} = B_{r1} + A_{12}(-A_{22})^{-1} B_{z1}, \quad D_{\text{rd1}} = D_{\text{sys1}} + C_z(-A_{22})^{-1} B_{z1} \tag{2.36}$$

$$B_{\text{rd2}} = B_{r2} + A_{12}(-A_{22})^{-1} B_{z2}, \quad D_{\text{rd2}} = D_{\text{sys2}} + C_z(-A_{22})^{-1} B_{z2} \tag{2.37}$$

$$B_{\text{rd}f} = B_{rf} + A_{12}(-A_{22})^{-1} B_{zf}, \quad D_{\text{rd}f} = D_{\text{sys}f} + C_z(-A_{22})^{-1} B_{zf} \tag{2.38}$$

$$\Delta_{f,B} = A_{12}\delta_f, \quad \Delta_{f,D} = C_z\delta_f \tag{2.39}$$

Finally, one reduced-order model can be obtained as $A_{\text{rd}} = -0.27$, $C_{\text{rd}} = 0.26$. Note that the mode $\lambda_8 = -0.26$ is well preserved.

2.3 ASFR and Support Quantification

The SFR model in (2.5) can be regarded as the plant, while the reduced-order WTG model expressed in (2.34) can be regarded as the controller. Let u_f be zero for now. By closing the

loop, the ASFR model can be expressed as

$$
\begin{aligned}
2H_c\Delta\dot{\omega}_c &= \Delta P_M + k_{\text{scal}}\Delta P_G - \Delta P_D - \overline{D}\Delta\omega_c \\
\overline{\tau_{\text{ch}}}\Delta\dot{P}_M &= \Delta P_V - \Delta P_M \\
\overline{\tau_{\text{gv}}}\Delta\dot{P}_V &= -\Delta P_V - \frac{1}{\overline{R}}\Delta\omega_c \\
\Delta\dot{\omega}_r &= A_{\text{rd}}\Delta\omega_r + B_{\text{rd1}}\Delta\dot{\omega}_c + B_{\text{rd2}}\Delta\omega_c
\end{aligned}
\tag{2.40}
$$

where k_{scal} denotes a change of base if necessary and

$$
\Delta P_G = C_{\text{rd}}\Delta\omega_r + D_{\text{rd1}}\Delta\dot{\omega}_c + D_{\text{rd2}}\Delta\omega_c \tag{2.41}
$$

Having the ASFR model, it is easy to shown that the supportive power expressed in (2.41) due to the signal $\Delta\dot{\omega}_c$ and $\Delta\omega_c$ will influence the values of H_c and $\overline{D}$ independently. To evaluate the emulated inertia, the terms B_{rd2} and D_{rd2} are set to zero. The explicit forced output response of (2.41) due to $\Delta\dot{\omega}_c$ is given by

$$
\Delta P_G(t) = C_{\text{rd}}\int_{t_0}^{t} e^{A_{\text{rd}}(t-\tau)}B_{\text{rd1}}\Delta\dot{\omega}_c(\tau)d\tau + D_{\text{rd1}}\Delta\dot{\omega}_c(t) \tag{2.42}
$$

During the time window of inertia response $T_h = \{t : 0 \leq t \leq t_h\}$, the ROCOF is approximately fixed. Then, $\Delta\dot{\omega}_c$ can be pulled out of the integral. Integrating (2.42) with $t_0 = 0$ yields

$$
\Delta P_G(t) = (D_{\text{rd1}} - C_{\text{rd}}A_{\text{rd}}^{-1}(I - e^{A_{\text{rd}}t})B_{\text{rd1}})\Delta\dot{\omega}_c \tag{2.43}
$$

Substituting (2.43) back into the swing equation in (2.40) and rearranging the state yields

$$
[2H_c + 2H_e(t)]\Delta\dot{\omega}_c = \Delta P_M - \Delta P_D - \overline{D}\Delta\omega_c \tag{2.44}
$$

where

$$
H_e(t) = 0.5[-D_{\text{rd1}} + C_{\text{rd}}A_{\text{rd}}^{-1}(I - e^{A_{\text{rd}}t})B_{\text{rd1}}] \tag{2.45}
$$

To evaluate the emulated load-damping effect, the terms B_{rd1} and D_{rd1} are set to zero. The explicit forced output response of (2.34) due to $\Delta\omega_c$ is given as

$$\Delta P_G(t) = C_{\mathrm{rd}} \int_{t_0}^{t} e^{A_{\mathrm{rd}}(t-\tau)} B_{\mathrm{rd2}} \Delta\omega_c(\tau) d\tau + D_{\mathrm{rd2}} \Delta\omega_c(t) \tag{2.46}$$

After the frequency is stabilized by the governor, i.e., $t \in T_p = \{t : t_p \leq t \leq t_s\}$, the term $\Delta\omega_c$ can be pulled out of the integral. Integrating (2.47) with $t_0 = t_p$ yields

$$\Delta P_G(t) = (D_{\mathrm{rd2}} - C_{\mathrm{rd}} A_{\mathrm{rd}}^{-1} (I - e^{A_{\mathrm{rd}}(t-t_p)}) B_{\mathrm{rd2}}) \Delta\omega \tag{2.47}$$

Substituting (2.47) into the swing equation in (2.40) yields

$$2H_c \Delta\dot{\omega}_c = \Delta P_M - \Delta P_D - [D + D_e(t)] \Delta\omega_c \tag{2.48}$$

where

$$D_e(t) = -D_{\mathrm{rd2}} + C_{\mathrm{rd}} A_{\mathrm{rd}}^{-1} (I - e^{A_{\mathrm{rd}}(t-t_p)}) B_{\mathrm{rd2}} \tag{2.49}$$

Here based on the model and its operating condition in Appendix B.2, the reduced-order WTG is obtained as $A_{\mathrm{rd}} = -0.0723$ and $C_{\mathrm{rd}} = 0.0127$. B_{rd1}, D_{rd1} and B_{rd2}, D_{rd2} with the corresponding K_{ie} and K_{pc} are listed in Table 4.1. The parameters of SFR model in (2.5) are assumed to be estimated well and given in Appendix A.1. Then, the equivalent time-varying inertia and load-damping effects are shown in Fig. 2.3.

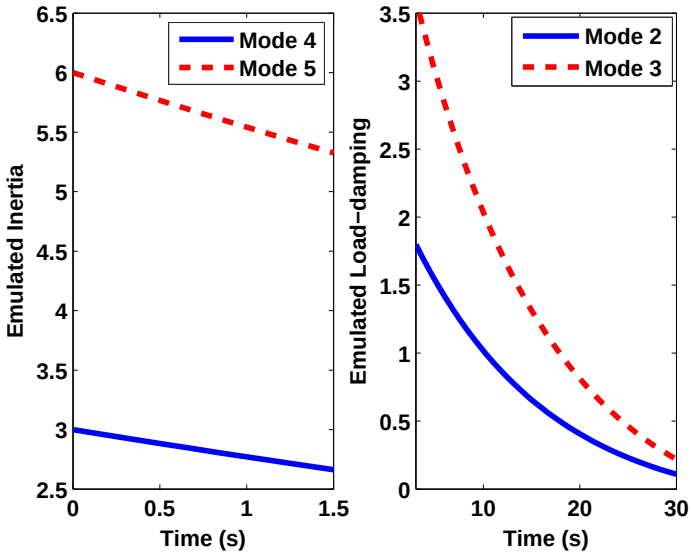

Figure 2.3: Time-varying emulated inertia and load-damping coefficient.

Part I

Switching Analysis and Supervisory Control

Chapter 3

Set Theoretic Approaches on Safety Verification

The importance of safety verification increases tremendously for modern engineering systems whose functions are safety-critical such as the transportation systems and power systems. Safety verification is to secure the evolutions of system states. Thus, most approaches are related to set theories and reachability. All set theoretic approaches can be categorized into two main groups: set operation-based methods and passivity-based methods. On the other hand, the verification can be cast either in the forward setting or the backward setting. This chapter reviews approaches in safety verification and introduces some preliminaries that will be used later.

This chapter is organized as follows. Section 3.1 reviews the set theoretic approaches on safety verification, including a passivity-based verification method: the so-called barrier certificate. Section 3.2 introduces the positivity certificates and computation techniques used by the barrier certificate.

3.1 Safety Verification

Safety denotes the property that all system trajectories stay within given bounded regions, thus, equipment damage or relay trigger can be avoided. Note this is similar, but not identical, to what is called security in power industry but for purposes of this dissertation

proposal we will assume satisfying safety conditions ensures secure operation. Consider the dynamics of a power system governed by a set of ordinary differential equations (ODEs) as

$$\dot{x}(t) = f(x(t), d(t)), \quad t \in [0, T] \tag{3.1}$$

where $T > 0$ is a terminal time, $x(\cdot) : [0, T] \to \mathbb{R}^n$ denotes the vector of state variables and $d(\cdot) : [0, T] \to \mathbb{R}^m$ denotes the vector of certain disturbances, such as, generation losses or abrupt load changes. The vector fields $f : \mathbb{R}^n \times \mathbb{R}^m \to \mathbb{R}^n$ is such that for any d and initial condition x_0, the state equation (3.1) has a unique solution defined for all $t \in [0, T]$, denoted by $\phi(t; d(t), x_0) : [0, T] \to \mathbb{R}^n$. Note that we employ a semicolon to distinguish between the arguments and the trajectory parameters.

For the verification tasks in power systems, the disturbances may be assumed to be bounded in the set $D \subseteq \mathbb{R}^m$, that is, $d(\cdot) : [0, T] \to D$. Let $X \subseteq \mathbb{R}^n$ be the computational domain of interests, $X_I \subseteq X$ be the initial set and $X_U \subseteq X$ be the unsafe set, then the formal definition of the safety property is given as follows.

Definition 3.1 (Safety)**.** *Given (3.1), X, X_I, X_U and D, the* safety *property holds if there exists no time instant $T \geq 0$ and no piecewise continuous and bounded disturbance $d : [0, T] \to D$ such that $\phi(t; d(t), x_0) \cap X_U \neq \varnothing$ for all $t \in [0, T]$ and $x_0 \in X_I$.*

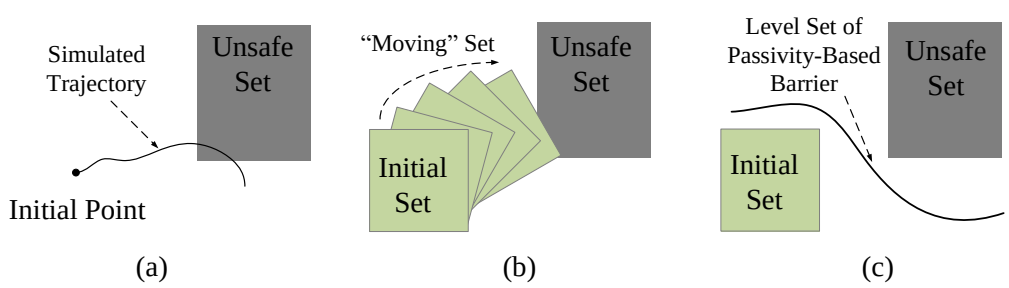

Figure 3.1: Safety verification based on (a) simulation, (b) set operating and (c) passivity.

In other words, safety verification is to ensure there is no intersection between the possible system trajectories and the given unsafe set. Three typical methods tackling this problem are illustrated in Fig. 3.1 and will be briefly introduced in this section, the last of which, the passivity-based methods, is the subject of this dissertation proposal.

3.1.1 Simulations and Alternative Simulations

If the system is assured to be at a specific operating point $\widetilde{x}_0$ and subjected to a known disturbance $\widetilde{d}$, the safety can be verified by numerical integration of (3.1) to obtain the trajectory as illustrated in Fig. 3.1 (a). In one hand, it is tremendous challenging to assure the precise operating point and measure the exact disturbance. On the other hand, system designs should aims at operations under multiple scenarios and unpredictable conditions. These factors make this problem intractable. Nevertheless, the system is known to be unsafe if one unsafe trajectory is found. Based on this observation, unsafe scenarios may be discovered by exhaustive analysis. For example, in practical power system operations exclusive simulations will be conducted in the control rooms known as the dynamic security assessment [71]. Another solution is to try to generate a finite set of trajectories that will exhibit all the behaviors of the system [28]. Rapidly-exploring random trees [13], sensitivity analysis [12] and approximate bisimulation [27] are techniques to achieve this goal.

3.1.2 Set Operation-Based Verification

Set operation-based verification can be categorized in different ways. From *execution* point of view, the set operation-based verification can be conducted using either the forward reachable sets or backward reachable sets as illustrated in Fig. 3.2 [60]. In forward verification, the reachable set of the initial set denoted by X_F is computed under the system vector fields to examine whether X_F will intersect with X_U. While, in backward verification, the reachable set of the unsafe set denoted by X_B is computed in reverse time and the intersecting condition between X_I and X_B is examined.

From *computation* point of view, there are Lagrangian and Eulerian methods [60]. Both types of methods can be executed in either forward or backward setting. Lagrangian methods work with linear systems and seek efficient over-approximation of the reachable sets. Eulerian method (also known as the level set method), which can deal with general dynamic systems, is to calculate as closely as possible the true reachable set by computing a numerical solution to the Hamilton-Jacobi partial differential equation (HJ PDE). Both methods are briefly introduced in this subsection, respectively.

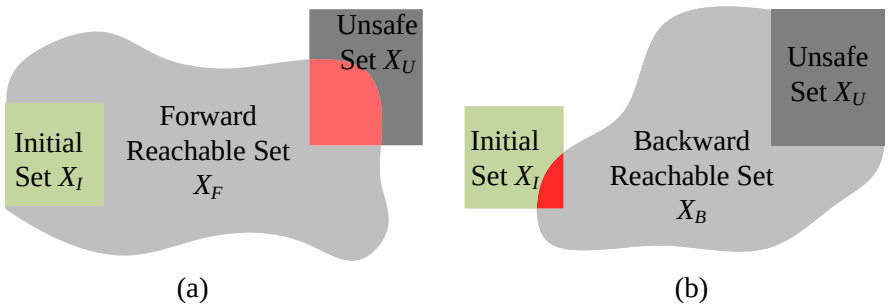

Figure 3.2: Safety verification based on (a) forward reachable set, (b) backward reachable set.

Lagrangian Methods

Lagrangian methods compute over-approximation of the reachable sets by propagating the sets under the vector fields of linear systems in efficient manners. The efficiency relies on the special representations of sets as boxes, ellipsoids, polytopes, support functions and so on. Among all representations, the ellipsoids [49] and zonotopes [26], a sub-class of polytopes, are widely-used. Applications of these techniques in power and energy systems are concluded in Table 3.1. It is worth mentioning that nonlinear differential-algebraic systems have been addressed in [3] by using the conservative linearization.

Table 3.1: Application of Lagrangian Methods in Power and Energy Systems

Reference	Technique	Topics
[36][119]	Ellipsoid	Uncertainty impact on power flow
[15]	Ellipsoid	Uncertainty impact on dynamic performance
[34]	Ellipsoid	Large-signal behavior of DC-DC converters
[115]	Ellipsoid	Locational impacts of virtual inertia on the frequency responses
[79]	Zonotope	Frequency dynamics with HVAC and HVDC transmission lines
[77][78]	Zonotope	Voltage ride-through capability of wind turbine generators
[37]	Zonotope	Uncertainty impact on power flow
[3][4][21]	Zonotope	Transient stability
[22]	Zonotope	Load-following capabilities maximization
[2]	Zonotope	Feasible ndal power injections estimation

Eulerian Methods

Strictly speaking, the Eulerian method is known as the level set method. In this method, the initial set at time t is implicitly represented by the zero sublevel sets of an appropriate function denoted by $\phi(x,t) : \mathbb{R}^n \times \mathbb{R} \to \mathbb{R}$, where the surface of the initial set at time t is expressed as $\phi(x,t) = 0$. Consider a small variation along this surface, i.e., moving (x,t) to a neighboring point $(x + dx, t + dt)$ on the surface, the variation in ϕ will be zero

$$d\phi = \phi(x + dx, t + dt) - \phi(x,t) = 0 \tag{3.2}$$

which finally leads to the HJ PDE

$$\sum_i \frac{\partial \phi}{\partial x_i} \frac{dx}{dt} + \frac{\partial \phi}{\partial t} = 0 \tag{3.3}$$

The state evolution is governed by the ODE in (3.1). Thus Eq. (3.3) is cast as follows

$$\sum_i \frac{\partial \phi}{\partial x_i} f(x,d) + \frac{\partial \phi}{\partial t} = 0 \tag{3.4}$$

This PDE describes the propagation of the reachable set boundary as a function of time under the system vector field. By solving the PDE, precise reachable sets can be obtained, and therefore this method is known as the convergent approximation [105]. Transient stability [38][101] and voltage stability [100] are analyzed using this approach. However, to obtain numerical solutions, one needs to discretize the state space, which leads to exponentially increasing computational complexity and limits its application to systems with no more than four continuous states [4].

Broadly speaking, the initial set at time t can be expressed by alternative manners, like the occupation measure in [31]. Propagating such a measure (set-valued function) will lead to the Liouville's PDE. In spirit, the type of methods is closer to the level set method, although may be in a different category from computation point of view.

3.1.3 Passivity-Based Methods

Inspired by the Lyapunov function, a barrier certificate is proposed in [83] and formally stated in the following theorem.

Theorem 3.2. *Let the system $\dot{x} = f(x, d)$, and the sets $X \subseteq \mathbb{R}^n$, $X_I \subseteq X$, $X_U \subseteq X$ and $D \in \mathbb{R}^m$ be given, with $f \in C(\mathbb{R}^{n+m}, \mathbb{R}^n)$. If there exists a differentiable function $B : \mathbb{R}^n \to \mathbb{R}$ such that*

$$B(x) \leq 0 \qquad \forall x \in X_I \tag{3.5}$$

$$B(x) > 0 \qquad \forall x \in X_U \tag{3.6}$$

$$\frac{\partial B(x)}{\partial x} f(x, d) < 0 \qquad \forall (x, d) \in X \times D \tag{3.7}$$

then the safety of the system in the sense of Definition 3.1 is guaranteed.

The function $B(x)$ satisfied the above theorem is called a barrier certificate. The zero level set of $B(x)$ defines an invariant set containing X_I, that is, no trajectory starting in X_I can cross the boundary to reach the unsafe set. It is guaranteed by the negativity of $B(x)$ over X_I and the decrease of $B(x)$ along the system vector fields. Although conditions in Theorem 3.2 is convex, it is rather conservative due to the satisfaction of (3.7) over the whole state space. A non-convex but less conservative condition is also proposed in [83] as follows.

Theorem 3.3. *Let the system $\dot{x} = f(x, d)$, and the sets $X \subseteq \mathbb{R}^n$, $X_I \subseteq X$, $X_U \subseteq X$ and $D \in \mathbb{R}^m$ be given, with $f \in C(\mathbb{R}^{n+m}, \mathbb{R}^m)$. If there exists a differentiable function $B : \mathbb{R}^n \to \mathbb{R}$ such that*

$$B(x) \leq 0 \qquad \forall x \in X_I \tag{3.8}$$

$$B(x) > 0 \qquad \forall x \in X_U \tag{3.9}$$

$$\frac{\partial B}{\partial x} f(x, d) < 0 \qquad \forall (x, d) \in X \times D \quad \text{s.t.} \quad B(x) = 0 \tag{3.10}$$

then the safety of the system in the sense of Definition 3.1 is guaranteed.

Eq. (3.10) reduces conservatism in the sense that the passivity condition only needs to hold on the zero level set of $B(x)$ instead of the whole state space. Compositional barrier certificates are discussed in [99] and [98] for verification of the interconnected systems.

By using the barrier certificate, safety can be verified without explicitly computing trajectories nor reachable sets. It has been employed in [52] and [114] to design the safety supervisor to shutdown the wind turbines in emergent conditions. Voltage constraint satisfaction with distributed generation and time-varying consumption is verified in [76].

3.2 Positivity for Barrier Certificates

The key property for the barrier certificates is to enforce positivity or non-negativity (also denoted as semi-positivity) of functions over a given set $K \subseteq \mathbb{R}^n$ as

- $p(x)$ is positive definite over a set K if and only if for any $x \in K$, $p(x) > 0$
- $p(x)$ is positive semi-definite over a set K if and only if for any $x \in K$, $p(x) \geq 0$

Any such description is called a *positivstellensatz* or *nichtnegativstellensatz*, which ends with a combination of two German words *stellen* (places) and *satz* (theorem) [74]. This is a very important problem, and a variety of efforts have been devoted to it. However, there is no general solution to prove the above property. To tackle the problem algorithmically, the classes of functions $p(x)$ have to be further restricted. A good compromise is achieved by considering the case of polynomial functions as every continuous function defined on a closed interval $[a, b]$ can be uniformly approximated as closely as desired by a polynomial function based on the Weierstrass approximation theorem.

Once confined to polynomial data, that is, the function $p(x)$ is polynomial and the set K is defined by finitely many polynomial inequalities and equality constraints (denoted as semi-algebraic sets), the problem is solvable under certain cases. In 1900, Hilbert posted a list of 23 problems, the 17th of which was: Given a multivariate polynomial that takes only non-negative values over the reals, can it be represented as a SOS of rational functions [89]? The Hilbert's 17th problem was answered by Artin in 1927 [9]. But generally the positivity of polynomials is still under intensive studies, mainly being tackled from the algebraic geometry

point of view [80]. From now on, we will use polynomials in this dissertation proposal to represent sets and approximate continuous functions. In this section, two main computation techniques are reviewed.

3.2.1 SOS Representations

Definition 3.4. *A polynomial $P(x)$ is a SOS if and only if there exist polynomials $p_1(x), \cdots, p_k(x)$ over x such that $P(x)$ can be written as*

$$P(x) \equiv p_1^2(x) + \cdots + p_k^2(x) \tag{3.11}$$

We denote a SOS polynomial as $p \in \Sigma^2[x]$. Any SOS polynomial is positive semi-definite over $\mathbb{R}^n$, while not every positive semi-definite polynomial is a SOS. A counter-example was provided by Motzkin known as the Motzkin polynomial shown as follows [89]

$$M(x_1, x_2, x_3) = x_1^4 x_2^2 + x_1^2 x_2^4 - 3x_1^2 x_2^2 x_3^2 + x_3^6 \tag{3.12}$$

which is a non-negative degree 6 polynomial and is not a SOS.

In most cases, $p_i(x)$ for $i = 1, \cdots, k$ are constructed using the monomial basis under a bounded degree. Searching for appropriate coefficients such that $P(x)$ admits a sum of squares decomposition is denoted as the SOS programming (SOSP) and can be solved by relaxation to a semi-definite program (SDP) [74, 75]. Now Theorem 3.2 can be formally solved by the following problem.

Problem 3.5. *Let $X = \{x \in \mathbb{R}^n : g_X(x) \geq 0\}$, $X_I = \{x \in \mathbb{R}^n : g_I(x) \geq 0\}$, $X_U = \{x \in \mathbb{R}^n : g_U(x) \geq 0\}$, and $D = \{d \in \mathbb{R}^m : g_D(d) \geq 0\}$, which are represented by the zero superlevel sets of the polynomials $g_X(x)$, $g_I(x)$, $g_U(x)$, and $g_D(d)$, respectively, and some*

small positive number ϵ be given. Then

$$-B(x) - \lambda_I(x)g_I(x) \in \Sigma^2[x] \tag{3.13}$$

$$B(x) - \epsilon - \lambda_U(x)g_U(x) \in \Sigma^2[x] \tag{3.14}$$

$$-\frac{\partial B}{\partial x}(x)f(x,d) - \lambda_D(x,d)g_D(d) - \lambda_X(x,d)g_X(x) \in \Sigma^2[x] \tag{3.15}$$

with multipliers $\lambda_I(x)$, $\lambda_U(x)$, $\lambda_X(x,d)$ and $\lambda_D(x,d)$ SOS polynomials.

The proof in [83] is briefly described here. Consider the formulation (3.13). Since it is a SOS, $-B(x) - \lambda_I(x)g_I(x)$ is globally nonnegative. For $x \in X_I$ ($g_I(x) \geq 0$), we have $-B(x) \geq \lambda_I(x)g_I(x) \geq 0$. Thus, Eq. (3.5) holds. Similar arguments can be used for the other conditions.

Conversion of Problem 3.5 to SDP has been implemented in solvers such as SOSTOOLS [73] or the SOS module [55] in YALMIP [54]. Then, the powerful SDP solvers like MOSEK can be employed [7].

3.2.2 Linear Representations

As an alternative to the SOS representation, another class of linear representations involves the expression of the target polynomial to be proven non-negative over the set K as a linear combination of polynomials that are known to be nonnegative over the set K. This approach reduces the polynomial positivity problem to a linear program (LP) [40][9]. Then the so-called *Handelman representations* are employed to ensure the non-negativity of a polynomial form over a region. Let K be defined as a semi-algebraic set again: $K = \{x \in \mathbb{R}^n : p_j(x) \geq 0, j = 1, 2, \cdots, m\}$. Denote the set of polynomials P as $\{p_1, p_2, ..., p_m\}$. This approach writes the given polynomial $p(x)$ as a conic combination of products of the constraints defining K, i.e., $p(x) = \lambda_f f$, where $\lambda_f \in \mathbb{R}^+$ are the coefficients, D is the bounded degree and f belongs to the following set

$$f \in \mathcal{P}(P, D) = \{p_1^{n_1} p_2^{n_2} \cdots p_m^{n_m} : n_j \leq D, j = 1, 2, \cdots, m\} \tag{3.16}$$

If the semi-algebraic set reduces into a polyhedron, that is, $p_j(x) = a_j x - b_j$, then the following conclusion known as the Handelman's Theorem provides a useful LP relaxation for proving polynomial positivity [29].

Theorem 3.6 (Handelman)**.** *If $p(x)$ is strictly positive over a compact polyhedron K, there exists a degree bound $D > 0$ such that*

$$p(x) = \sum \lambda_f f \text{ for } \lambda_f \geq 0 \text{ and } f \in \mathcal{P}(P, D) \tag{3.17}$$

An example in [9] is presented here for better illustration. Consider the polynomial $p(x_1, x_2) = -2x_1^3 + 6x_1^2 x_2 + 7x_1^2 - 6x_1 x_2^2 - 14x_1 x_2 + 2x_2^3 + 7x_2^2 - 9$ and the set $K : (x_1 - x_2 - 3 \geq 0 \wedge x_2 - x_1 - 1 \geq 0)$. Then, the positivity of p over K can be proved by representing p as follows

$$p(x_1, x_2) = \lambda_1 f_1^2 f_2 + 3 f_1 f_2 \tag{3.18}$$

where $f_1 = x_1 - x_2 - 3$, $f_2 = x_2 - x_1 - 1 \geq 0$, $\lambda_1 = 2$ and $\lambda_2 = 3$.

The general procedure is described as follows [9]:

1. Choose a degree limit D and construct all terms in $\mathcal{P}(P, D)$, where $P = \{p_1, p_2, ..., p_m\}$ are the lines defining polyhedron K.

2. Let $p(x) = \sum_{f \in \mathcal{P}(P,D)} \lambda_f f$ for unknown multipliers $\lambda_f \geq 0$.

3. Equate coefficients on both sides (the given polynomial and the Handelman representation) to obtain a set of linear inequality constraints involving λ_f.

4. Use a LP solver to solve these constraints. If feasible, the results yields a proof that $p(x)$ is positive semi-definite over K.

Remark 3.7. *Handelman's Theorem results in a LP, and thus reduces the computation burden. However, since the multipliers λ_f are real numbers instead of SOS polynomials in Putinar representation, it admits a less chance to find a Handelman representation, leaving the problem inconclusive.*

An Illustrative Example

Nevertheless, we try to employ the Handelman representation to solve Theorem 3.2 as a precursor. Similar attempt is made in [118] as well. Consider the example in [83] as follows

$$\begin{bmatrix} \dot{x}_1 \\ \dot{x}_2 \end{bmatrix} = \begin{bmatrix} x_2 \\ -x_1 + \frac{1}{3}x_1^3 - x_2 \end{bmatrix} \tag{3.19}$$

The original sets are defined as: $X = \mathbb{R}^2$, $X_I = \{x \in \mathbb{R}^2 : (x_1 - 1.5)^2 + x_2^2 \leq 0.25\}$, $X_U = \{x \in \mathbb{R}^2 : (x_1 + 1)^2 + (x_2 + 1)^2 \leq 0.16\}$. To employ the Handelman's Theorem, they are modified to be polyhedrons as shown in Fig. 3.3. The barrier certificate computed using the Handelman's Theorem is plotted as the blue curve, while the one obtained by SOSP is plotted as the dark curve. As seen, although the barrier certificates are different, both approaches successfully verify the safety of the system.

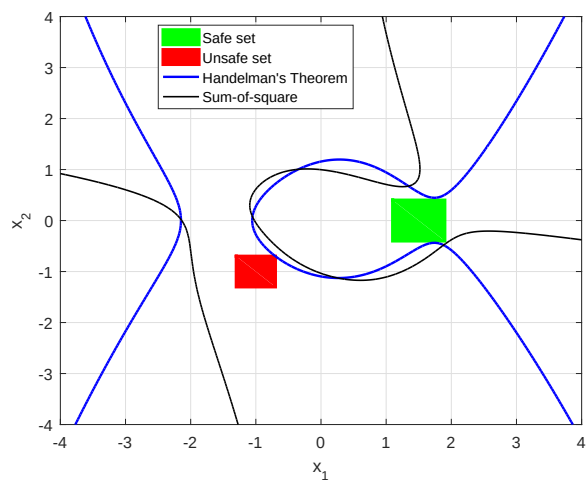

Figure 3.3: Safety verification using the Handelman representation.

Chapter 4

Hybrid Controller Synthesis

This chapter proposes the core principle and framework for switching synthesis, and at the same time provides guidelines for hybrid controller synthesis in the WTG. In section 4.1, a so-called ROS is proposed, whereby the safe switching principle is stated. In section 4.2, two different approaches are proposed to estimate the largest ROS. Section 4.3 has dual roles, which is to validate the proposed frameworks as well as to provide guidelines for hybrid controller synthesis towards adequate frequency response. Section 4.4 proposes an online safety supervisory control and is implemented on full-scale nonlinear models. Part of the results in this chapter appeared in [126] and part of the results are prepared in [125].

4.1 ROS and Safety Switching Principle

Consider the ASFR model in (2.40) in the following form

$$\Delta \dot{x}_s = A_s \Delta x_s + B_s k_{\text{scal}} \Delta P_G - B_s \Delta P_D \tag{4.1}$$

where

$$A_s = \begin{bmatrix} -\frac{\overline{D}}{2H_c} & \frac{1}{2H_c} & 0 \\ 0 & -\frac{1}{\overline{\tau}_{\text{ch}}} & \frac{1}{\overline{\tau}_{\text{ch}}} \\ -\frac{1}{\overline{R}\overline{\tau}_{\text{gv}}} & 0 & -\frac{1}{\overline{\tau}_{\text{gv}}} \end{bmatrix}, B_s = \begin{bmatrix} \frac{1}{2H_c} \\ 0 \\ 0 \end{bmatrix}$$
$$\Delta x_s = \begin{bmatrix} \Delta\omega_c, \Delta P_M, \Delta P_V \end{bmatrix}^T$$

where k_{scal} denotes a change of base if necessary. Introducing the hybrid behavior in the reduced-order model of the WTG in (2.34) yields

$$\begin{aligned} \Delta\dot{\omega}_r &= A_{\text{rd}}\Delta\omega_r + s(t-k)(B_{\text{rd1}}\Delta\dot{\omega} + B_{\text{rd2}}\Delta\omega) \\ \Delta P_G &= C_{\text{rd}}\Delta\omega_r + s(t-k)(D_{\text{rd1}}\Delta\dot{\omega} + D_{\text{rd2}}\Delta\omega) \end{aligned} \tag{4.2}$$

where $s(t-k)$ is the unit step function to describe the switching behaviors.

$$s(t-k) = \begin{cases} 0 & \text{if } t < k \\ 1 & \text{if } t \geq k \end{cases} \tag{4.3}$$

The physical component related to the switching is the deadband, the function of which is to prevent the control from responding to small fluctuations [112]. The concepual model is expressed in Fig. 4.1.

The control objective is described as follows. Consider a computation domain of interest $X \subset \mathbb{R}^n$ within the state space, which can be associated with physical system limits. Assume a power imbalance occurs at time t_0. Given the IE mode with k_{ie}, the objective of the SSC is to activate the WTG supportive mode at time $t_1 = t_0 + t_r$ so that the frequency response is adequate, i.e., $\omega \in X_S = \{x|\omega_{\text{lim}}^- \leq \omega \leq \omega_{\text{lim}}^+\} \cap X$. The set X_S is usually denoted as the *safe set*, and its complementary set is called the *unsafe set* $X_U = \{x|\omega > \omega_{\text{lim}}^+ \text{ or } \omega < \omega_{\text{lim}}^-\} \cap X$. The frequency safety limits are usually defined for a set of contingencies, i.e., $\Delta P_d \in D = \{\delta|\delta_{\text{lim}}^- \leq \delta \leq \delta_{\text{lim}}^+\}$. As seen, the most important task is to determine the reaction time t_r [109].

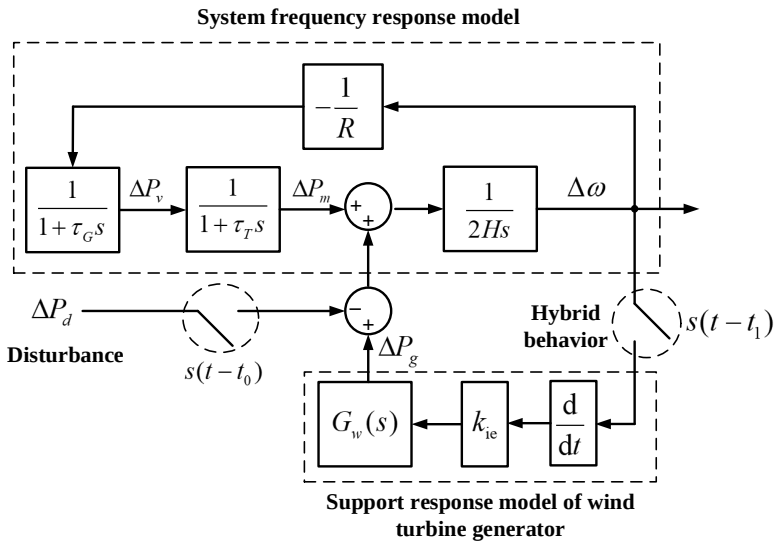

Figure 4.1: The hybrid system frequency response model incorporating the support response model of WTG. The supportive mode is limited to the inertia emulation for simplicity.

Let the hybrid closed-loop system of (4.1) and (4.2) be expressed in the compact form

$$\dot{x} = f_{t_r}(x, d) \tag{4.4}$$

Then the ROS is defined as follows.

Definition 4.1 (Region of Safety)**.** *A set that only initializes trajectories with the property in Definition 3.1 is called a region of safety.*

The *region of safety* is named analogously to the region of attraction (ROA). Both sets are collections of the initial conditions with certain properties, that is, the ROA generates stable trajectories while the ROS generates safe trajectories.

Having defined the concepts, the switching synthesis principle via the ROS can be interpreted in Fig. 4.2. Consider two extreme scenarios of the hybrid system in (4.4) when $t_r = \infty$ and $t_r = 0$, respectively. The first one presents the vector field under the MPPT mode $f_\infty(x, d)$ and the latter one denotes the supportive mode without deadband $f_0(x, d)$. Assume the ROSs under the different vector fields are calculated for $d \in D$ and shown as the green areas in Fig. 4.2. Due to the inertia emulation support, the corresponding ROS

is larger. When the system undergoes a contingency, a switching that guarantees adequate

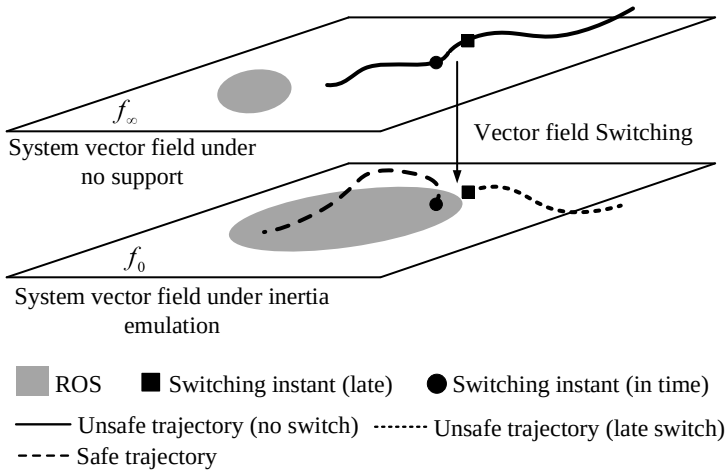

Figure 4.2: Switching principle under the guidance of ROSs for safe trajectory. The boxes are the safety limits. The green areas are the ROS of corresponding vector fields. The solid black lines are safe trajectories while the solid red ones are unsafe. The dash lines are trajectory projected onto the other vector field.

response can be committed as long as the trajectory is inside the ROS of $f_0(x, d)$. Since the states cannot jump, the trajectory after switching will be initialized within the ROS and according to Definition 4.1 it will be safe. It is worth distinguishing the ROS from the ROA in the sense that a safe trajectory may cross the boundary of the ROS. The general principle of safe switching synthesis is concluded in the following proposition [126].

Proposition 4.2. *In a hybrid system with several modes, a safe switching to mode i is guaranteed if the trajectory of the current mode belongs to the ROS of mode i. Moreover, if the ROS is represented by some sublevel set of a continuous function in terms of system states, then this function admits a safety supervisor.*

Largest ROS

It is clear that the key to appropriately supervising the mode switchings is to estimate as close as possible the largest ROS, denoted as X_I^*. The largest ROS can be explained in the sense of backward reachability. Consider the computation domain of interests X which consists of the safe set X_S and unsafe set X_U illustrated in Fig. 4.3. The true and estimated

invariant backward reachable set (BRS) of X_U is denoted as X_B^* and $\overline{X}_B$, respectively. Every trajectory starts in X_B^* will reach the unsafe set. Thus, the largest ROS is the relative complement of X_B^* with respect to X_S, i.e., $X_I^* = X_S \setminus X_B^*$. The BRS can be estimated by using the techniques introduced in Section 3.1.2, that is, either solving the HJ PDE or operating sets in the form of ellipsoids or zonotope. The two approaches will be used as comparisons and validations for the methods introduced in the following section.

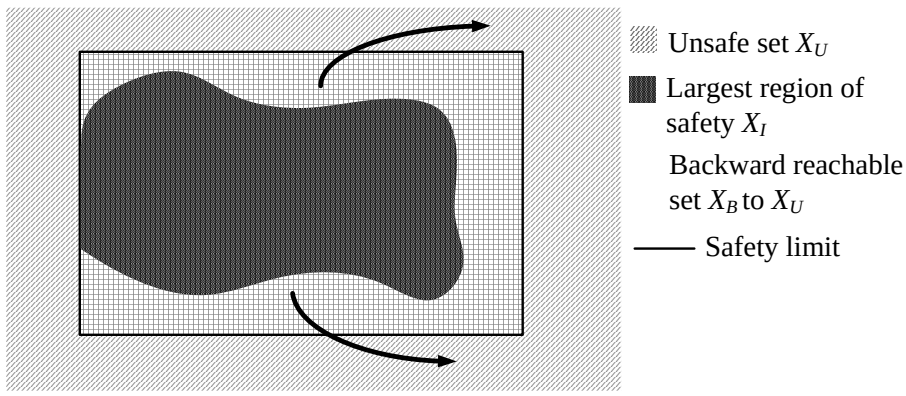

Figure 4.3: ROS interpretation in backward reachability sense.

4.2 Estimating Largest ROS

In Section 4.1, the ROS is defined and the largest ROS is interpreted from the backward reachable set point of view. Here, based on the barrier certificate approach in Theorem 3.3, we propose a conceptual optimization problem for the largest ROS as follows.

Problem 4.3. *Let $\dot{x} = f_{t_s}(x, d)$, X, X_U and D be given. The largest ROS X_I^* under the mode $t_s = 0$ can be obtained by solving*

$$\max_{X_I, B(x)} \quad Volume(X_I)$$

subject to

$$B(x) \leq 0 \quad \forall x \in X_I$$

$$B(x) > 0 \quad \forall x \in X_U$$

$$\frac{\partial B}{\partial x} f_0(x, d) < 0 \quad \forall (x, d) \in X \times D \quad \text{s.t.} \quad B(x) = 0$$

However, since the initial set X_I is a variable, Problem 4.3 becomes non-convex and cannot be solved directly. In this section, two different approaches are proposed.

4.2.1 Iterative Algorithm

Since the non-convexity is introduced by making the initial set as a variable, an iterative solution can be proposed starting by several guessed initial sets illustrated in Fig. 4.4. To

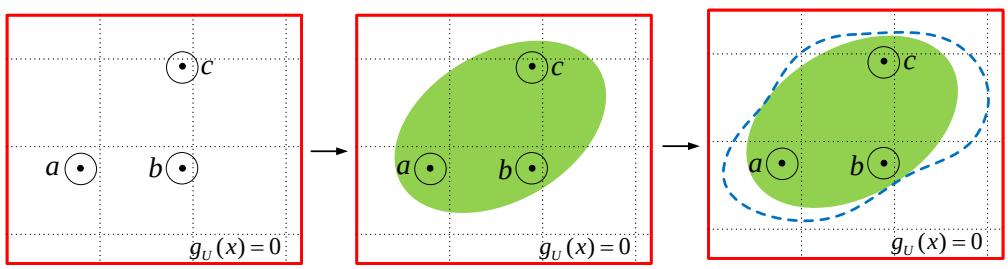

Figure 4.4: Demonstration of the iterative algorithm to estimate the largest ROS.

generate appropriate guesses, several safe trajectories can be first obtained using numerical simulations. Then, small balls can be generated around the initial points which initialize those safe trajectories. These balls can be employed as the initial sets to solve Theorem 3.3. Once a barrier certificate is obtained, its zero sublevel sets can be used as the initial set for the next iteration. Now let us introduce this algorithm formally to approximate the solution of Problem 4.3.

Algorithm 4.4. *Let* $X = \{x \in \mathbb{R}^n : g_X(x) \geq 0\}$, $X_U = \{x \in \mathbb{R}^n : g_U(x) \geq 0\}$, $D = \{d \in \mathbb{R}^m : g_D(d) \geq 0\}$, *which are represented by the zero superlevel of the polynomials* $g_X(x)$, $g_U(x)$ *and* $g_D(d)$, *respectively, some small positive number* ϵ, *initial order* $2p$ *and maximal order* $2p_{max}$ *for barrier certificate computation be given.*

- ***Initialization*** *Let* x_0^i *for* $i = 1, \cdots, N$ *be several initial points with safety verified, and* $X_{I,i} = \{x \in \mathbb{R}^n : g_{I,i}(x) \geq 0\}$ *represent a small ball centered at* x_0^i. *Choose* $\lambda_B(x, d)$ *equal to a sufficiently small positive real number* r *and solve the following*

SOS optimization for $i = 1, \cdots, N$:

$$
\begin{aligned}
-B^{(0)}(x) - \lambda_{I,i}^{(0)}(x) g_{I,i}(x) &\in \Sigma^2[x] \\
B^{(0)}(x) - \epsilon - \lambda_U^{(0)}(x) g_U(x) &\in \Sigma^2[x] \\
-\frac{\partial B^{(0)}}{\partial x}(x) f(x,d) - \lambda_D^{(0)}(x,d) g_D(d) & \\
-\lambda_X^{(0)}(x,d) g_X(x) - r B^{(0)}(x) &\in \Sigma^2[x]
\end{aligned}
$$

- ***Iteration* k**

  (a) *Fix the barrier certificate $B^{(k-1)}(x)$ from $k-1$ step, solve the SOS optimization for multiplier $\lambda_B^{(k_a)}(x,d)$:*

$$
\begin{aligned}
-\frac{\partial B^{(k-1)}}{\partial x}(x) f(x,d) - \lambda_D^{(k_a)}(x,d) g_D(d) & \\
-\lambda_X^{(k_a)}(x,d) g_X(x) - \lambda_B^{(k_a)}(x,d) B^{(k-1)}(x) &\in \Sigma^2[x]
\end{aligned}
$$

  (b) *Fix the barrier certificate $B^{(k-1)}(x)$ from $k-1$ step, the multiplier $\lambda_B^{(k_a)}(x,d)$ from k (a) step, solve the following SOS optimization for $B^{(k)}(x)$:*

$$
\begin{aligned}
-B^{(k)}(x) - \lambda_I^{(k)}(x) B^{(k-1)}(x) &\in \Sigma^2[x] \\
B^{(k)}(x) - \epsilon - \lambda_U^{(k)}(x) g_U(x) &\in \Sigma^2[x] \\
-\frac{\partial B^{(k)}}{\partial x}(x) f(x,d) - \lambda_D^{(k)}(x,d) g_D(d) & \\
-\lambda_X^{(k)}(x,d) g_X(x) - \lambda_B^{(k_a)}(x,d) B^{(k)}(x) &\in \Sigma^2[x]
\end{aligned}
$$

  (c) *If step k (b) is feasible, then let $k = k+1$. If infeasible, then increase the polynomial order of $B^{(k)}$ by two, i.e., $2p = 2p+2$. If $p = p_{max}$ but step k (b) is still infeasible, then the algorithm stops and $X_I^* = \left\{x : B^{(k-2)}(x) \leq 0\right\}$ with $B^{(k-1)}(x)$ the barrier.*

The key idea of the proposed algorithm is to use the zero level set of a feasible barrier certificate as an initial condition and to search for a larger invariant set. Once feasible, this initial condition becomes a ROS due to the existence of the corresponding barrier certificate.

A judicious choice of the initial points in the initialization step can reduce the number of iterations, and also helps to have a precise estimate in certain sub-dimensions, if a full dimensional estimate is hard due to computational complexity.

4.2.2 Occupation Measures

A recent novel approach proposed in [31, 48] uses the occupation measures to formulate the BRS computation as an infinite-dimensional LP in the space of measures. Its dual problem is formulated on the nonnegative continuous functions. Based on [31], we propose the following optimization problem.

Problem 4.5. *Let $\dot{x} = f_{t_r}(x, d)$, X, X_U and D be given. The largest ROS X_I^* under the mode $t_r = 0$ can be obtained by solving*

$$\inf_{B(x),\Omega(x)} \quad \int_X \Omega(x) d\lambda(x) \tag{4.5a}$$

$$s.t. \quad B(x) > 0 \quad \forall x \in X_U \tag{4.5b}$$

$$\frac{\partial B}{\partial x} f_0(x, d) \leq 0 \quad \forall (x, d) \in X \times D \tag{4.5c}$$

$$\Omega(x) \geq B(x) + 1 \quad \forall x \in X \tag{4.5d}$$

$$\Omega(x) \geq 0 \quad \forall x \in X \tag{4.5e}$$

where the infimum is over $B \in C^1(X)$ and $\Omega \in C(X)$. λ denotes the Lebesgue measure. If the problem is feasible, the safety $f_0(x, d)$ with $d \in D$ is preserved and the zero level set of $\Omega(x) - 1$ converges below to X_I^*.

Strict mathematical proof can be found in [31] and is out of scope of this dissertation proposal. Instead, a geometry interpretation is given. In essence, Problem 4.5 tries to estimate the BRS in Fig. 4.3 to avoid the knowledge requirement of the initial set X_I. Let any trajectory eventually ending up in the set X_U at certain time T denote as $\phi(T|x_0)$. Based on the conditions that $B(\phi(T|x_0)) > 0$ in (4.5b) and the passivity in (4.5c), one can easily have $B(x_0) > 0$. Thus, (4.5b) and (4.5c) ensure that $B(x) > 0$ for any $x \in X_B^*$ illustrated as a one dimensional case in Fig. 4.5. However, the conservatism lies in the fact

that $B(x) > 0$ for some $x \in X_I^*$, which overestimates the BRS (i.e., $X_B^* \subset \overline{X}_B$) and in turn underestimates the ROS (i.e., $X_I^* \supset \overline{X}_I$). Fortunately, this conservatism can be reduced by introducing a positive slack function $\Omega(x)$ that is point-wise above the function $B(x) + 1$ over the computation domain X in (4.5c) and (4.5d), respectively. Assume the largest ROS is represented by the indicator function $\delta_{X_I^*}(x)$, i.e., a function is equal to one on X_I^* and 0 elsewhere. The key idea of Problem 4.5 is by minimizing the area of function $\Omega(x)$ over the computation domain X, the function $B(x)+1$ will be forced to approach $\delta_{X_I^*}(x)$ from above as shown in Fig. 4.5. Thus, the zero sublevel set of $\Omega(x)-1$ is an inner approximation of X_I^*. Essentially, Problem 4.5 is trying to approximate an indicator function using a continuous function.

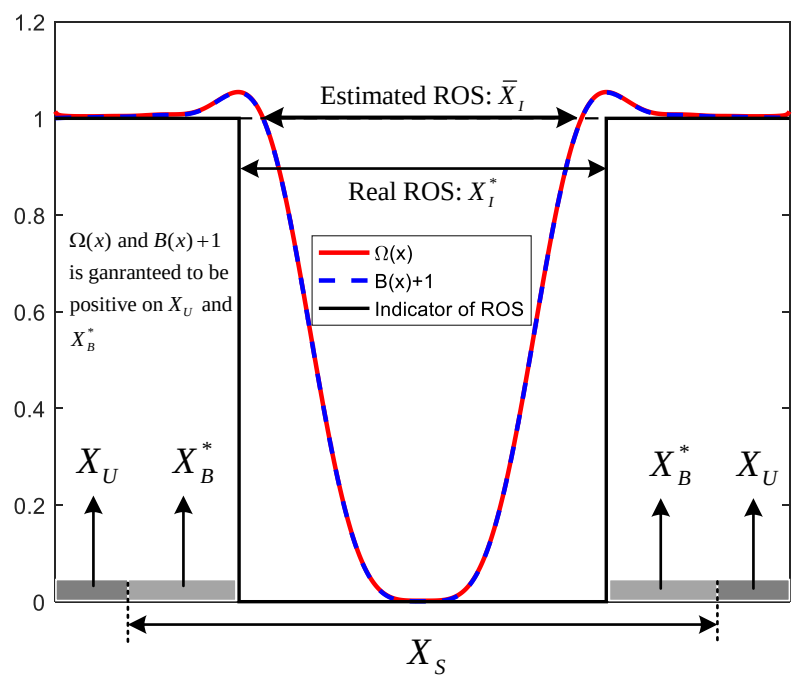

Figure 4.5: Geometry interpretation of proposed optimization problem for estimating the largest ROS.

Similarly, when equipped with polynomial data, the corresponding problem can be converted into a SOSP as follows. Conservatism of the estimation is vanishing with the increasing order of the polynomial.

Problem 4.6. *Let* $X = \{x \in \mathbb{R}^n : g_X(x) \geq 0\}$, $X_U = \{x \in \mathbb{R}^n : g_U(x) \geq 0\}$, *and* $D = \{d \in \mathbb{R}^m : g_D(d) \geq 0\}$, *which are represented by the zero superlevel set of the polynomials* $g_X(x)$, $g_I(x)$, $g_U(x)$, *and* $g_D(d)$, *respectively, and some small positive number* ϵ *be given. Functions* $B(x)$ *and* $\Omega(x)$ *are polynomials with fixed highest degree. Multipliers* $\sigma_i(x)$ *for* $i = 1, \cdots, 6$ *are SOS polynomials with fixed highest degree. Then the largest ROS can be obtained by solving the following SOS program*

$$\inf_{B(x),\Omega(x)} \omega' l \tag{4.6a}$$

$$B(x) - \epsilon - \sigma_1(x) g_U(x) \in \Sigma^2[x] \tag{4.6b}$$

$$-\frac{\partial B}{\partial x}(x) f_0(x,d) - \sigma_2(x,d) g_D(d) - \sigma_3(x,d) g_X(x) \in \Sigma^2[x] \tag{4.6c}$$

$$\Omega(x) - B(x) - 1 - \sigma_4(x) g_X(x) \in \Sigma^2[x] \tag{4.6d}$$

$$\Omega(x) - \sigma_5(x) g_X(x) \in \Sigma^2[x] \tag{4.6e}$$

where l *is the vector of the moments of the Lebesgue measure over* X *indexed in the same basis in which the polynomial* $\Omega(x)$ *with coefficients* ω *is expressed.*

For example, for a two-dimensional case, if $\Omega(x) = c_1 x_1^2 + c_2 x_1 x_2 + c_3 x_2^2$, then $\omega = [c_1, c_2, c_3]$ and $l = \int_X [x_1^2, x_1 x_2, x_2^2] \mathrm{d}x_1 \mathrm{d}x_2$.

4.2.3 Illustrations and Discussions

To further demonstrate the approaches, a simple example is illustrated. The set operation-based approaches introduced in Section 3.1.2 will be used for comparison and verification. Consider the single-machine infinite-bus system as follows

$$\begin{aligned} \dot{\delta} &= \frac{377}{\overline{\omega}} \omega \\ \dot{\omega} &= \frac{\overline{\omega}}{2H}(P_m - P_{\max} \sin\delta - \frac{D}{\overline{\omega}}\omega) \end{aligned} \tag{4.7}$$

where $\overline{\omega}$ is the speed base of the synchronous machine, H is the inertia constant, D is the load-damping effect, $P_{\max}$ is the maximum power transfer capacity, P_m is the mechanical input. The parameters are given as: ω_s=60 [Hz], $H = 3.5$ [s], D=1, $P_{\max} = 1.23$ [p.u.].

Linearizing the system about the equilibrium point of $P_m = 1$ yields the state-space model

$$\begin{bmatrix} \Delta\dot{\delta} \\ \Delta\dot{\omega} \end{bmatrix} = \begin{bmatrix} 0 & 6.2833 \\ -6.2696 & -0.1429 \end{bmatrix} \begin{bmatrix} \Delta\delta \\ \Delta\omega \end{bmatrix} \tag{4.8}$$

Define the safety specification as $X_U = \{[\delta, \omega]^T : -0.5 \leq \omega \leq 0.5\}$. First, the zonotope-based set operating method is applied in backward to find the largest backward reachable set of the unsafe set. Define an unsafe set as the red box shown in Fig. 4.6 and propagate this set in reverse time. If the computation is long enough, then an invariant set in the middle of the

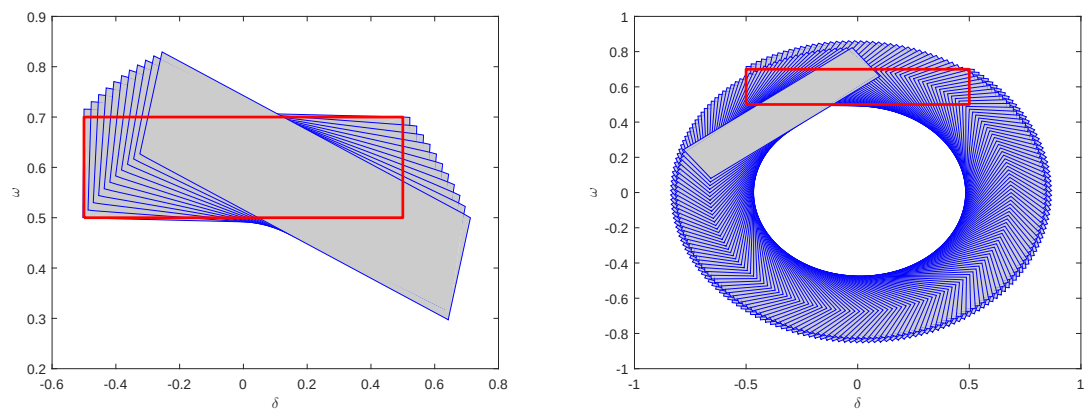

(a) **(b)**

Figure 4.6: Backward reachable set computation using zonotopes. (a) Compute for 0.05 s in reverse time. (b) Compute for 1 s in reverse time. x_1 is the rotor angle and x_2 is the machine speed.

BRS of the unsafe set is obtained, which is actually the ROS based on the interpretation of Fig. 4.3. The ROSs computed by the level set method and Algorithm 4.4 are shown in Fig. 4.7 together with the BRS via the zonotope method. The three results are in accordance with each other, and the backward reachability interpretation of the largest ROS is verified.

The results obtained by Algorithm 4.4 and Problem 4.6 are compared in Fig. 4.8. In this simple case, the two results are consistent. The zero level set of $B(x)$ solved by Problem 4.6 is enlarged by $\Omega(x) - 1$ as much as possible to the largest ROS under the fixed highest degree. With increasing dimensions of the system, higher degrees may need to obtain a convergent result from Problem 4.6. Limited by the computation complexity, Problem 4.6 sometimes

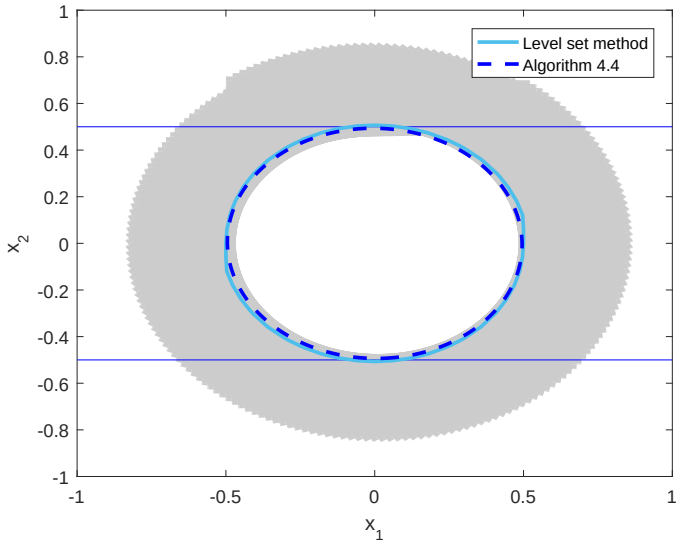

Figure 4.7: ROS computed by the level set method and Algorithm 4.4 and compared with the BRS of the unsafe set using zonotope representations.

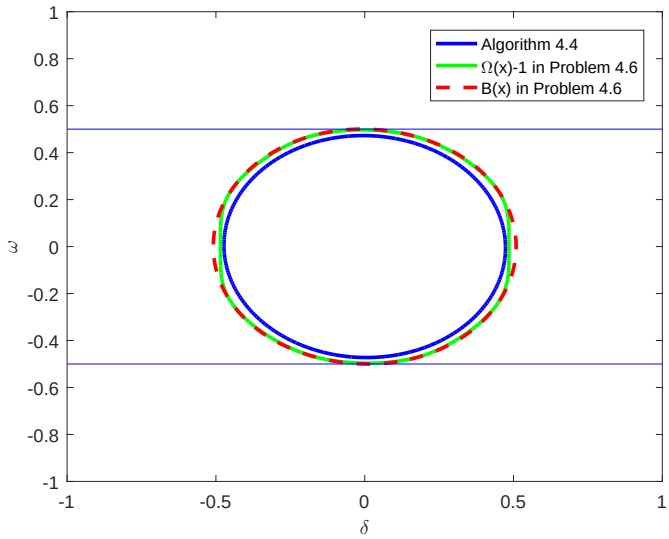

Figure 4.8: ROS computed by Algorithm 4.4 and Problem 4.6.

fails to converge. Algorithm 4.4 can always provide certain results, however, with unknown conservatism.

4.3 Supportive Modes Synthesis for WTGs

In this section, the multiple grid-supportive modes of a WTG will be synthesized. To be specific, the deadbands and other thresholds in the supplementary loop of a WTG shown in Fig. 4.9 are to be validated for adequate frequency response in a single-area system. The inertia emulation (IE) and primary frequency control (PFC) with different gains will be considered. The study in this section employs the third-order DFIM-based WTG model in Appendix B.2. All ROS computations in this section are performed using Algorithm 4.4.

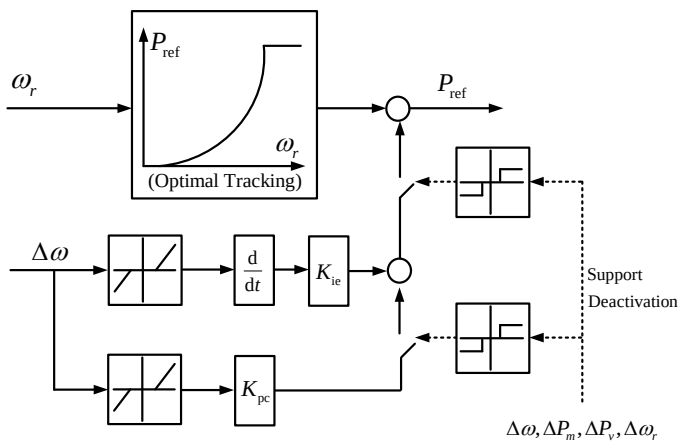

Figure 4.9: Active power control of wind turbine generator with inertia emulation and primary frequency control.

Consider the four-bus system in Fig. 4.10. Assume that the synchronous generator is a 600 MW thermal plant made up of four identical units, the frequency dynamics of which can be represented using (2.5). The parameters of (2.5) are assumed to be estimated well and given in Appendix A.1. The wind farm is assumed to be an aggregation of 200 individual

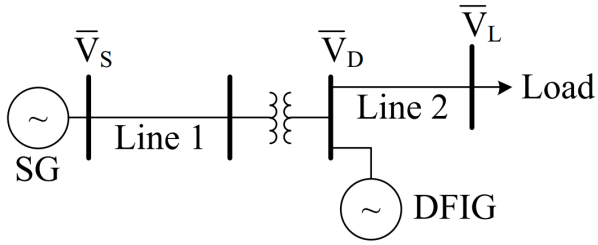

Figure 4.10: Four-bus single-area system.

GE 1.5 MW WTGs with rated speed of 450 rad/s (or 72 Hz) and rated output of 300 MW. The active power variations of the WTG due to the supportive signals can be expressed using (2.34). Under the operating condition given in Appendix B.2, the reduced-order WTG model can be obtained with $A_{\mathrm{rd}} = -0.0723$ and $C_{\mathrm{rd}} = 0.0127$. B_{rd1}, D_{rd1} and B_{rd2}, D_{rd2} with the corresponding K_{ie} and K_{pc} are listed in Table 4.1.

Table 4.1: Gain of Frequency Support Mode and Corresponding Matrix Value

Mode	Number	K_{ie}	B_{rd1}	D_{rd1}	K_{pc}	B_{rd2}	D_{rd2}
MPPT	1	0	0	0	0	0	0
IE	2	-0.10	0.6246	-0.10	0	0	0
IE	3	-0.20	1.2492	-0.20	0	0	0
IEPFC	4	-0.10	0.6246	-0.10	-0.03	0.1874	-0.03
IEPFC	5	-0.20	1.2492	-0.20	-0.06	0.3748	-0.06

The worst-case scenario is assumed to be the loss of one unit (150 MW), which occurs at 1 s. The safety limit is set to be a 0.5 Hz deviation to avoid triggering load shedding [69]. The frequency responses of all modes under this scenario are given in Fig. 4.11. The inertia emulation effect can be observed as the ROCOF becomes slower from the responses of Modes 1-3. The ROSs are calculated using the reduced-order model in Eq. (2.40), but the full-order linearized model in Appendix B.2 is used for verification. Denote $x_{\mathrm{rd}} = [\Delta\omega, \Delta P_m, \Delta P_v, \Delta\omega_r]$ and $x = \left[\Delta\omega, \Delta P_m, \Delta P_v, \Delta E'_{qD}, \Delta E'_{dD}, \Delta\omega_r, \Delta x_1, \Delta x_2, \Delta x_3, \Delta x_4\right]$ for theoretical analysis and simulation verification, respectively.

4.3.1 Model and Algorithm Validation

To validate the reduced-order model, consider the worst-case scenario above. The four state variables $\Delta\omega$, ΔP_m, ΔP_v, $\Delta\omega_r$ between reduced-order and full-order model of Mode 2-5 in Table 4.1 are compared in Fig. 4.12 and Fig. 4.13. The excellent agreements ensure that the reduced-order model based ROS should be sufficient to find the switching instants for the full-order dynamics.

With the given safety limit, the ROS for Mode 1 under no disturbance can be projected onto the plane $\Delta\omega$-ΔP_m as illustrated in Fig. 4.14 with two different initializations. The iteration sequences indicate that if more initial guess points are used, the fewer iterations

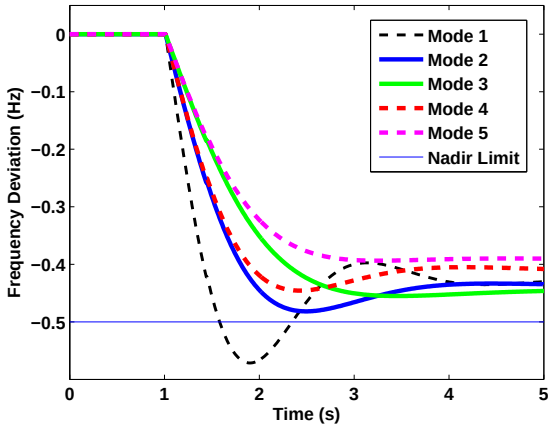

Figure 4.11: Frequency response of different modes under the worst-case scenario: 150 MW generation loss.

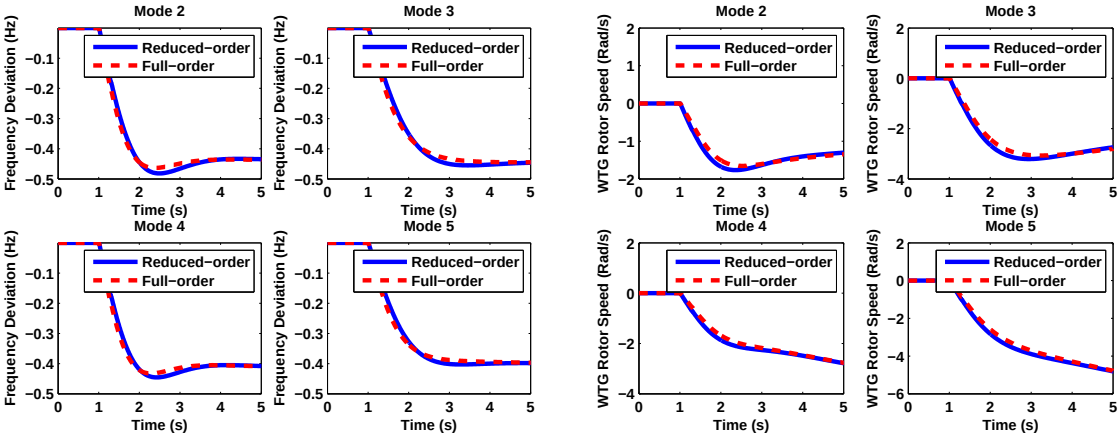

(a) **(b)**

Figure 4.12: Dynamics between full-order and reduced-order model under different modes: (a) Frequency deviation; (b) WTG rotor speed.

are needed and a better estimation can be achieved (as shown in the blue case). The final result is shown in Fig. 4.15. The green region is the ROS obtained by extensive simulations and can be regarded as the largest ROS. The comparison shows that the proposed algorithm successfully reduces conservatism in the estimate of the largest ROS.

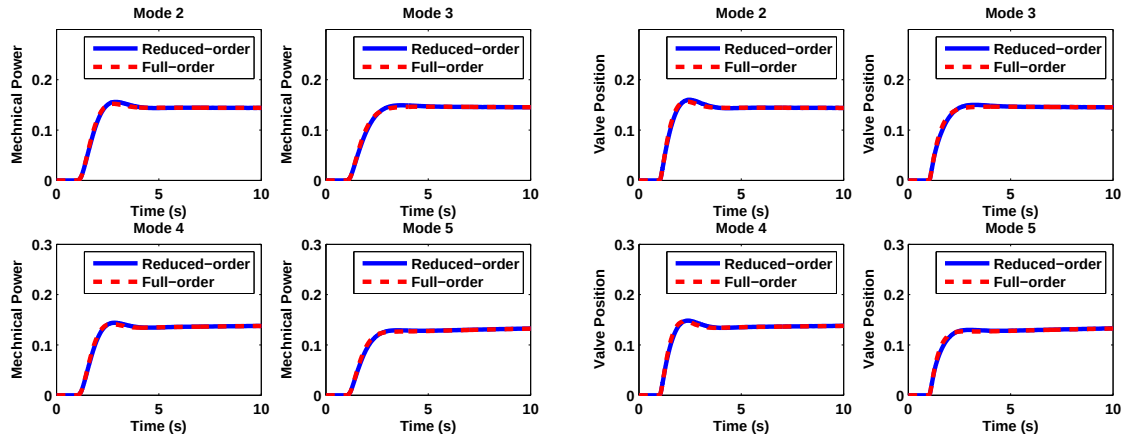

(a) (b)

Figure 4.13: Dynamics between full-order and reduced-order model: (a) Turbine-governor mechanical power; (b) Turbine-governor valve position.

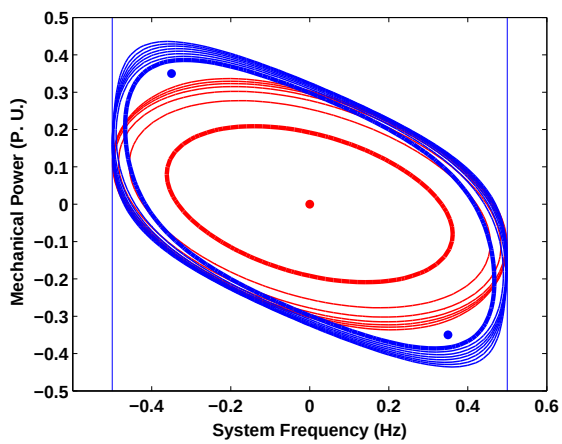

Figure 4.14: Iteration in calculating ROS with different initializations.

4.3.2 IE Mode Only

The ROSs under the worst-case scenario of Modes 1-3 are calculated with representation of polynomials in terms of x_{rd} up to degree 8. Denote these regions as

$$\text{Worst-case ROS 1: } \mathcal{S}_{d1} = \{x_{\mathrm{rd}} : B_{d1}(x_{\mathrm{rd}}) \leq 0\}$$

$$\text{Worst-case ROS 2: } \mathcal{S}_{d2} = \{x_{\mathrm{rd}} : B_{d2}(x_{\mathrm{rd}}) \leq 0\}$$

$$\text{Worst-case ROS 3: } \mathcal{S}_{d3} = \{x_{\mathrm{rd}} : B_{d3}(x_{\mathrm{rd}}) \leq 0\}$$

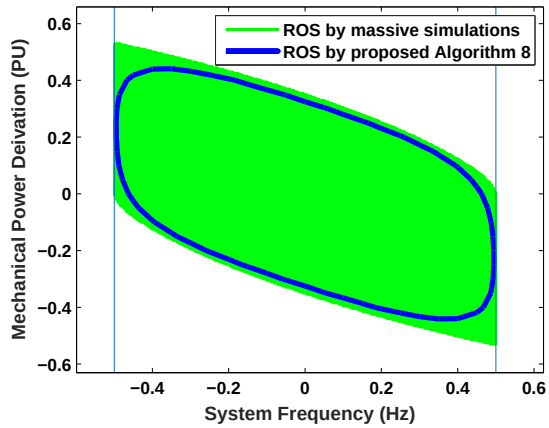

Figure 4.15: ROS of Mode 1 under normal condition obtained by proposed Algorithm 8 and extensive simulations.

where $B_{d1}(x_{\mathrm{rd}})$, $B_{d2}(x_{\mathrm{rd}})$ and $B_{d3}(x_{\mathrm{rd}})$ serve as the safety switching guards.

To determine if the safety can be preserved under Mode 1, one needs to check whether the intersection between $\mathcal{S}_{d1}$ and the pre-disturbed operating point x_0 is empty. In our case, the fact that $\mathcal{S}_{d1} \cap \{x_0\} = \varnothing$ is graphically shown in Fig. 4.19 and mathematically verified by $B_{d1}(x_0) > 0$. According to Proposition 4.2, the safety cannot be preserved without switching to grid-supportive modes as shown in Fig 4.11.

To verify the largest deadband or equivalently the critical switching instant from Mode 1 to Mode 2 or 3, the values of $B_{d2}(x_{\mathrm{rd}})$ and $B_{d3}(x_{\mathrm{rd}})$ with respect to the disturbed trajectory of Mode 1, denoted as X_{d1} (dash line in Fig. 4.16), is calculated. Note that X_{d1} is from the full-order model and only relevant states $\bar{X}_{d1} = [X_{d1}(1), X_{d1}(2), X_{d1}(3), X_{d1}(6)]$ are substituted into the guards. The zero-crossing point from negative to positive values denotes the critical switching instant t_{cr}, or equivalently the largest deadband with the value $\Delta\omega(t_{\mathrm{cr}})$. As shown in Fig. 4.17, the largest deadband (critical switching instant) is 0.30 Hz (1.29 s) if Mode 2 is used, and 0.42 Hz (1.44 s) if Mode 3 is used. Simulations of each scenario with the suggested largest deadband as well as the recommended value from GE (0.15 Hz) are carried out and shown in Fig. 4.18. As seen the system safety is preserved under all cases, but the recommended values are conservative especially when Mode 3 is activated. On the other hand, the fact that the frequency nadir is extremely close to the limit indicates that the estimated ROS is not overly conservative.

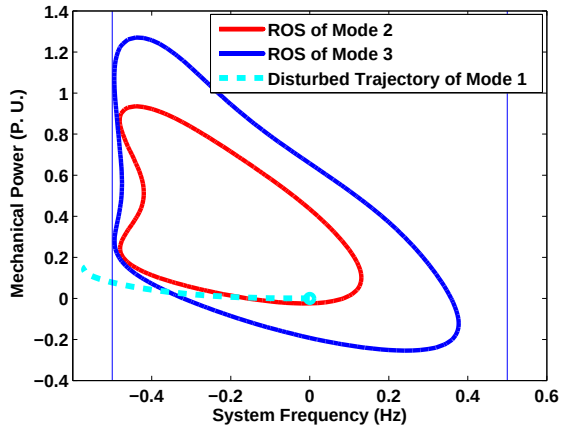

Figure 4.16: ROS of Mode 2 and 3 under given scenario.

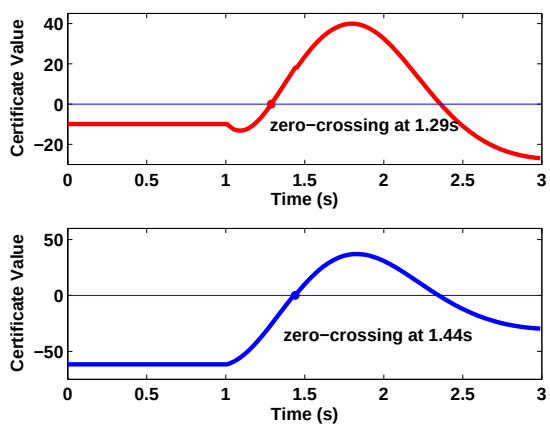

Figure 4.17: Value of $B_{d2}(x)$ (upper) and $B_{d3}(x)$ (lower) w.r.t the disturbed trajectory X_{d1}

Beyond safety, the earliest support deactivation (earliest switching instant) is established so that the emulated inertia can be shed to obtain faster frequency restoration. Let the trajectories in Fig. 4.18 be denoted as X_{d12} (left) and X_{d13} (right) and substituted into $B_{d1}(x_{\mathrm{rd}})$ to find the zero-crossing point from positive to negative, which occurs approximately at 2 s for both cases. Negativity of the safety switching guard $B_{d1}(\bar{X}_{d1i})$ guarantees a safe switching from Mode i to Mode 1. Earlier switchings when $B_{d1}(\bar{X}_{d1i}) > 0$ will lead to an unsafe trajectory. Both cases are shown in Fig. 4.21.

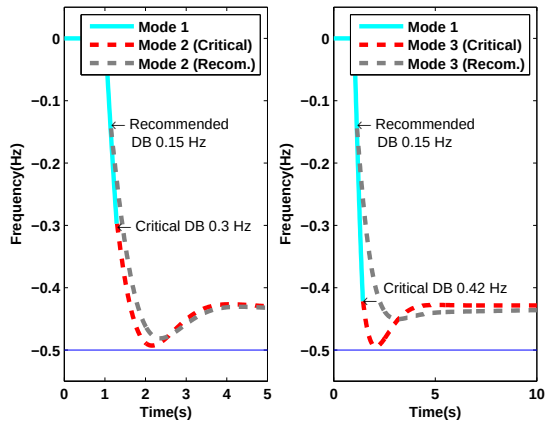

Figure 4.18: Frequency dynamics of full-order model under calculated critical deadband.

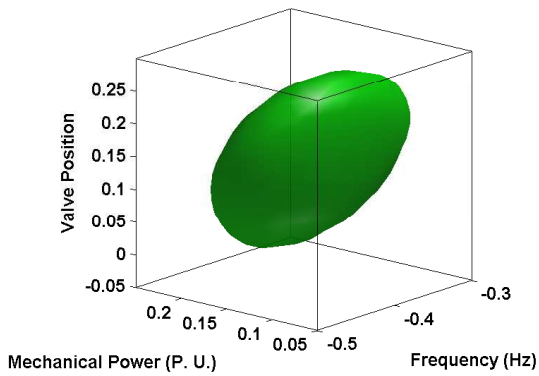

Figure 4.19: ROS of Mode 1 under the given scenario.

4.3.3 IEPFC Mode and Safety Recovery

The PFC loop will artificially create additional load-frequency sensitivity and the maximum frequency excursion will be decreased. The deadband analysis procedure is similar and will not be repeated. However, when it comes to the support deactivation, due to the additional constant frequency deviation signal, a safe switching time window appears. Thus, the PFC mode needs to be deactivated before a critical time. The mechanism is illustrated in Fig. 4.22. The WTG attempts to draw the total energy that has been pulled out during the grid supporting to restore the rotor speed. So the upper area and lower area with respect to the original operating point have to be equal. When the PFC is deactivated, the supportive power decreases below the original operating point to satisfy this equal-area criterion. This

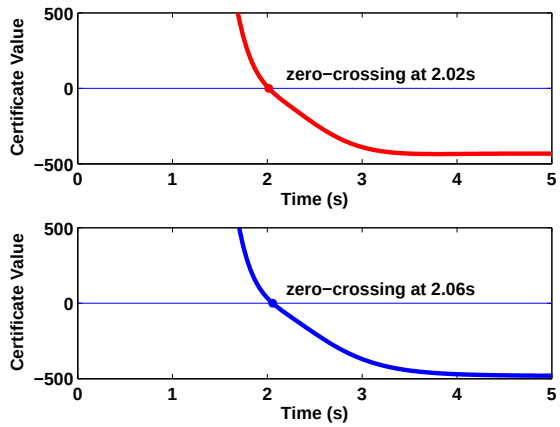

Figure 4.20: Value of $B_{d1}(x)$ w.r.t. the disturbed trajectories X_{d12} (upper) and X_{d13} (lower).

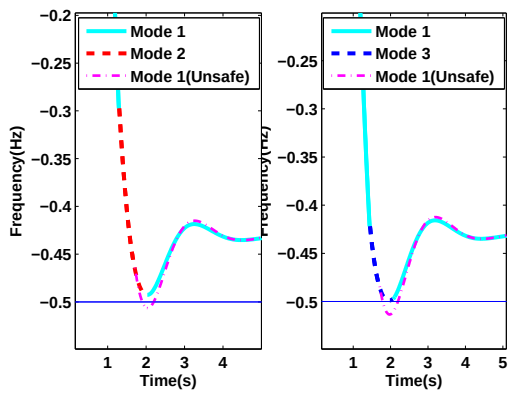

Figure 4.21: Frequency dynamics under critical deadband and threshold.

sudden shortage of active power, if large enough, will lead to an unsafe trajectory. Let Mode 5 be designed with a deadband of 0.3 Hz and substitute the disturbed trajectory $\bar{X}_{d15}$ into $B_{d1}(x_{\mathrm{rd}})$, then the critical switching window can be observed as shown in the upper plot of Fig. 4.23, where the critical deactivating instant suggested by the guard is 15.2 s. A deactivation at 22 s leads to an unsafe trajectory. Frequency dynamics of both cases are shown in the upper plot of Fig. 4.24.

To extend the safe switching window, we propose a safety recovery procedure illustrated by Fig. 4.25. When the PFC mode is deactivated, the corresponding IE mode is kept to address the sudden shortage of active power. By checking the value of $B_{d3}(x_{\mathrm{rd}})$ with respect to the trajectory $\bar{X}_{d15}$ (lower plot of Fig. 4.23), it indicates that this procedure postpones

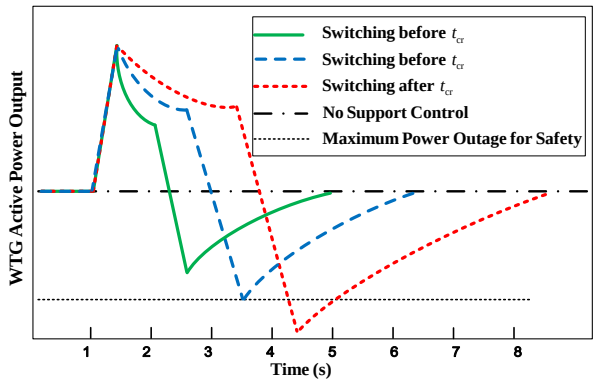

Figure 4.22: An equal-area criterion in support-deactivation procedure.

the critical deactivating instant by 15 s. The original unsafe switching from Mode 5 directly to Mode 1 at 22 s is now safely switched to Mode 3 as shown in the lower plot of Fig. 4.24. The critical switching instant from Mode 5 to 3 is suggested to be 30.21 s by the guard in Fig. 4.23 and verified by simulation in Fig. 4.24.

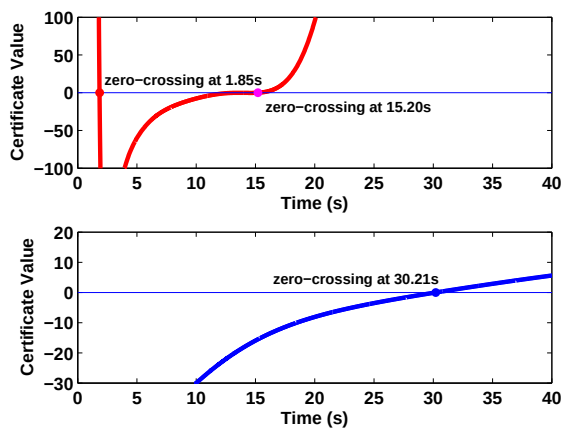

Figure 4.23: Upper: Value of $B_{d1}(x)$ and $B_{d3}(x)$ w.r.t. the disturbed trajectory X_{d15}.

4.4 Safety Supervisory Control for WTGs

Under high levels of renewables, a fixed deadband may not be sufficient as the commitments of synchronous generators could change dramatically over time due to the stochastic output characteristics of renewable sources [106]. In this section, the ROS is employed online to be a safety supervisor. The ASFR model will be used as the state observer to provide

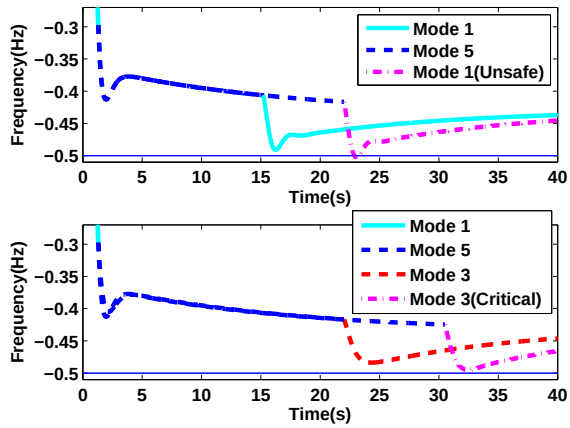

Figure 4.24: Frequency dynamics under 0.3 Hz deadband and critical deactivation: normal sequence Mode 1-5-1 (Upper) and safe recovery sequence Mode 1-5-3-1 (lower)

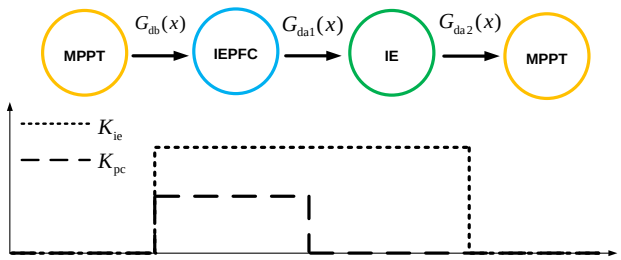

Figure 4.25: Modelling deadband as a hybrid transition system.

the grid awareness capability. The state observer and safety supervisor compose the safety supervisory control (SSC), which is able to switch the modes of WTGs to ensure adequate frequency response in the grid under disturbances as well as provide the real-time margin to the critical limits, that is, the remaining available time for a safe switching. Meanwhile, the SSC constantly updates its boundary with respect to different renewable penetration levels and commitments of synchronous generators so that it is robust against the stochastic renewable outputs.

In this section, full-scale nonlinear simulations and experimental verification will be performed. Section 4.4.1 demonstrates the design procedure of the SSC using a single-machine three-phase nonlinear microgrid model in Simulink. In Section 4.4.2, the SSC will be implemented with a decentralized fashion in the IEEE 39-bus system in DSATools. In

Section 4.4.3, the SSC is experimentally implemented in the HTB at CURENT. All ROS computations in this section are performed using the formulation in Problem 4.6.

4.4.1 SSC for a Single-Area System

To illustrate the SSC design using the proposed framework, the lumped diesel-wind fed microgrid in [122] is employed. Assume that the parameters of the ASFR in the form of (**??**) have been estimated. The parameters are given as follows

$$H_c = 2, \overline{R}^{-1} = 30, \overline{\tau}_{\text{gv}} = 0.1, \overline{\tau}_{\text{ch}} = 0.5, k_{\text{scal}} = 0.15, K_{\text{ie}} = 0.2, \Delta P_D \in D = \{d : 0 \leq d \leq 0.32\}$$

$$A_{\text{rd}} = -0.3914, C_{\text{rd}} = 1.37, B_{\text{rd1}} = -0.3121, D_{\text{rd1}} = 1, B_{\text{rd2}} = 0, D_{\text{rd2}} = 0$$

The safety limit is set as $\omega_{\text{lim}}^{-} = 58.5$ Hz, intentionally leaving no extra margin. With all the given conditions, Problem (4.6) is formulated in Yalmip [54] and solved by Mosek [7]. The ROS is represented by the zero sublevel set of $B(x)$ and its projection on the phase plane of the frequency and mechanical power is shown in Fig. 4.26. The green region is the ROS

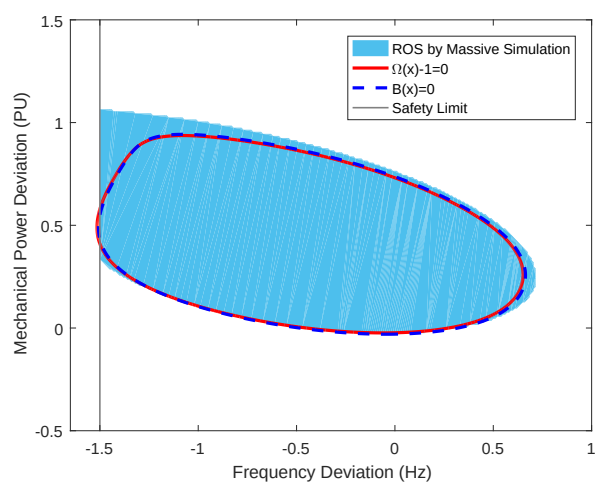

Figure 4.26: Comparison of ROS (projected onto $\Delta\omega - \Delta P_m$ plane) between the subzero level set of $B(x)$ (blue dash) and exhaustive simulations (blue).

obtained by massive simulations and can be considered very close to the largest one. As shown by minimizing the area under the slack function $\Omega(x)$, the zero level set of $B(x)$ is expanded by $\Omega(x) - 1$ as much as possible to the largest ROS under the fixed highest degree.

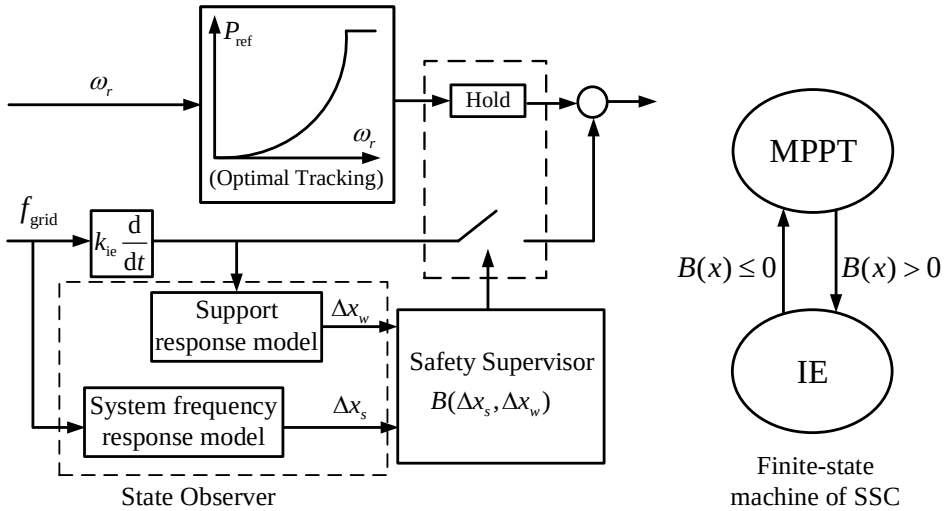

Figure 4.27: Safety supervisory control (SSC) integrated in WTGs, which enables the system awareness capability and provides real-time systemic safety margin for WTGs.

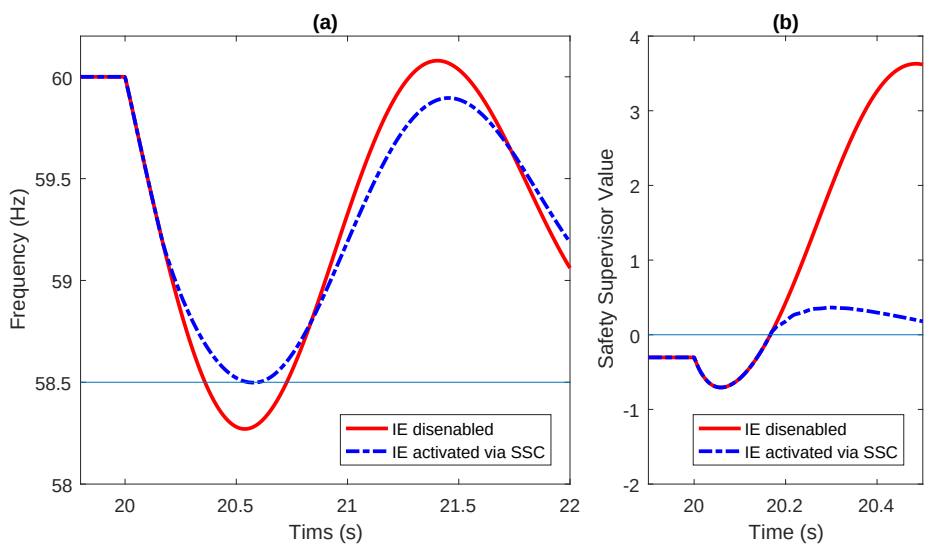

Figure 4.28: Frequency response under no inertia emulation and inertia emulation activated via safety supervisory control (SSC), (a) frequency response, (b) value of safety supervisor.

Once $B(x)$ is obtained, it can be deployed online in the configuration shown in Fig. 4.27. The speeds of diesel and wind turbine generators are measurable. The estimated frequency response model used in the ROS computation is now employed as the state observer for ΔP_m and ΔP_v. The SSC integrated into the WTG not only enables the grid awareness capability, but also provides the remaining available time for adequate frequency response.

As for simulation, the full-order nonlinear model of the synchronous generator is employed and scaled down to the microgrid level. A type-4 wind turbine with the averaged converter model is used as well. Detailed descriptions of models used in simulation can be found in [122]. The system is imposed on the worse-case disturbance. The frequency response and the value of the safety supervisor are shown in Fig. 4.28. The IE is activated when the supervisor's value is crossing zero. As seen the nadir of the frequency response from SSC is exactly on the safety limits, indicating the estimated ROS is not conservative at all.

4.4.2 Decentralized SSC for Multi-Machine Systems

Center of Inertia Frequency

As mentioned in Section 2.1.2, we aim at the adequacy of the COI frequency. On one hand, the COI frequency filters out the local swings to gives a clearer measure of the systemic performance of concern [64], and thus becomes the target in many related works [25, 59, 63, 64]. On the other hand, due to the increasing computation complexity of the SOS decomposition with respect to system dimensions, addressing every individual machines will make the problem intractable. Considering the fact that the frequency deviation of single machine (area) from the COI frequency is determined by the electric distance to the inertial center, which is further determined by the line impedance [5], extra margins can be added to the safety limit to prevent the frequency of single machine (area) from reaching the UFLS zone.

Let $\mathcal{S}$ denote the index set of synchronous generators. Let $\mathcal{W}$ denote the index set of WTGs that have been selected as actuators of the SSC. N_s and N_w denote the total number of generators in each set, respectively. The model in (2.5) will serves as the COI frequency response model, where the COI inertia constant H_{c} is calculated as

$$H_{\mathrm{c}} = \frac{\sum_{i\in\mathcal{S}}^{N_s} S_i H_i}{S_{\mathrm{sg}}}, S_{\mathrm{sg}} = \sum_{i\in\mathcal{S}}^{N_s} S_i \tag{4.9}$$

where S_i, H_i are the base and inertia constant of synchronous generator i. The governor and turbine models represent the averaged mechanical behavior of the overall system. It is assumed that the corresponding time constants have been estimated.

To use the Transient Security Assessment Tool (TSAT) [82], the western electricity coordinating council (WECC) generic type-3 WTG model and its corresponding control presented in [32] is employed. The active power control loop is shown in Fig. 4.29. The low-pass filter $G_1(s)$ aims to filter out the fluctuation from the MPPT signal, where its time constant T_{sp} is usually in the time frame of tens of seconds [17]. So during the inertial and primary frequency response, the reference signal ω_{ref} can be assumed as a constant. The transfer function $G_3(s)$ is to model the inner current loop dynamics in converter controllers. As the current regulation is in the time frame of milliseconds, this part is omitted [97]. Similarly like the frequency response model of synchronous generators, an aggregated model

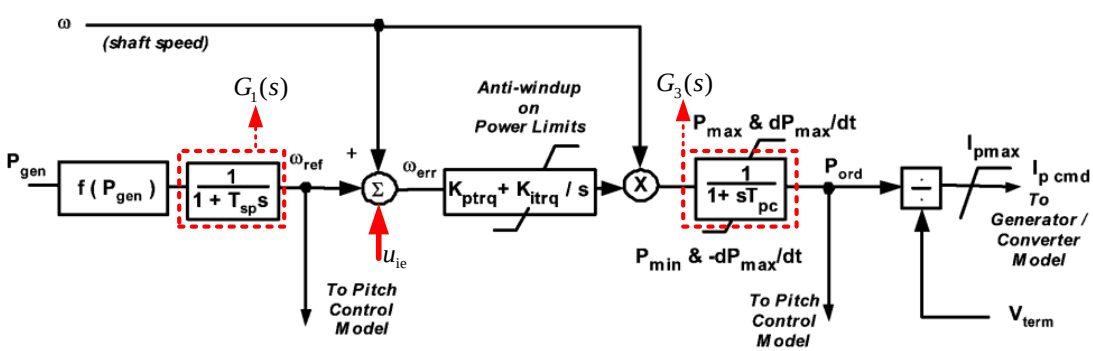

Figure 4.29: Widely used active power control loop for the WECC generic type-3 wind turbine generator model [32, 17, 81].

is employed to represent the overall behavior of WTGs that have been selected as the actuators of SSC. Based on the above simplifications, the synthetic inertial response model reads

$$\begin{aligned} \dot{\overline{x}} &= \overline{K}_{\text{itrq}}(\overline{\omega}_r - \overline{\omega}_{\text{ref}} + \overline{u}_{\text{ie}}) \\ \dot{\overline{\omega}}_r &= \frac{1}{2\overline{H}_w \overline{\omega}_r}(\overline{P}_{m,w} - \overline{\omega}_r \overline{y}) \end{aligned} \tag{4.10}$$

where

$$\begin{aligned} \overline{y} &= \overline{x} + \overline{K}_{\text{ptrq}}(\overline{\omega}_r - \overline{\omega}_{\text{ref}} + \overline{u}_{\text{ie}}) \\ \overline{P}_G &= \overline{\omega}_r \overline{y} \end{aligned} \tag{4.11}$$

And the averaged inertia constant of WTGs is calculated as

$$\overline{H}_w = \frac{\sum_{i\in\mathcal{W}}^{N_w} S_i H_i}{S_{\text{wt}}}, S_{\text{wt}} = \sum_{i\in\mathcal{W}}^{N_w} S_i \tag{4.12}$$

In (4.10), $\overline{u}_{\text{ie}}$ generated from the COI frequency is the input and the power variation $\overline{P}_G$ with the base of S_{wt} is the output. The aerodynamic model in [81] is employed, where $\overline{P}_{m,w}$ is a function of $\overline{\omega}_r$, wind speed and pitch angle. Under the time snapshot of inertial and primary response, wind speed, pitch angle and $\overline{\omega}_{\text{ref}}$ are assumed to be fixed. As shown in [126], linearized models are able to capture the input-output relation from the ROCOF to the supportive power variations of WTGs. Linearizing (4.10) and applying a change of base as $k_{\text{scal}} = S_{\text{wt}}/S_{\text{sg}}$ yields the following state-space model of the WTG

$$\begin{aligned} \dot{\overline{x}}_w &= A_w \overline{x}_w + B_w \overline{u}_{\text{ie}} \\ \Delta\overline{P}_G &= C_w \overline{x}_w + D_w \overline{u}_{\text{ie}} \end{aligned} \tag{4.13}$$

where

$$\Delta\overline{x}_w = \begin{bmatrix} \Delta\overline{x} & \Delta\overline{\omega}_r \end{bmatrix} \tag{4.14}$$

By combining (4.13) with (4.1) one can obtain the ASFR for the ROS computation. On the other hand, the state observer from $\overline{u}_{\text{ie}}$ to $\overline{x}$ is defined as

$$\begin{aligned} \dot{\overline{x}}_w &= A_w \overline{x}_w + B_w \overline{u}_{\text{ie}} \\ \overline{y} &= \begin{bmatrix} 1 & 0 \\ 0 & 1 \end{bmatrix} \Delta\overline{x}_w \end{aligned} \tag{4.15}$$

Decentralized Communication for Small-Scale Systems

Based on the previously developed response model, a centralized communication link shown in Fig. 4.30 (a) is needed for the SSC. The speed of each synchronous generator (area) is measured and transmitted to the central controller to calculated the COI frequency. Then, the COI frequency is sent to the state observers to estimate states $\Delta\overline{P}_m$, $\Delta\overline{P}_v$, $\Delta\overline{x}$ and $\Delta\overline{\omega}_r$. Finally, all the states are substituted into the safety supervisor for making a switching decision. This switching signal will need to be transmitted to each WTG to activate the inertia emulation. Although such a communication fashion will theoretically ensure the safe response of the COI frequency, it will introduce delay and complexity, reduce reliability and require extra cost of communication infrastructure.

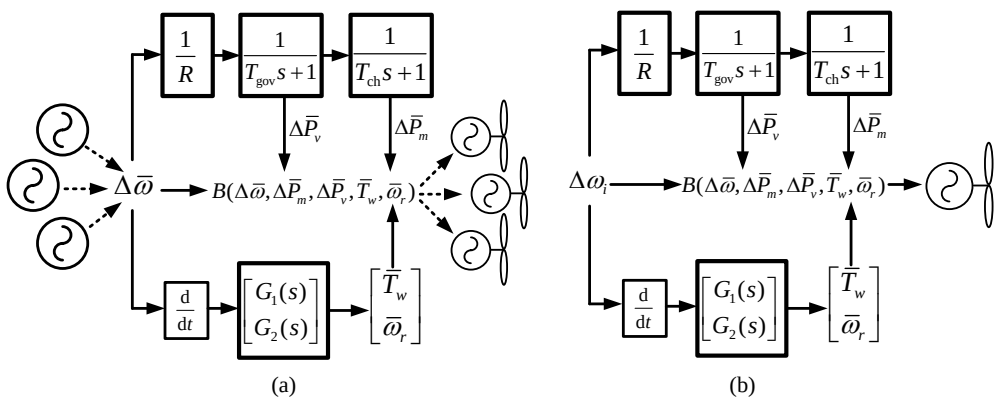

Figure 4.30: Centralized and decentralized Communication fashions in SSC. The decision results will be equivalent in a small scale system.

Essentially all WTGs will only need the switching signal, which is determined by predicting the overall system behavior. Since frequency is a global feature, the system awareness capability can be integrated locally in each WTG using the same state observer. Then, as long as the input is the COI frequency, the result will be the same. In order to further reduce the communication links, measuring local frequency is desired. It is known that the local frequency will deviate from the COI frequency during the transient period. But for a small-scale system, such deviations are sufficiently small. Thus, it is reasonable to assume that the frequency of single machine (area) is approximately equal to the COI frequency, i.e., $\omega_i \approx \overline{\omega}$. Therefore, the centralized SSC can be replaced approximately by the

decentralized SSC shown in Fig. 4.30 (b). The decentralized SSC is completely integrated in a single WTG, and only local frequency measure is needed. However, it is worth mentioning that such a communication reduction is only equivalent when the system is small.

Simulation Setup and Dynamic Performance Verification

In this subsection, the modified New England IEEE 39-bus system with more than 50% wind penetration is employed to demonstrate the SSC. Two scenarios with different numbers of WTGs as the actuators are illustrated.

The modified generator data of the system is listed in Tab. 4.2. All other parameters are the same with the standard ones in [86]. The bold inertia constants indicate that they are visible to the grid. The synchronous generators are round rotor models equipped with the

Table 4.2: Generator Data of Modified New England 39-bus System

#	Bus	Type	Output (MW)	Base (MVA)	Inertia (s)
1	30	WTG	550	$S_1 = 670$	$H_1 = 8.00$
2	31	WTG	572	$S_2 = 670$	$H_2 = 8.00$
3	32	WTG	650	$S_3 = 670$	$H_3 = 8.00$
4	33	SG	632	$S_4 = 1000$	$H_4 = \mathbf{2.86}$
5	34	WTG	508	$S_5 = 670$	$H_5 = 8.00$
6	35	WTG	650	$S_6 = 670$	$H_6 = 8.00$
7	36	SG	400	$S_7 = 1000$	$H_7 = \mathbf{2.64}$
8	37	WTG	540	$S_8 = 670$	$H_8 = 8.00$
9	38	SG	830	$S_9 = 1000$	$H_9 = \mathbf{3.45}$
10	39	SG	859	$S_{10} = 1000$	$H_{10} = \mathbf{5.00}$

1992 IEEE type DC1A excitation system model (ESDC1A) and the steam turbine-governor model (TGOV1) [96]. The WECC generic type-3 WTG model with built-in controls in [81] is implemented as a user-defined model (UDM). The corresponding parameters are given in Appendix B.3. The SSC is realized by using the dynamically linked blocks (DLBs) and implemented using C/C++, which is proved to be effect for advanced control design realization [88]. The overall dynamic simulations are performed in TSAT [82].

The traditional plant pool is $\mathcal{S} = \{4, 7, 9, 10\}$. The worse-case contingency is the loss of entire traditional plant 7, which is a 400 MW generation loss. The safety limit is set to be 59 Hz. In the New England system, synchronous machines' frequency are close to the COI

frequency. Considering the fact that the UFLS rely allow frequency stay in triggering zone for several cycles, it is sufficient to ensure the exact safety of the COI frequency response. This is also for the purpose of demonstrating the precision of the proposed framework.

In the first scenario, only WTG 5 is selected as the actuator equipped with $K_{\text{ie}} = 0.2$. The power and current limits are modified to assume an over-size design of converters. Under the worst-case contingency, the COI frequencies of no switching case and supervised switching one are compared in Fig. 4.31 (a). As seen, the supervisory control timely activates the IE function of WTG 5 based on the supervisor value (shown in Fig. 4.31 (b)) so that the COI frequency stays within the specified safety limit. Since the IE gain is large, there is approximately one second reaction time for WTG 5 to respond. Individual speeds of synchronous generators are also plotted. As seen, they are close to the COI frequency. So ensuring safe COI frequency response could greatly reduce the possibility of the unnecessary frequency relay actions.

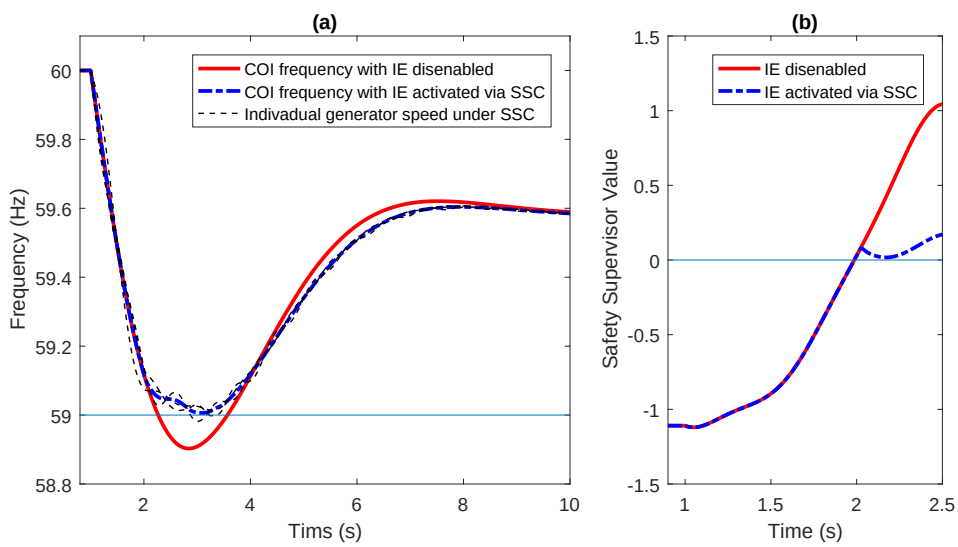

Figure 4.31: Frequency response under no inertia emulation and inertia emulation activated via safety supervisory control (SSC), (a) frequency response, (b) value of safety supervisor. The reaction time is around one second in this scenario.

In the second scenario, three WTGs are chosen to be the actuators, i.e., $\mathcal{W} = \{1, 2, 5\}$, with a smaller gain of $K_{\text{ie}} = 0.03$ so that each WTG will not reach its normal designed limit. The same contingency is applied. The COI frequency and individual frequencies of synchronous generators are plotted in Fig. 4.32 (a). Fig. 4.32 (b) indicates that the IE

function is activated in slightly different times, from 0.4 to 0.6 s in different WTGs. This is because the slight differences between local frequencies. The power outputs of WTG 1, 2 and 5 are shown in Fig. 4.33. Each of them contributed less than 0.1 per unit supportive power from their operating points, while WTG 5 in the previous scenario contributed more than 0.15 per unit. It is always preferred to coordinate more actuators to reduce the required contribution from each one.

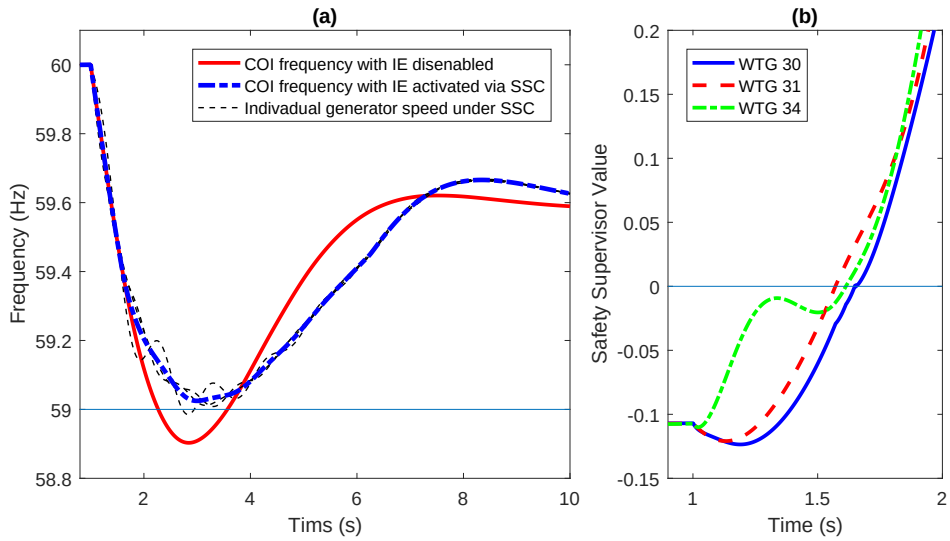

Figure 4.32: Frequency response under no inertia emulation and inertia emulation activated via safety supervisory control (SSC), (a) frequency response, (b) value of safety supervisor. The reaction time is from 0.4 to 0.6 second in different WTGs in this scenario.

Adaptive SSC Against Varying Renewable Penetration

Due to the stochastic and intermittent nature of renewable resources, the commitment of traditional plants can change dramatically over time, which could significantly change the system frequency response characteristics. This time-varying feature requires a SSC to be adaptive to the system operating condition. This adaptivity can be implemented by adding a scheduling loop overseeing the triggering loop as shown in Fig. 4.34. The triggering loop will receive local measurements and make a decision based on the up-to-date supervisor. On the other hand, the scheduling loop will receive global information, such as, unit commitment and WTG outputs, and then recalculate settings for the safety supervisor. When choosing actuators, those with larger available capacity will be selected first. The SFR model will be

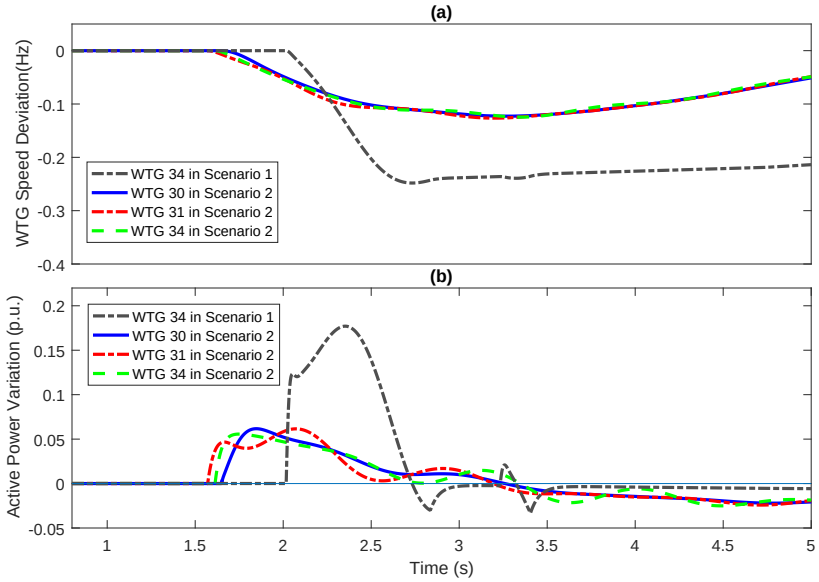

Figure 4.33: Active power variation of WTGs in different scenarios.

updated and the supervisor will be re-calculated. If the SOS program is not feasible, more WTGs are incorporated and the IE gain will be adjusted.

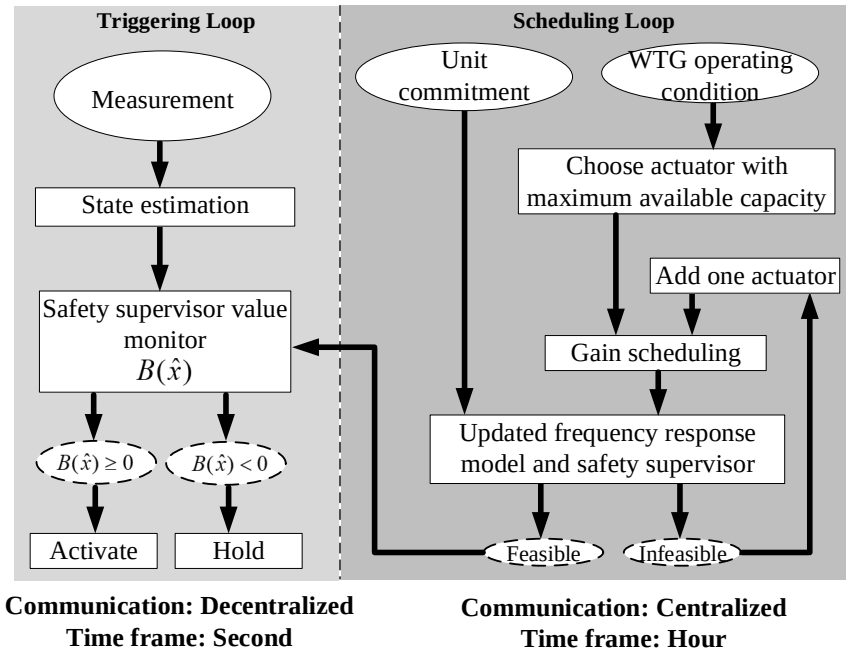

Figure 4.34: Two-loop SSC with adaptivity and robust to the change of system operating point.

The scheduling loop will need a centralized communication link. But the two loops are in different time scales. When a disturbance takes place, the SSC uses the latest received ROS as the threshold function to determine the activation of the IE mode. Therefore, the triggering level stays in a decentralized fashion. This is importance since the time scale of this level is in terms of seconds. The scheduling level will be in the same time scale of economic dispatch, and can be regarded as an enhanced functionality of energy management system.

The demonstration here is based on the setup of Scenario 1, that is, $\mathcal{W} = 5$ and $k_{\text{ie}} = 0.2$. The worst-case disturbance and safety limit are also the same. In New England system, SG 10 is to equivalently model the rest of the Eastern Interconnections. Assume a scenario where the level of renewable penetrations in the Eastern Interconnections increases significantly within a time. This change can be equivalently represented by decreasing the inertia constant of SG 10. Here, three different constants, that is, 10, 5 and 1, are used to represent different unit commitment scenarios at certain time snapshots. Based on the information, the scheduling loop will update the SFR model and re-calculate the ROS. Thus, three different ROSs will be obtained with respect to the three inertia constants of SG 10 shown in Fig. 4.35 (a). The ROS shrinks with the increase level of renewable penetration. Now assume the worse-case disturbance happens when $H_{10} = 1$. Based on up-to-date ROS 1, which corresponds to the scenario of $H_{10} = 1$, the adequate reaction time should be around 0.2 s as shown in Fig. 4.35 (b), and the safety of COI frequency can be ensured shown in Fig. 4.36 (a). If not updated in time, that is, either ROS 2 or 3 is online, the IE will not be activated in time, and the corresponding COI frequencies are not safe also depicted in Fig. 4.36 (a). The speeds and outputs of WTGs under up-to-date and out-of-date SSCs are also plotted in 4.36 (b) and (c), respectively.

Based on the setting of Scenario 1, the inertia constant of SG 10 is changed from 1 to 10 s to represent the operation change of the rest eastern interconnection. Using the same safety setting, the ROSs under different operating conditions are computed and plotted in Fig. 4.35 (a). The same disturbance is applied when $H_{10} = 1$ s and the trajectory is plotted in Fig. 4.35 (a) as well. The values of different supervisors with respect to this trajectory are shown in Fig. 4.35 (b). The adequate reaction time should be around 0.2 s based on the

corresponding supervisor (blue), but other supervisors provide larger times, which will lead to inadequate responses.

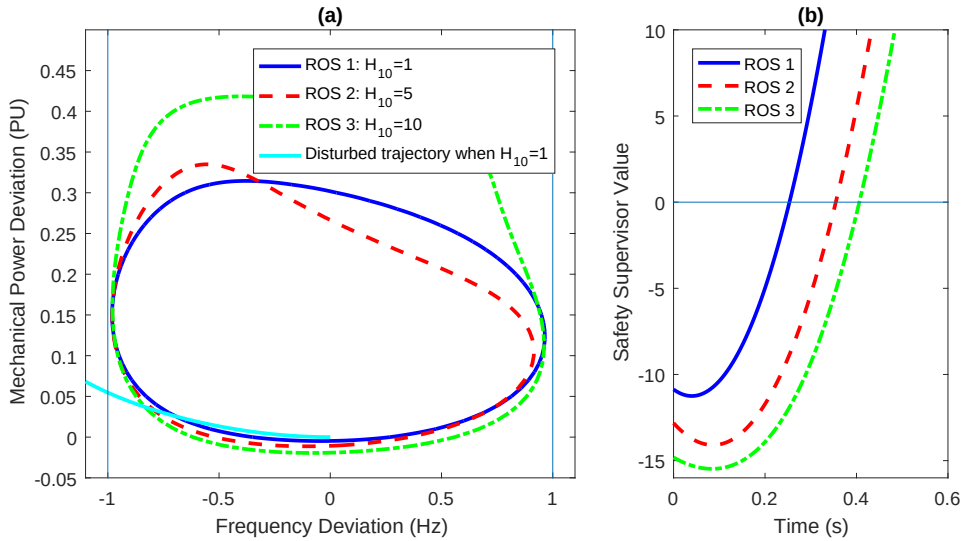

Figure 4.35: (a) ROSs under different operating conditions. (b) Values of different supervisors with respect to the disturbed trajectory when $H_{10} = 1$ s.

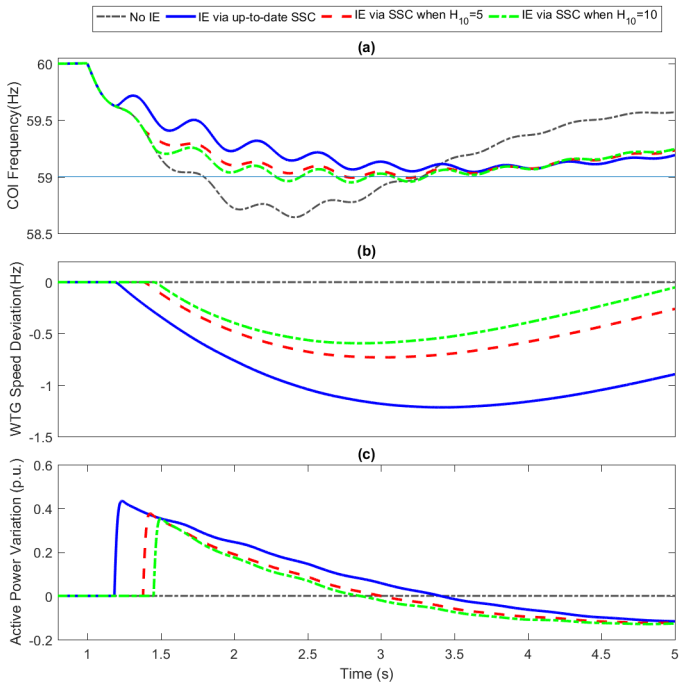

Figure 4.36: (a) COI Frequencies under different SSCs. (b) WTG Speeds under different SSCs. (c) Active power variation of WTGs under different SSCs.

4.4.3 Experimental Implementation in HTB

The proposed control is implemented on an aggregated WECC system modeled in the HTB of CURENT. The WECC system is divided into four areas as shown in Fig. 4.37 (a). In addition, Area 1, 2 and 3 are divided into two regions. Thus, the total number of regions in the system are equal to seven. All generators of every region are aggregated into one generator using DYNRED software, then loads and branches are manually combined to obtain the system shown in Fig. 4.37 (b).

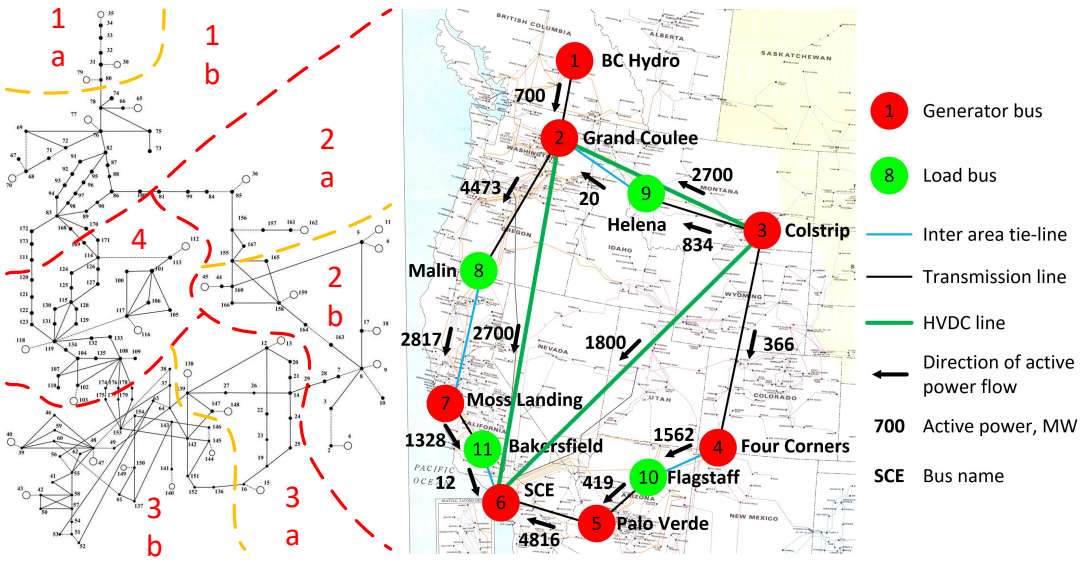

Figure 4.37: WECC system in HTB. (a) WECC 179-bus system divided into four areas. (b) WECC four-area system emulated in HTB.

The generators at Colstrip (Bus 3) and Four Corners (Bus 4) are WTGs controlled as the virtual synchronous generators (VSGs). The VSG control design in the HTB is presented in [57] and shown in Fig. 4.38. Thus, they can provide programmable synthetic inertia via the kinetic energy and energy storage units. The SSC is integrated in the mechanical model. In the WECC system, the SSC cannot be designed in the decentralized manner. The wide-area measurement signals are needed. The generator speeds are transmitted to WTG 3 and 4 to calculate the COI frequency, whereby the triggering signal can be generated. This wide-area SSC diagram is shown in Fig. 7. In normal conditions, WTG 3 and 4 operate under low-inertia mode to avoid using energy storage units frequently. Once the SSC is activated, the

controller will switch to a remedial mode with high inertia to release the storage energy as shown in Fig. 4.39.

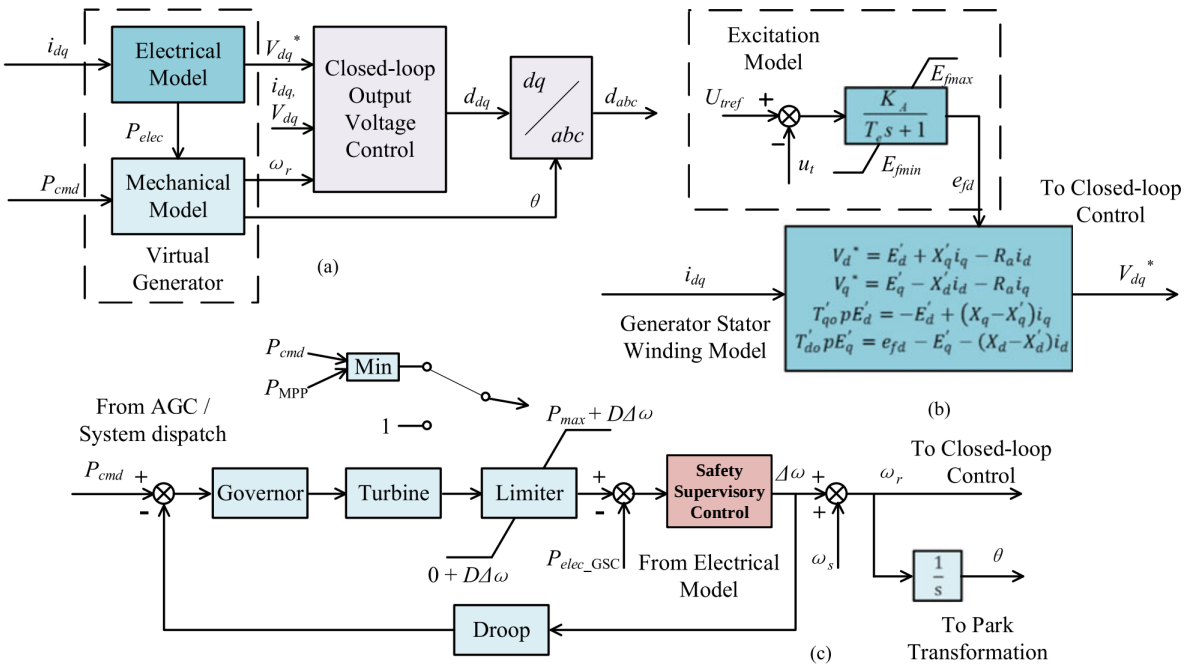

Figure 4.38: GSC control to mimic SG behavior in power system, (a) overall control diagram. (b) electrical model. (c) mechanical model [57].

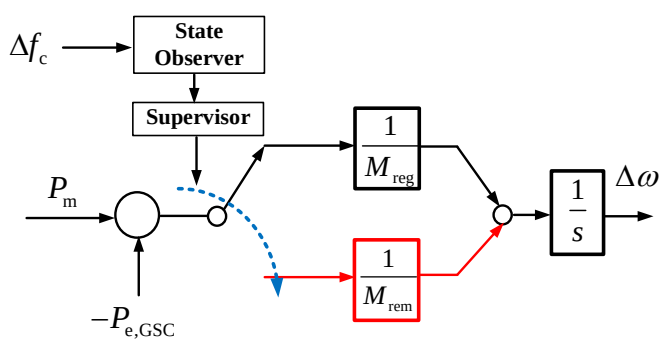

Figure 4.39: Wide-area SSC in the VSG mode-based WTG.

In the experimental demonstration, a 0.5 p.u generation loss is applied at Palo Verde (Bus 5), and the experiment results are shown in Fig. 4.40. The red curve indicates that the remedial mode with the supervisor is correctly scheduled and triggered to limit the COI

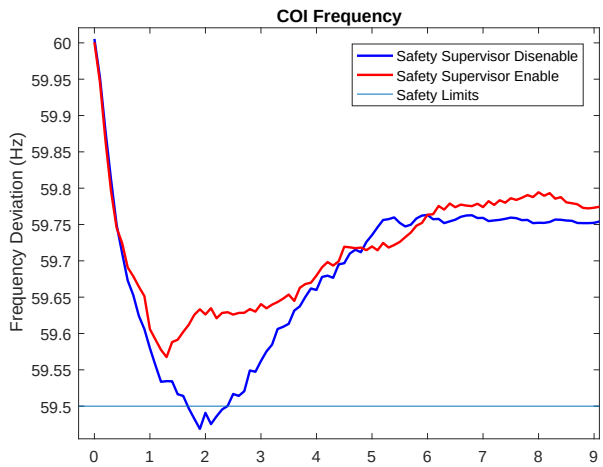

Figure 4.40: COI frequencies under different cases.

frequency within the desired bounds. The blue curve is the COI frequency response when the controller is dis-enabled, the performance metric of which is not satisfied. In addition, by comparing the results, half a second communication delay in the HTB can be observed.

4.5 Summary

This chapter first states the mode synthesis principle for safe response and the concept of ROS. Then, a mathematical optimization problem in functional space is proposed to estimate the backward reachable set of the unsafe set, the complementary of which is the ROS. The optimization problem is interpreted from a geometry point of view, and then converted into a SOS program by using polynomial functions and semi-algebraic sets. A feasible result of the SOS program will generate a barrier certificate. The superlevel set of the barrier certificate over-approximates the backward reachable set of the unsafe set and the sublevel set of it under-approximate the ROS. This barrier certificate is employed as the safety supervisor for hybrid supportive mode synthesis of WTGs. The proposed controller is first verified on a single-machine three-phase nonlinear microgrid model in Simulink. For multi-machine systems, a decentralized SSC is designed particularly for small-scale systems and implemented in IEEE 39-bus system with high renewable penetration modeled in DSATools. Both results indicate that the proposed framework and control configuration can guarantee

adequate response and not conservative at all. In addition, a scheduling loop is proposed so that the supervisor updates its margin with respect to the renewable penetration level in order to be robust to variations in system inertia. The shape change of ROSs with respect to renewable penetration level is demonstrated as well. Finally, the proposed controller is verified in the HTB at CURENT.

Part II

Novel Control Designs and Synthesis

Chapter 5

Frequency Control with Temporal Logic Specifications

In the previous chapters, efforts are devoted into switching behavior synthesis given control input signals. Beginning from this chapter, we search over the space of input signals to obtain trajectories that satisfy certain control specifications by using open-loop numerical optimal control methods as well as closed-loop feedback design.

Till now, performance specifications are only state-dependent. But the protection replays of power system in real industry are designed based on states and dwell time simultaneously. Most of the grid codes also allow states to enter certain restricted regions, but the dwell time should not be larger than a specified value. So, it is natural to seek a tool that can specify both time and region requirements in control designs. The temporal logic specifications (TLSs) allow richer descriptions of specifications including set, logic and time-related properties. For example, to guarantee the proper operation of microgrids, the speed deviation of the synchronous generator should not exceed ± 1.5 Hz for 0.1 second [117]. The pioneering work in [116] introduces the TLSs for controller synthesis of energy storage systems, where the frequency is required to restore back to 60 ± 0.2 Hz within 2 seconds. Inspired by both [126] and [11] and motived by the introduction of TLSs [116], this chapter probes into certain technical methods of control design for frequency to satisfy the TLSs, and proposes a numerical optimal control (NOC)-based synthesis methodology. The reminder of the chapter is organized as follows. Section 5.1 introduces preliminary knowledge about

TLSs. Section 5.2 introduces the NOC-based control synthesis methodology, including the overall configuration, problem formulation, and the results with nonlinear simulation verifications. Conclusions are expressed in Section 5.3. Part of the results in this chapter appeared in [124].

5.1 Preliminaries on Temporal Logic Specification

A temporal logic specification is built by combining the atomic propositions (APs), or predicates, using logical and temporal operators. An AP is a statement on the system variables that is either true or false for some given value of the systems variables [44]. For example, the statement "the grid frequency deviation should never exceed 0.5 Hz" is an AP, formally expressed as $\mu(\bullet) = (|\bullet| \leq 0.5)$. The commonly used logical operators are conjunction ($\wedge$), disjunction ($\vee$), negation ($\neg$), implication ($\rightarrow$), and equivalence ($\leftrightarrow$). The temporal operators include eventually ($\Diamond$), always ($\Box$), and until (U). The TLSs can be categorized into two groups, that is, discrete-time and continuous-time TLSs. For a discrete-time TLS, timing intervals cannot be added with the temporal operators. For example, $\Diamond p$ for $p = (y < 5)$ states the y will be eventually less than five without specifying when the condition will be fulfilled. Obviously, discrete-time TLS can not be used for reasoning about quantitative properties of time. As a supplementary, a continuous-time TLS can add the timing intervals like $\Diamond_{[2,+]}p$ for $p = (y < 5)$, which states the y will be eventually less than five after two seconds. For frequency control problem, the continuous-time TLSs are employed.

The validity of a formula φ with respect to a signal or state of a system, denoted by x, at time t is defined inductively as follows [87]

$$(x,t) \models \mu \quad \Leftrightarrow \quad \mu(x(t)) > 0 \tag{5.1}$$

$$(x,t) \models \neg\mu \quad \Leftrightarrow \quad \neg((x,t) \models \mu) \tag{5.2}$$

$$(x,t) \models \psi \wedge \varphi \quad \Leftrightarrow \quad (x,t) \models \psi \wedge (x,t) \models \varphi \tag{5.3}$$

$$(x,t) \models \psi \vee \varphi \quad \Leftrightarrow \quad (x,t) \models \psi \vee (x,t) \models \varphi \tag{5.4}$$

$$(x,t) \models \Box_{[a,b]}\varphi \quad \Leftrightarrow \quad \forall\tau \in [t+a, t+b], (x,\tau) \models \varphi \tag{5.5}$$

$$(x,t) \models \Diamond_{[a,b]}\varphi \quad \Leftrightarrow \quad \exists\tau \in [t+a, t+b], (x,\tau) \models \varphi \tag{5.6}$$

Considerable efforts have been devoted to control synthesis for continuous-time TLSs. On the one hand, in [116, 113], the temporal logic constraints are substituted into the optimization objectives, leading to a unconstrained problem that can be solved by some functional gradient descent algorithms. On the other hand, the authors in [87] introduce an approach using mixed-integer convex optimization to encode the TLSs as constraints. First, the safe or unsafe sets are represented as polyhedrons (by finite many hyperplanes). An AP like $x \in P$ can be formulated as a linear program. Second, some integer variables are introduced to indicate whether the condition holds or not. The if and else condition can be formulated in the linear program using the big-M technique. Finally, the overall problem becomes a mixed integer linear program (MILP). In [92], a heuristic algorithm is proposed. By adding constraints to satisfy the TLS formula only when necessary, the exponential complexity of solving MILP problems is avoided.

5.1.1 Model Checking via Mixed Integer Linear Programming

Model checking or property checking refers to the following problem: Given a model of a system, exhaustively and automatically check whether this model meets a given specification. In order to solve such a problem algorithmically, both the model of the system and the specification are formulated in some precise mathematical language. MILP has been successfully applied to the satisfiability problem for propositional logic in [33], where the

linear temporal logic is converted into mixed integer linear constraints. In addition, this technique has been successfully applied into optimal control problems of mixed logical dynamical systems [45], and the vehicle routing problem with linear temporal logic [41, 42] as well as metric temporal logic [43]. The MILP encoding procedure has been implemented in the Matlab toolbox BluSTL [20], and employed for model predictive control in [87]. In this study, the formulation technique for continuous-time temporal logic in [87] is employed and briefly introduced here.

Atomic Propositions

APs are the elementary units building the TLSs. The encoding procedure starts with translating APs in Eq. (5.1) into linear constraints. To do this, arbitrary sets in APs are approximately represented by polyhedrons, that is, by finite many hyperplanes. Formally, an AP is denoted as $\mu = (Ax > b)$. To indicate (for verification) or enforce (for synthesis) the satisfaction of an AP with respect to the signal or state of a system x at time t, denoted as x_t for short, binary variables z_t^μ for AP μ at time $t = 0, 1, \cdots, N$ are introduced, and the big-M technique is employed as follows

$$\begin{aligned} \mu(x_t) &\leq M z_t^\mu - \epsilon \\ -\mu(x_t) &\leq M(1 - z_t^\mu) - \epsilon \end{aligned} \tag{5.7}$$

where M are sufficiently large positive numbers, and ϵ are sufficiently small positive numbers that prevent $\mu(x_t)$ from equaling to zero. Obviously, $z_t^\mu = 1$ indicates or enforces the satisfaction of μ.

Logic Operators

Using the binary indicators, Eq. (5.2) can be formulated as

$$z_t^{\neg\mu} = 1 - z_t^\mu \tag{5.8}$$

For the conjunction operator $\varphi = \mu_1 \wedge \mu_2 \wedge \cdots \wedge \mu_m$, the MILP formulation is expressed as follows

$$\begin{aligned} z_t^{\varphi} &\leq z_t^{\mu_i}, i = 1, \cdots, m \\ z_t^{\varphi} &\geq 1 - m + \sum_i^m z_t^{\mu_i} \end{aligned} \tag{5.9}$$

For the disjunction operator $\varphi = \mu_1 \vee \mu_2 \vee \cdots \vee \mu_m$, the MILP formulation is expressed as follows

$$\begin{aligned} z_t^{\varphi} &\geq z_t^{\mu_i}, i = 1, \cdots, m \\ z_t^{\varphi} &\leq \sum_i^m z_t^{\mu_i} \end{aligned} \tag{5.10}$$

The implication operator $\varphi = \mu_1 \Rightarrow \mu_2$ is logically equivalent to $\varphi = (\neg\mu_1) \vee \mu_2$. The equivalence operator $\varphi = \mu_1 \Leftrightarrow \mu_2$ is logically equivalent to $\varphi = (\mu_1 \Rightarrow \mu_2) \wedge (\mu_2 \Rightarrow \mu_1)$. Thus, the formulations in Eqs. (5.8)-(5.10) can be used.

Temporal Operator

To achieve algorithmic solutions, the discretized time and state spaces are considered. In addition, finite-time horizon from 1 to N is considered. The most general expressions of the temporal operators for an AP μ are $\Box_{[t+a,t+b]}\mu$ and $\Diamond_{[t+a,t+b]}\mu$, where $b > a$ and $t \in [1, N-(b-a)]$. In other words, the duration that the property is satisfied over is given, but the instant is unknown, which probably depends on other variables like control inputs. In this case, all possible scenarios should be considered with the constraint that only one will become true.

For example, we would like to encode the formula $\varphi = \Box_{[\tau+a,\tau+b]}\mu$ and $\mu = (y < 1)$, where the duration is assumed to be 4 without loss of generality, and y is the output of a system. The formula φ could be true any time once on a finite-time interval $[1, N]$. The instant of event τ is to be determined by other factors such as the dynamics of the system and control input. The encoding objective is to define a binary indicator for formula φ. First, let z_t^{μ} be the indicator of μ at time t, and z_t^{φ} be the indicator of the scenario that φ becomes true at time t. Second, generate all possible scenarios for φ in the time interval $[1, N]$ as illustrated in Fig. 5.1. Third, based on Eqs. (5.5) and (5.6) and duration, create

logic constraints inductively between z_t^{μ} and z_t^{φ}, which is also shown in Fig. 5.1. Finally, enforce the following constraint so that φ could only become true once

$$z^{\varphi} = \sum_{t=1}^{N-(b-a)} z_t^{\varphi} = 1 \tag{5.11}$$

where z^{φ} is the indicator of φ on the time interval $[1, N]$. If φ is enforced to be true starting at a specific instant k, then the corresponding indicator z_k^{φ} can be used directly.

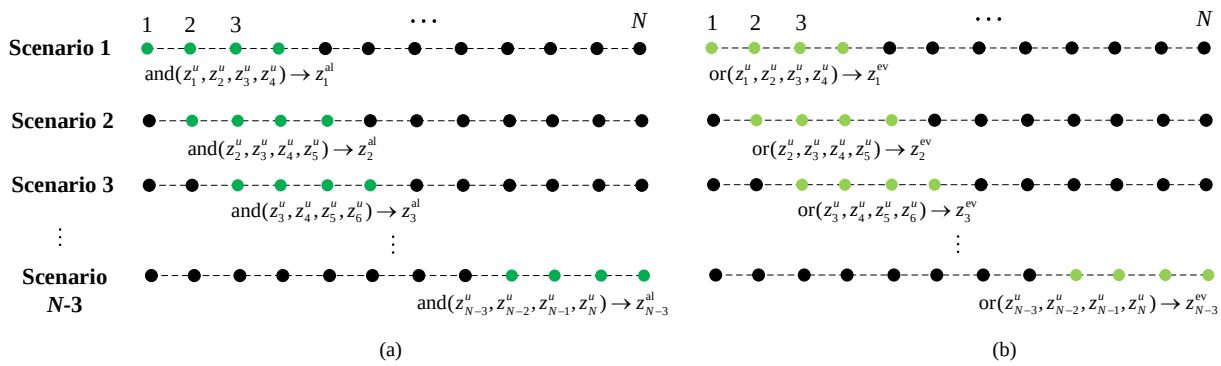

Figure 5.1: Illustration of encoding temporal operators into MILP. (a) Temporal operator: always. (b) Temporal operator: eventually.

5.2 NOC-based Control Synthesis with Temporal Logic Specifications

5.2.1 Overall Configuration

The overall configuration of the proposed control is illustrated in Fig. 5.2. The controller is configured into two levels, that is, the scheduling level and the triggering level. In the scheduling level, the grid operating status is acquired to update the parameters of the ASFR model. The required performance specifications and up-to-date models are sent to the NOC-based signal scheduling program. The signals are Boolean with pre-specified magnitude. The signal scheduling problem is formulated as a MILP. Then, the supportive signals for WTGs can be pre-calculated under a worst-credit contingency.

The scheduled signals are sent to the triggering level, where the frequency is measured and compared to a pre-defined threshold to detect whether a severe contingency close to the worst-case one is happening. Once the supportive function is determined to be activated, a local clock is activated so that the scheduled signals are synchronized with the real time. And the synchronized signals are applied to the supplementary loop of the WTGs. It is worth mentioning that the initial condition in the NOC scheduling should be aligned with the threshold setting. The overall configuration is analogous to the adaptive remedial action scheme in [61].

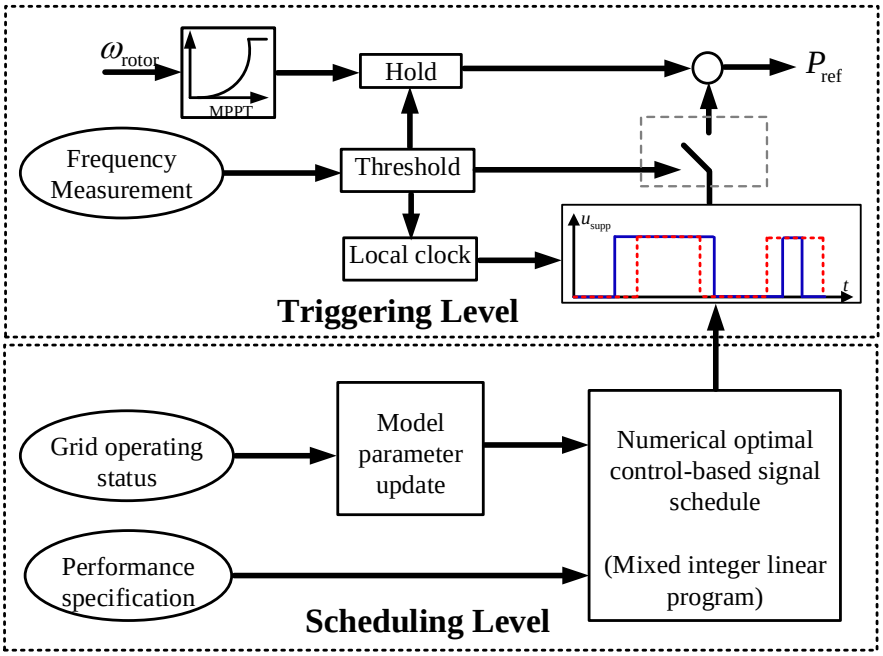

Figure 5.2: Overall configuration of synthesizing performance guaranteed controller.

5.2.2 Test System 33-Node Based Microgrid

Consider a diesel-wind mixed microgrid in Fig. 5.3. The ASFR model in 2.40 can be adopted with modifications as follows

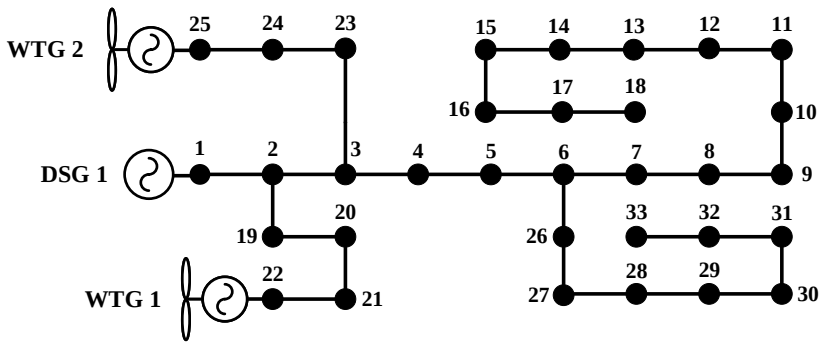

Figure 5.3: Diesel-wind fed 33-node based microgrid.

$$
\begin{aligned}
&2H_d\Delta\dot{\omega}_d = \overline{f}(\Delta P_m - k_d\Delta P_d + k_{dw1}\Delta P_{g1} + k_{dw2}\Delta P_{g2}) \\
&\tau_d\Delta\dot{P}_m = -\Delta P_m + \Delta P_v \\
&\tau_g\Delta\dot{P}_v = -\Delta P_v - \Delta\omega_d/(\overline{f}R_D) \\
&\Delta\dot{\omega}_{r1} = A_{\mathrm{rd1}}\Delta\omega_{r1} + B_{\mathrm{rd1}}u_{s1} \\
&\Delta\dot{\omega}_{r2} = A_{\mathrm{rd2}}\Delta\omega_{r2} + B_{\mathrm{rd2}}u_{s2}
\end{aligned}
\tag{5.12}
$$

where

$$
\begin{aligned}
\Delta P_{g1} &= C_{\mathrm{rd1}}\Delta\omega_{r1} + D_{\mathrm{rd1}}u_{s1} \\
\Delta P_{g2} &= C_{\mathrm{rd2}}\Delta\omega_{r2} + D_{\mathrm{rd2}}u_{s2}
\end{aligned}
\tag{5.13}
$$

Let S_d, S_{w1} and S_{w2} be the base of DG and WTG 1 and 2, respectively. Then, $k_d = 1/S_d$, $k_{dw1} = S_{w1}/S_d$, and $k_{dw2} = S_{w2}/S_d$. The term ΔP_d is the worst-case contingency.

5.2.3 NOC Formulation for Scheduling Level

Define the state and input vectors as

$$
\begin{aligned}
x &= [\Delta\omega_d, \Delta P_m, \Delta P_v, \Delta\omega_{r1}, \Delta\omega_{r2}]^T \\
u &= [u_{s1}, u_{s2}]^T
\end{aligned}
\tag{5.14}
$$

Then, the analytical model in (5.12) is discretized at a sample time of t_s and expressed compactly as follows

$$x(k+1) = A_d x(k) + B_{d1} u(k) + B_{d2} k_d \Delta P_d \tag{5.15}$$

Let the scheduling horizon be denoted as $k \in \mathcal{T} = [1, \cdots, T]$. First, the frequency deviation should not exceed a certain limit in any time, that is,

$$|x_1(k)| \leq \Delta f_{d,\text{lim}} \quad \forall k \in \mathcal{T} \tag{5.16}$$

Since the kinetic energy of WTGs will be transferred to active power to support the grid, the speed of WTGs will decrease from nominal values. This deviation is also desired to be limited for both WTGs

$$|x_i(k)| \leq \Delta f_{w,\text{lim}} \quad \forall k \in \mathcal{T}, i = 4, 5 \tag{5.17}$$

The Boolean control signals for both WTGs can be presented using the following constraints

$$u_{si}(k) = b_i(k) u_C \quad \forall k \in \mathcal{T}, i = 1, 2 \tag{5.18}$$

where b_i is a binary variable indicating the status of the GS mode of WTG i, and u_C is the fixed magnitude of the inputs. Finally, the frequency is required to satisfy the following TLS φ to enhance the performance

$$x_1(k) \vDash \varphi \quad \forall k \in \mathcal{T} \tag{5.19}$$

where

$$\varphi = \Box[(|x_1(k)| \geq \Delta f_c) \rightarrow \Diamond_{[0,t_a]} \Box(|x_1(k)| \leq \Delta f_c)] \tag{5.20}$$

The above TLS states that whenever the frequency deviation is larger than Δf_c, then it should become less than Δf_c within t_a seconds.

The first objective is to minimize the control efforts. The total control effort can be represented as the summation of all binary variables as

$$C_U = \sum_{i=1}^{2} \sum_{k=1}^{T} b_i(k) \tag{5.21}$$

In addition, the switching between on and off of the supportive modes should not be too frequent. Thus, a start-up cost is added as follows

$$C_{SU} = \sum_{i=1}^{2} \sum_{k=2}^{T-1} b_i(k)[1 - b_i(k-1)] \tag{5.22}$$

This nonlinear objective can be converted into a linear objective with constraints by introducing slack binary variable z as follows

$$C'_{SU} = \sum_{i=1}^{2} \sum_{k=2}^{T-1} (b_i(k) - z_i(k)) \tag{5.23}$$

and

$$\begin{aligned} &z_i(k) \leq b_i(k), z_i(k) \leq b_i(k-1) \\ &z_i(k) \geq b_i(k) + b_i(k-1) - 1 \quad \forall k \in \mathcal{T}, i = 1, 2 \end{aligned} \tag{5.24}$$

The scheduling problem can be summarized as follows

$$
\begin{aligned}
&\min \quad w_1 C_U + w_2 C'_{SU} \\
&\text{s.t.} \quad \forall k \in \mathcal{T} \\
&x(k+1) = A_d x(k) + B_{d1} u(k) + B_{d2} k_d \Delta P_d \\
&|x_1(k)| \leq \Delta f_{d,\text{lim}} \\
&|x_i(k)| \leq \Delta f_{w,\text{lim}} \quad i = 4, 5 \\
&u_i(k) = b_i(k) u_C \quad i = 1, 2 \\
&z_i(k) \leq b_i(k), z_i(k) \leq b_i(k-1) \quad i = 1, 2 \\
&z_i(k) \geq b_i(k) + b_i(k-1) - 1 \quad i = 1, 2 \\
&x_1(k) \vDash \varphi \\
&\varphi = \Box[(|x_1(k)| \geq \Delta f_c) \rightarrow \Diamond_{[0,t_a]} \Box(|x_1(k)| \leq \Delta f_c)]
\end{aligned}
\tag{5.25}
$$

where w_1 and w_2 are positive weighing factors. The TLS can be encoded into a MILP using the toolbox BluSTL [20]. Then, the overall problem is converted into a MILP, written in the format of Yalmip [54] and solved by efficient solvers Mosek [7] and Gurobi.

5.2.4 Results and Simulation Verification

The rated powers of DG and WTG are assumed to be 2 MW and 1 MW, respectively. The operating conditions of the WTGs and their corresponding first-order model are given as follows

$$
\begin{aligned}
&v_{\text{wind}} = 10 \text{ [m/s]}, P_{gi} = 0.8, Q_{gi} = 0, v_{dsi} = 0, v_{qsi} = 1 \\
&A_{\text{rd}i} = -0.2771, B_{\text{rd}i} = 2.5741, C_{\text{rd}i} = 0.2550, D_{\text{rd}i} = -2.3343
\end{aligned}
$$

for $i = 1, 2$. The parameters associated with the DG are given as follows

$$
H_d = 4, \tau_d = 0.1, \tau_g = 0.5
$$

The base and scaling factors are

$$S_d = 5 \text{ [MVA]}, S_w = 1.11 \text{ [MVA]}, k_d = 0.2, k_{wd} = 0.22$$

The parameters in the MILP are given as follows

$$\begin{aligned}
&t_s = 0.02 \text{ [s]}, T = 4 \text{ [s]}, P_d = 0.7 \text{ [MW]}, w_1 = 1, w_2 = 10 \\
&\Delta f_{d,\text{lim}} = 0.5 \text{ [Hz]}, \Delta f_{w,\text{lim}} = 2 \text{ [Hz]}, u_C = -0.05 \\
&f_c = 0.45 + \varepsilon \text{ [Hz]}, t_a = 1 \text{ [s]}
\end{aligned}$$

Based on the given parameters, it is required that the frequency deviation to be limited within 0.5 Hz. Moreover, whenever the frequency deviation is larger than 0.45 Hz, it should be restored back to 0.45 Hz within one second. Since there exists certain mismatches between the ASFR and the full nonlinear model, the term ε is introduced to tighten the specification such that the nonlinear response can satisfy the original specification as well.

Three cases are considered. In the first case, the TLS is removed. In the second case, the TLS is considered with the compensating factor $\varepsilon = 0$. In the third case, the compensating factor ε is set to be -0.015 Hz. The scheduled inputs of these three cases are plotted in Fig. 5.4. The DG frequencies under these cases from the AFR are shown in Fig. 5.5. As shown, with more constraints, the WTGs are required to operate at the GS mode for larger time durations. The responses from the AFR model strictly satisfy all control specifications with minimum control efforts required.

The scheduled inputs of Case 2 and 3 are applied to the nonlinear model. The corresponding frequencies of DG are shown in Fig. 5.6. The DG frequency in Case 2 does not satisfy the TLS. This is because of the error induced by the model reduction of WTGs. The active power variations associated with the support signals in Case 3 are shown in Fig. 5.7. As shown, although the first-order models have successfully captured the active power dynamics with good accuracy, there are still mismatches in the response. These tiny mismatches, however, falsify the TLS, the satisfaction of which requires higher level precision. Thus, the response mismatches need to be compensated. The most convenient approach is to impose more strict specifications, that is, the introduction of the robust factor ε, such that

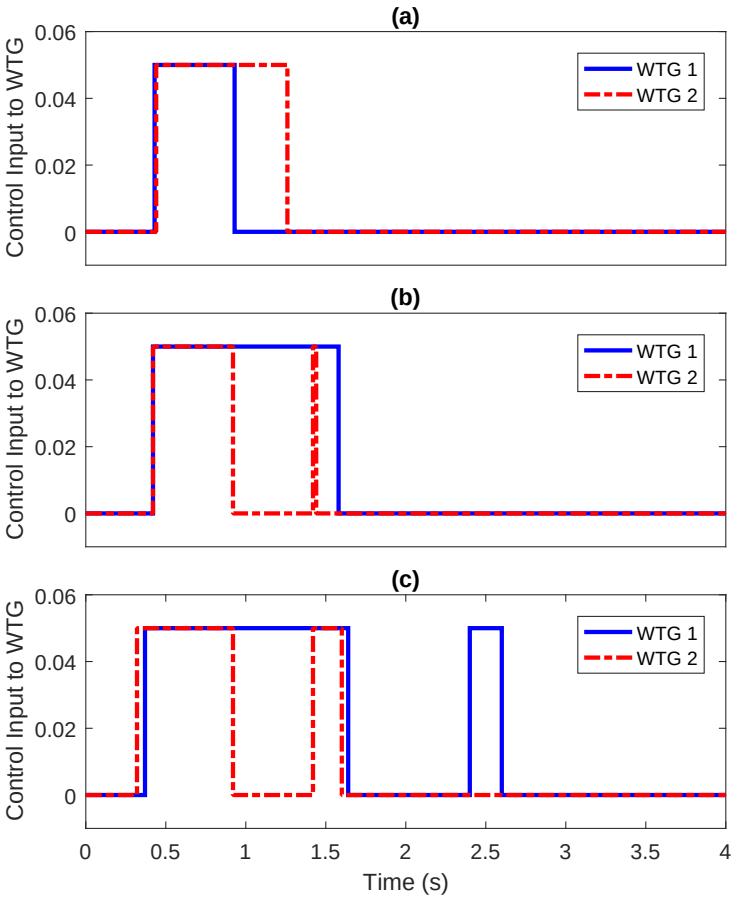

Figure 5.4: Scheduled control signals for WTGs. (a) Without TLS. (b) With TLS. (c) With TLS and a robust margin.

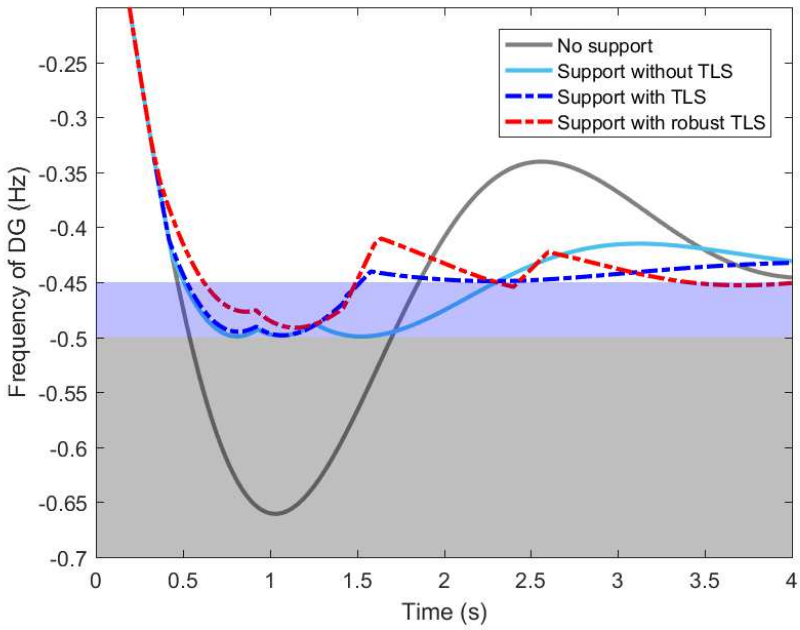

Figure 5.5: Frequencies of DG under different cases simulated using the AFR model.

the output could satisfy the original specifications at the cost of introducing certain levels of conservatism. The red dash plot in Fig. 5.6 indicates that this robust factor could generate a stronger control effort so that the specifications are satisfied. It is also worth mentioning that in the nonlinear verification, the TLS is a bit conservative because the ASFR model is not able to capture the weak inertial responses from the DFIG-based WTGs.

5.3 Summary

In this chapter, a NOC-based control synthesis methodology is proposed that enables the realization of the TLSs. The controller schedules ahead a series of Boolean control signals to synthesize the GS mode of WTGs by solving the NOC problem, where the frequency response predicted by the AFR model satisfies the defined specifications under a worst-case contingency. The proposed control is verified on the full nonlinear model in Simulink. A robust factor is introduced to compensate the model reduction error such that the nonlinear response satisfies the TLS.

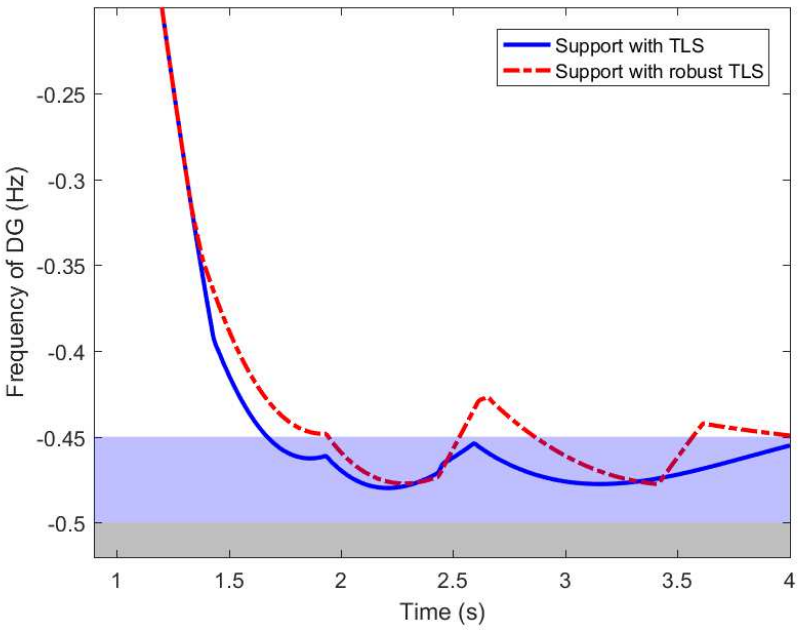

Figure 5.6: Frequencies of DG under different cases simulated using the full nonlinear model in Simulink.

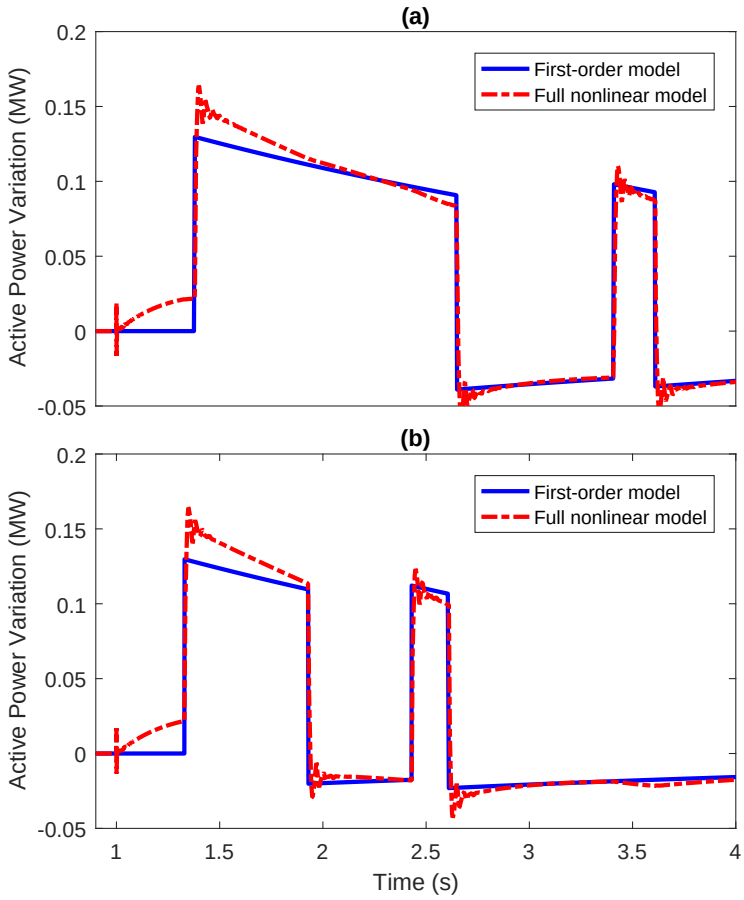

Figure 5.7: Active power variations from the first-order and full nonlinear model. (a) WTG 1. (b) WTG 2.

Chapter 6

Model Reference Control-Based Inertia Emulation

Classic inertia emulation approach feeds the ROCOF into the supplementary loop of a WTG to couple the kinetic energy with the grid frequency events [65, 46]. However, it is difficult to assess how much synthetic inertia can be provided through this loop during a disturbance. There are a few works trying to approximate the inertia contribution [110, 62, 47, 126]. Refs. [110] and [126] indicate that under current existing inertia control, the emulated inertia is time-varying. Thus, emulating desired inertia over a time window is impossible using the ROCOF as the control input. Under some specific control structures, such as, droop control or virtual synchronous generators (VSG), the synthetic inertia can be estimated or controlled [19], but this requires the WTG to operate as voltage sources and at the cost of de-loaded operation.

Motivated by these issues, a novel inertia emulation strategy for current-mode WTGs is proposed. The model reference control (MRC) concept [24] is employed to provide the capability of precisely emulating inertia. A frequency response model is defined as the reference model, where the desired inertia is parametrically defined. A measurement at a specific location delivers the information about the disturbance acting on the diesel-wind system to the reference model. Then, a static state feedback control law is designed to ensure the frequency of the physical plant tracks the reference model so that the desired

inertia is emulated. In spirit, this proposed control strategy is similar to the VSG approach but instead uses WTGs and traditional generators together as actuators.

The rest of the chapter is organized as follows. Section 6.1 describes the challenges of the proposed objective from the physical point of view in details. The MRC-based inertia emulation strategy is presented in Section 6.2. Three-phase nonlinear simulation illustrates performance in Section 6.3 followed by conclusions in Section 6.5. Part of the results in this chapter appeared in [122] and [123].

6.1 Problem Statement

The natural inertial response (NIR) refers to the kinetic energy of electric machines that transfers into electric power per unit time to overcome the immediate power imbalance. It can be expressed mathematically by the swing equation

$$\underbrace{2Hs\Delta\omega}_{\text{NIR}} = \Delta P \tag{6.1}$$

where s is the Laplace operator, H is the inertia constant, $\Delta\omega$ is the frequency variation and ΔP is the power imbalance. The left side of (6.1) can be regarded as the NIR. For a WTG, the power imbalance is invisible to the electric machine as the electromagnetic torque is controlled by the converter interface, and is a constant in most times. Inertia emulation is to let the electric machine sense the power imbalance and release its kinetic energy in proportion to the ROCOF as illustrated in Fig. 6.1 (a). The generated power due to this effort, denoted by ΔP_{ie}, is referred to as the virtual inertial response (VIR). This procedure can be mathematically modeled in Fig. 6.1 (b), where $G_w(s)$ represents the responding dynamics of WTG to generate ΔP_w according to the inertia emulation (IE) command u_{ie}.

If the responding dynamics are infinitely fast, that is, $G_w(s) = 1$, then the supportive power can be expressed as

$$\Delta P_w = u_{\text{ie}} = K_{\text{ie}} s \Delta\omega \tag{6.2}$$

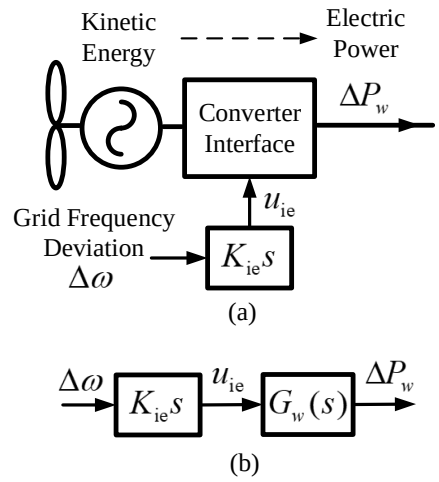

Figure 6.1: Inertia emulation using WTGs. (a) Control diagram. (b) Equivalent mathematical model.

Subjected to this supportive power, Eq. (6.1) will become

$$2Hs\Delta\omega = \Delta P + \Delta P_w \tag{6.3}$$

Substituting ΔP_w with the right hand side of (6.2) will yield

$$\underbrace{2Hs\Delta\omega}_{\text{NIR}} - \underbrace{K_{\text{ie}}s\Delta\omega}_{\text{VIR}} = \Delta P \tag{6.4}$$

As shown, the WTG support can be equivalently regarded as a constant added to the inertia constant. In this case, both sides of Eq. (6.2) are referred to as the ideal VIR.

However, $G_w(s)$ cannot be infinitely fast. It can be further decomposed into the dynamics of rotor and its regulator $G_r(s)$, DC-link and its regulator $G_d(s)$, and stator current regulator $G_s(s)$, the timescales of which are seconds, 100 ms, and 10 ms, respectively [102]. As seen in Fig. 6.2, the upper bandwidth limit for ideal VIR is the stator current regulator. Thus, the phrase "near-ideal" is used to express this physical limit, although both $G_d(s)$ and $G_s(s)$ are sufficiently fast to have sizable impacts on the frequency control problem. The lower limit, on the other hand, is determined by the rotor and its regulator $G_r(s)$, which has the most

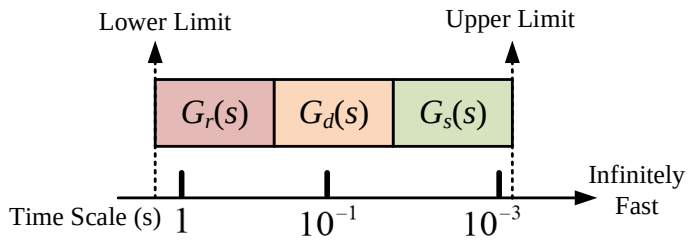

Figure 6.2: Decomposition of WTG responding model and their time scale. The upper and lower bandwidth limits for ideal VIR are identified.

dominant impact on the non-ideal effect of VIR, and prohibits the WTG from providing near-ideal VIR.

6.2 Model Reference Control-Based Inertia Emulation

6.2.1 Configuration Interpretation

Fig. 6.3 illustrates the MRC-based inertia emulation on a diesel-wind system. It consists of a parameterized reference model and a physical plant. Although theoretically any model can be chosen, a large difference between the reference model and the physical one will lead to mathematical infeasibility when seeking feedback controllers. Therefore, a reference model similar to Eq. (2.5) will be chosen with desired inertia $\hat{H}$. The physical plant is the diesel-wind unit.

The idea to achieve near-ideal synthetic inertial response of WTGs discussed in Section 6.1 can be recast as a tracking problem. As illustrated in Fig. 6.3, let $2\hat{H}s\Delta\omega$ and $2H_D s\Delta\omega_d$ be the inertial response of the reference model and DSG, respectively, where $\hat{H}$ is the desired inertia constant and $\hat{H} - H_D = H_{\text{ie}} > 0$. Once subjected to a same disturbance ΔP_{pom}, the power balance condition holds as

$$\Delta P_{\text{pom}} = 2\hat{H}s\Delta\omega = 2H_D s\Delta\omega_d + \Delta P_g \tag{6.5}$$

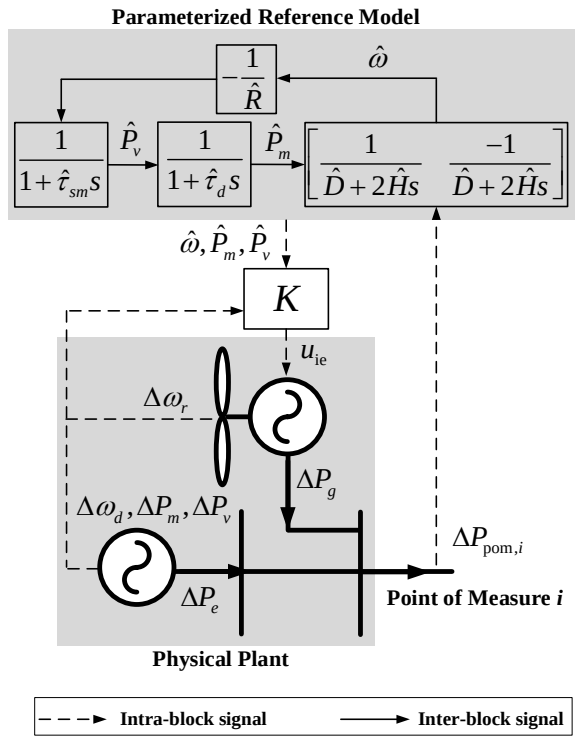

Figure 6.3: Realization of MRC on one diesel-wind system. Power deviation at the point of measure is measured and sent to the parameterized reference model. Four states from the physical plant and three states from the reference model are measured for feedback control.

If the speed of DSG can track the speed of reference model with the support of WTG, that is, $\Delta\omega = \Delta\omega_d$, then the following relation holds

$$\Delta P_g = 2\hat{H}s\Delta\omega - 2H_D s\Delta\omega = 2H_{\text{ie}}s\Delta\omega \tag{6.6}$$

Therefore, exact synthetic inertial response $2H_{\text{ie}}s\Delta\omega$ is emulated by the WTG. Finally, the MRC approach is employed to realize the tracking objective. This reference tracking can be realized by means of feedback control, which will be designed in Section 6.2.2.

The key for successful performance guarantees is to impose the disturbance suffered by the physical plant on the reference model. To do this, the power variations of all lines for the diesel-wind unit that feed power into the network are measured and sent to the reference model as disturbances. Due to the radial structure of most distribution networks, usually

there is one such path as shown in Fig. 6.3. We denote the line where the measurement is taken as the point of measurement (POM).

In spirit, this MRC-based inertia emulation is similar to the VSG control, where a reference model is also needed and the POM is the converter terminal bus. The difference is that in VSG the converter is controlled in voltage mode and does not need other voltage sources nearby. The reference model in both control systems can be regarded as an observer that provides the desired response. Note that the proposed configuration can also be used for coordination of flexible numbers of diesel and WTGs by appropriately choosing the POM.

6.2.2 Feedback Controller Design For Reference Tracking

Although state feedback control is implemented in this paper, the reduced-order model is employed to reduce the complexity of the communication link. Moreover, physically the reduced-order model only contains the mechanical states which are easier to obtain by means of state estimation. Taking this into account, the state measure procedure will be simplified by considering a time delay.

To arrive at an aggregated model of DSG and WTG, the electric power in (2.5) is substituted as

$$\Delta P_e = \Delta P_{\text{pom}} - \Delta P_g \tag{6.7}$$

where ΔP_{pom} is the measured power flow variation at the location illustrated in Fig. 6.3, and is regarded as the disturbance. Then, combining (2.5), (2.34) and (6.7) yields the reduced-order model of the physical plant

$$\begin{aligned} \dot{x}_p &= A_p x_p + B_p u_p + E_p w_p \\ y_p &= C_p x_p \end{aligned} \tag{6.8}$$

where states, control input, disturbance and output measurement are defined as

$$\begin{aligned} x_p &= [\Delta\omega_d, \Delta P_m, \Delta P_v, \Delta\omega_r]^T \\ w_p &= \Delta P_{\text{pom}}, u_p = u_{\text{ie}}, y_p = \Delta\omega_d \end{aligned} \tag{6.9}$$

and the matrices are

$$A_p = \begin{bmatrix} 0 & \frac{\overline{f}}{2H_D} & 0 & \frac{\overline{f}C_{\text{rd}}}{2H_D} \\ 0 & -\frac{1}{\tau_d} & \frac{1}{\tau_d} & 0 \\ \frac{1}{\overline{f}\tau_{sm}R_D} & 0 & -\frac{1}{\tau_{sm}} & 0 \\ 0 & 0 & 0 & A_{\text{rd}} \end{bmatrix}, B_p = \begin{bmatrix} \frac{\overline{f}D_{\text{rd}}}{2H_D} \\ 0 \\ 0 \\ B_{\text{rd}} \end{bmatrix}$$

$$E_p = \begin{bmatrix} -\frac{\overline{f}}{2H_D} & 0 & 0 & 0 \end{bmatrix}^T, C_p = \begin{bmatrix} 1 & 0 & 0 & 0 \end{bmatrix}$$

Note that the above definitions hold only when the power flow equation in (6.7) holds, which means the power variation measured at POM has to come from the DSG and WTG only. Fortunately, it is true for most cases as long as there is no fault through the path.

Similarly, the reference model is defined as

$$\begin{aligned} \dot{x} &= A_r x_r + E_r w_r \\ y_r &= C_r x_r \end{aligned} \tag{6.10}$$

where the states, disturbance and output measurement are given as

$$\begin{aligned} x_r &= \left[\Delta\hat{\omega}, \Delta\hat{P}_m, \Delta\hat{P}_v\right]^T \\ w_r &= \Delta P_{\text{pom}}, y_r = \Delta\hat{\omega} \end{aligned} \tag{6.11}$$

and the matrices are

$$A_r = \begin{bmatrix} -\frac{\overline{f}\hat{D}}{2\hat{H}} & \frac{\overline{f}}{2\hat{H}} & 0 \\ 0 & -\frac{1}{\hat{\tau}_d} & \frac{1}{\hat{\tau}_d} \\ \frac{1}{\overline{f}\hat{\tau}_{sm}\hat{R}} & 0 & -\frac{1}{\hat{\tau}_{sm}} \end{bmatrix} E_r = \begin{bmatrix} -\frac{\overline{f}}{2\hat{H}} \\ 0 \\ 0 \end{bmatrix}$$

$$C_r = \begin{bmatrix} 1 & 0 & 0 \end{bmatrix}$$

Assume that the controller admits the following form

$$u_p = K_p x_p + K_r x_r \tag{6.12}$$

Then, the augmented closed-loop system is

$$\begin{aligned}\dot{x}_{\mathrm{cl}}(t) &= \bar{A}x_{\mathrm{cl}}(t) + \bar{B}x_{\mathrm{cl}}(t-\nu(t)) + \bar{E}w_{\mathrm{cl}}(t)\\ e(t) &= \bar{C}x_{\mathrm{cl}}(t) + \bar{D}x_{\mathrm{cl}}(t-\nu(t))\end{aligned} \tag{6.13}$$

where

$$\begin{aligned}&x_{\mathrm{cl}}(t) = [x_p(t), x_r(t)]^T, w_{\mathrm{cl}}(t) = [w_p(t), w_r(t)]^T\\ &e(t) = y_p(t) - y_r(t), \bar{C} = [C_p, -Cr], \bar{D} = [D_pK_p, D_pK_r]\\ &\bar{A} = \begin{bmatrix} A_p & 0 \\ 0 & A_r \end{bmatrix}, \bar{E} = \begin{bmatrix} E_p & 0 \\ 0 & E_r \end{bmatrix}\\ &\bar{B} = \begin{bmatrix} B_pK_p & B_pK_r \\ 0 & 0 \end{bmatrix}\end{aligned}$$

The time delay in Eq. (6.13) is bounded by $\eta_m \leq \nu(t) \leq \kappa$.

The objective is to eliminate as much as possible the tracking error $e(t)$ under any disturbances $w_{\mathrm{cl}}(t)$. To achieve a feasible solution, $w_{\mathrm{cl}}(t)$ is assumed to be a $\mathcal{L}_2$ signal, that is, has finite energy. Then the problem, in a sub-optimal sense, is equivalently expressed as

$$\min ||T_{ew}||_\infty < \gamma \quad \text{for } \gamma > 0 \tag{6.14}$$

where T_{ew} is the transfer function of (6.13) from the disturbances $w_{\mathrm{cl}}(t)$ to the tracking error $e(t)$. This is equivalent to solving the following optimization problem.

Theorem 6.1. *Consider the system in* (6.13)*. If there exist scalar variables* $\gamma > 0$*,* $k_a > 0$*,* $k_b > 0$*, matrix variables* $\bar{P} > 0$*,* $\bar{Q} > 0$*,* $\bar{M}_i > 0$ *,*$\bar{U}_i$ *,*$\bar{V}_i$ *,*$i = 1, 2$*, and* $\bar{K}$ *such that the*

following multi-objective optimization problem can be solved

$$\min \quad \gamma + k_a + k_b$$

$$\begin{bmatrix} -k_a I & \bar{K} \\ \bar{K} & -I \end{bmatrix} < 0, \begin{bmatrix} k_b I & I \\ I & -\bar{P} \end{bmatrix} > 0 \tag{6.15}$$

$$\begin{bmatrix} \Theta_{11} & -\bar{U}_1 + \bar{V}_1^T & \widetilde{B}\bar{K} & \bar{U}_1 & 0 & \bar{E} & \bar{P}\bar{C}^T & \bar{P}\bar{A}^T & \bar{P}\bar{A}^T \\ * & \Theta_{22} & -\bar{U}_2 + \bar{V}_2^T & \bar{V}_1 & \bar{U}_2 & 0 & 0 & 0 & 0 \\ * & * & -\bar{V}_2^T - \bar{V}_2 & 0 & \bar{V}_2 & 0 & \bar{K}D_p^T & \bar{K}\widetilde{B}^T & \bar{K}\widetilde{B}^T \\ * & * & * & -\eta_m^{-1}\Upsilon_1 & 0 & 0 & 0 & 0 & 0 \\ * & * & * & * & -\kappa^{-1}\Upsilon_2 & 0 & 0 & 0 & 0 \\ * & * & * & * & * & -\gamma I & 0 & \bar{E}^T & \bar{E}^T \\ * & * & * & * & * & * & -I & 0 & 0 \\ * & * & * & * & * & * & * & -\eta_m^{-1}\bar{M}_1 & 0 \\ * & * & * & * & * & * & * & * & -\kappa^{-1}\bar{M}_2 \end{bmatrix} < 0 \tag{6.16}$$

where

$$\begin{aligned} \widetilde{B} &= [B_p^T, 0]^T \\ \Theta_{11} &= \bar{A}\bar{P} + \bar{P}\bar{A}^T + \bar{Q} + \bar{U}_1{}^T + \bar{U}_1 \\ \Theta_{22} &= -\bar{Q} - \bar{V}_1{}^T - \bar{V}_1 + \bar{U}_2{}^T + \bar{U}_2 \\ \Upsilon_i &= \bar{M}_i - 2\bar{P}, i = 1, 2 \end{aligned} \tag{6.17}$$

Then, the state feedback controller given in (6.18) *can guarantee that the system in* (6.13) *will attain output tracking performance* $\sqrt{\gamma}$ *in the* $\mathcal{H}_\infty$ *sense*

$$K = [K_p, K_r] = \bar{K}\bar{P}^{-1} \tag{6.18}$$

The linear matrix inequalities (LMIs) in (6.16) is derived based on Lyapunov–Krasovskii functional with the performance guarantees $||e||_2 < \sqrt{\gamma}||w_{\text{cl}}||_2$ [24]. Eq. (6.15) is to limit the

size of gain matrix K. Since $K = \bar{K}\bar{P}^{-1}$, one can have

$$\bar{K}^T\bar{K} < k_a I, \quad \bar{P}^{-1} < k_b I \tag{6.19}$$

for arbitrary scalars $k_a > 0$ and $k_b > 0$. Then, the gain matrix becomes

$$K^T K = \bar{P}^{-1}\bar{K}^T\bar{K}\bar{P}^{-1} < k_a k_b^2 I \tag{6.20}$$

where (6.19) and (6.15) are equivalent.

6.2.3 Polytopic Parameter Uncertainty

In realistic cases, the parameters of the physical plant cannot be exactly determined but generally reside in a given range. This is a polytopic type of uncertainty that can be described by its vertices. Let the plant matrix A_p with K_a uncertain parameters be denoted as $A_p(\theta_1, \cdots, \theta_i, \cdots, \theta_{K_a})$ where $\theta_i \in [\theta_i^1, \theta_i^2]$ describes the absolute percentage variation of parameter i from its nominal value and $i = 1, \cdots, K_a$. Then, all vertices can be expressed as $A_{p,k_a} = A_p(\theta_i^j)$ for $j = 1, 2$ and $i = 1, \cdots, N$. Similarly, the vertices of matrix B_p, E_p, C_p and D_p can be denoted as B_{p,k_b}, E_{p,k_e}, C_{p,k_c} and D_{p,k_d}. Since the LMI condition in (6.15) and (6.16) is affine in the system matrices, Theorem 6.1 can be directly used for robust tracking control as presented in the following corollary [24].

Corollary 6.2. *The closed-loop system in (6.13) with the polytopic parameter uncertainty described above will achieve $\mathcal{H}_\infty$ output tracking performance $\sqrt{\gamma}$ under the state feedback controller (6.12) if there exists $\bar{P} > 0$, $\bar{Q} > 0$, $\bar{M}_i > 0$,$\bar{U}_i$,$\bar{V}_i$, $i = 1, 2$, and $\bar{K}$ such that Theorem 6.1 is solved for all vertices A_{p,k_a}, B_{p,k_b}, E_{p,k_e}, C_{p,k_c} and D_{p,k_d}.*

Table 6.1: Scheduled Inertia in Reference Model and Other Parameters under Different Configurations

Config.#	OP	Activated MRC System (Involved Physical Units)	$\hat{H}$	$\hat{R}$	$H_{D,1}$	$H_{D,2}$	$R_{D,1}$	$R_{D,2}$	Results
1	A	Reference 1-1 (DSG 1, WTG 1)	3	5%	1	1	5%	5%	Fig. 6.6
2	A	Reference 1-1 (DSG 1, WTG 1), 1-2(DSG 2, WTG 2)	2, 2	5%, 5%	1	1	5%	5%	Fig. 6.9
3	B	Reference 2 (DSG 1, WTG 1 and 2)	5	3.5%	1	NA	3.5%	NA	Fig. 6.10
4	B	Reference 3 (DSG 1, WTG 1, 2 and 3)	5	3.5%	1	NA	3.5%	NA	Fig. 6.10

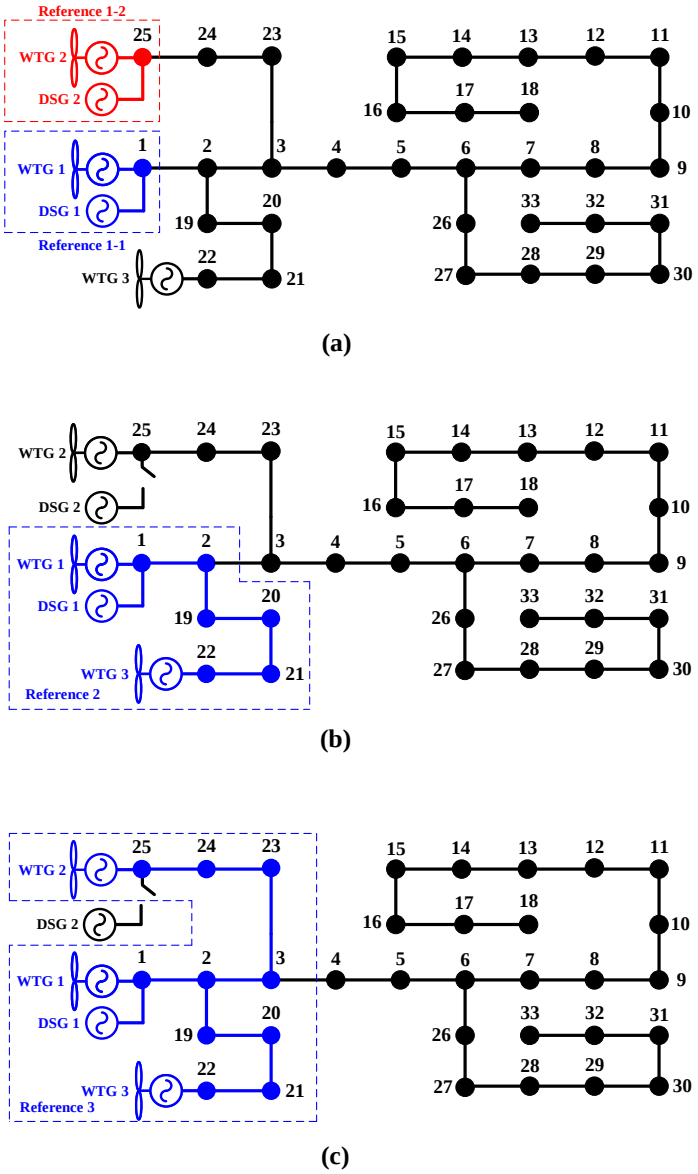

Figure 6.4: Model reference control configured on the 33-node based microgrid. (a) Two separate MRC systems with bus 1 and 25 be the POM, respectively. (b) MRC system incorporating DSG 1, WTG 1 and 3 with bus 2 be the POM. (c) MRC system incorporating DSG 1 and all WTGs with bus 3 be the POM.

6.3 Closed-loop Performance on 33-Node Based Microgrid

In this section, the proposed control will be tested on the 33-node based microgrid in the Simulink environment. Two representative operating points of the system are considered:

- A (heavy loading): $P_{e,1} = P_{e,2} = 1.2$ MW, $P_{g,1} = P_{g,2} = P_{g,3} = 0.8$ MW.
- B (light loading): $P_{e,1} = 1.5$ MW, $P_{e,2} = 0$ MW, $P_{g,1} = P_{g,2} = P_{g,3} = 0.8$ MW.

Four different MRC-based inertia emulation controllers are configured with respect to these operating points, which are illustrated in Fig. 6.4 and summarized in Table 6.1. The network data is acquired from [8]. The WTG model is modified based on the averaged DFIG in the Simulink demo library, where the aerodynamic model is changed to the one described in [86] and the two-mass model is reduced to the swing equation with combined inertia of turbine and generator. The two-axis synchronous machine model of the diesel generator is adopted from [93]. All parameters are scaled to medium-voltage microgrid level based on [72]. For all cases, the time constants of all reference models are set to be equal to those of the DSGs, i.e., $\hat{\tau}_d = 0.2$ s, $\hat{\tau}_{sm} = 0.1$ s. Due to the capacity limits, load-damping effect, which represents the frequency-sensitive loads, is not emulated, and thus $\hat{D} = 0$. Only inertia constants of reference models $\hat{H}$ are scheduled. The power system stabilizers are turned on to damp the oscillation. Other important parameters are given in Appendix A.2.

The responses of nonlinear, full linear, and first-order WTG model with $\delta = 0$ are shown under a step signal (Fig. 6.5 (a)), inertia emulation signal (Fig. 6.5 (b)), and using washout filters (Fig. 6.5). As seen the selected mode successfully captures the active power related dynamics of the full linear system, and the induced error by the SMA-based model reduction is not significant. Based on this result, it is sufficient to consider $\delta = \pm(-A_{22})^{-1}B_z \times 10\%$ for all cases.

6.3.1 Closed-loop Performance of Single Diesel-Wind System

Assume that the system operates under Condition A. The closed-loop performance of MRC system 1-1 (Config. 1) in Fig. 6.4 is presented. The other units are operating under normal

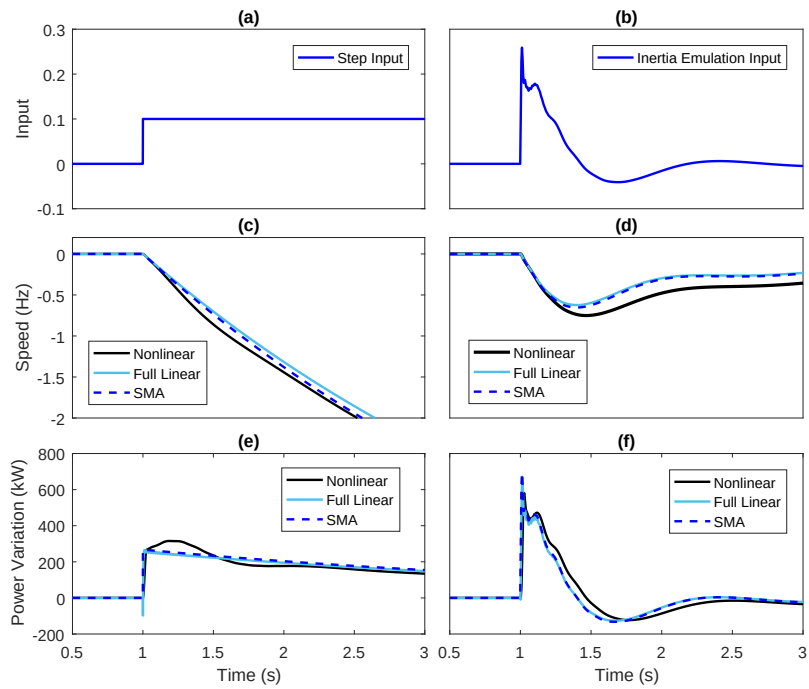

Figure 6.5: Response comparison of nonlinear, linear and SMA-based first-order WTG model under step input and inertia emulation input. (a) Step input. (b) Inertia emulation input via washout filter. (c) WTG speed variation under step input. (d) WTG speed variation under inertia emulation input. (e) WTG active power variation under step input. (f) WTG active power variation under inertia emulation input.

condition. The disturbance is a step load change at Bus 18. The inertia constant of DSG 1 is one second, i.e., $H_{D,1} = 1$ s, and the desired inertia set in the reference model is three seconds, i.e., $\hat{H}_1 = 3$ s. By solving the LMIs, the feedback law is obtained and shown in (6.21)

$$K_{\text{mrc}} = \begin{bmatrix} 158.37 & -5.28 & -3.18 & -68.81 & -157.02 & 5.79 & 3.50 \end{bmatrix} \tag{6.21}$$

The closed-loop frequency response is shown in Fig. 6.6 (a). As shown, the two second synthetic inertia constant is precisely emulated. The responses under conventional inertia emulation realized by a washout filter $K_{\text{ie}}s/(0.01s + 1)$ with different gains, $K_{\text{ie}} = 0.03$ and $K_{\text{ie}} = 0.1$, are shown in Fig. 6.6 (a) for comparison. As K_w increases the response approaches the one under the MRC-based inertia emulation. However, a trial and error procedure is needed to reach the desired performance. The power output from WTG 1 is shown in Fig. 6.6 (c). Note that there exists weak inertial response (Gray curve) for a

field-oriented controlled DFIG-based WTG even without a supportive controller, and this response is sensitive to the rotor current-controller bandwidth [68].

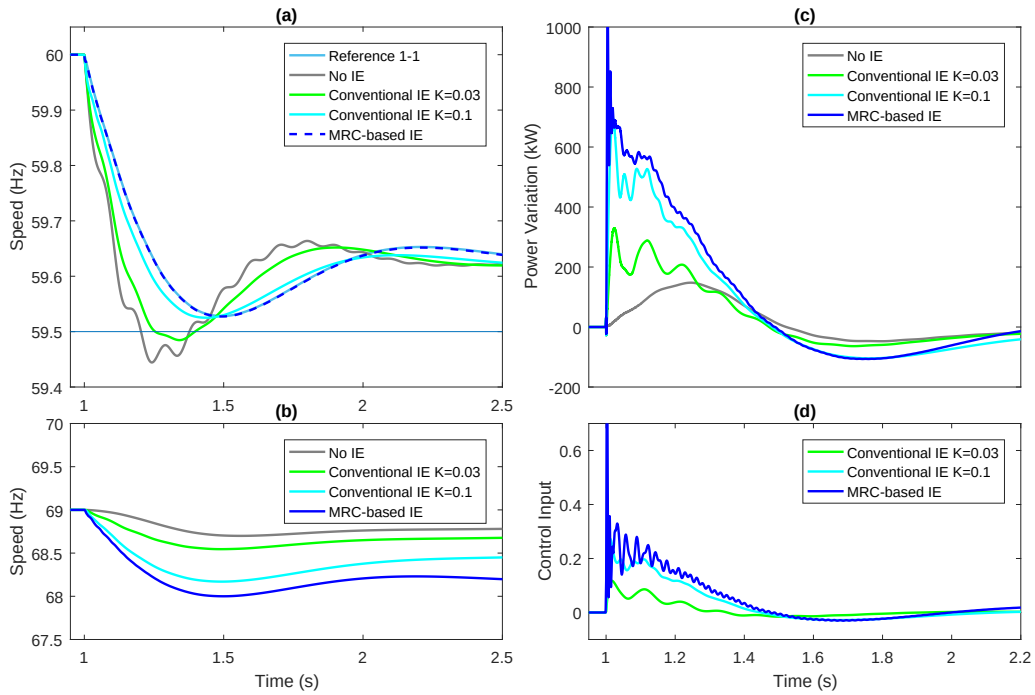

Figure 6.6: Performance under conventional and MRC-based inertia emulation with Config. 1. (a) Speeds of DSG and reference model. (b) WTG speed. (c) WTG active power variation. (d) Control input.

6.3.2 Parameter Uncertainty

Besides compensation of model reduction errors, parameter uncertainty of the physical plants is considered. As model (2.5) dominates the frequency characteristics, it is sufficient to consider only the parameter uncertainty within this model. Assume the inertia $H_{D,1}$, time constant τ_d and τ_{sm} of DSG 1 are the uncertain parameters and belong to the range defined as: $H_{D,1} \in \overline{H}_{D,1}[1-\theta_1^1, 1+\theta_1^2]$, $\tau_d \in \overline{\tau}_d[1-\theta_2^1, 1+\theta_2^2]$, $\tau_{sm} \in \overline{\tau}_{sm}[1-\theta_3^1, 1+\theta_3^2]$ where $\overline{H}_{D,1} = 1$ s, $\overline{\tau}_d = 0.2$ s and $\overline{\tau}_{sm} = 0.1$ s are the mean values. The reference model parameters are set according to the mean values as: $\hat{H}_1 = \overline{H}_{D,1} + 2$ s, $\hat{\tau}_d = \overline{\tau}_d$, $\hat{\tau}_{sm} = \overline{\tau}_{sm}$. Let $\theta_1^1 = \theta_1^2 = 50\%$ and $\theta_2^1 = \theta_2^2 = \theta_3^1 = \theta_3^2 = 90\%$ when using Corollary 6.2 to design the controller. Consider two sets of parameters as: $\{\text{Scenario 1} \mid H_{D,1} = 0.5 \text{ s}, \tau_d = 0.38 \text{ s}, \tau_{sm} = 0.19 \text{ s}\}$ and $\{\text{Scenario 2} \mid H_{D,1} = 1.5 \text{ s}, \tau_d = 0.11 \text{ s}, \tau_{sm} = 0.05 \text{ s}\}$. The response of Scenario 1 under

the controller designed using Theorem 6.1 is shown in Fig. 6.7 (a), while the response under controller designed using Corollary 6.2 is shown in Fig. 6.7 (c). As illustrated, by using Corollary 6.2 the tracking performance is not impaired by parameter uncertainty. A similar comparison of Scenario 2 is shown in Fig. 6.7 (b) and Fig. 6.7 (d), respectively.

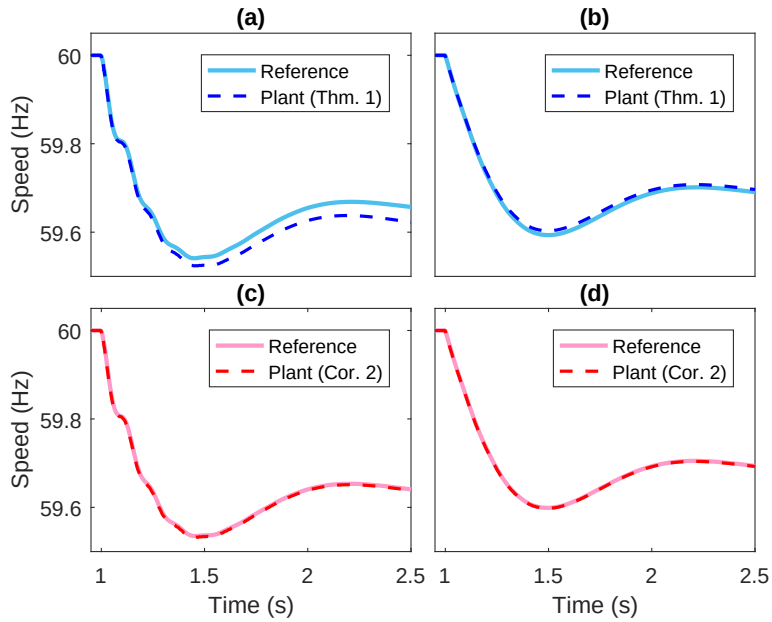

Figure 6.7: MRC-based IE under parameter uncertainty. (a) Response under parameters of Scenario 1 using Thm. 6.1. (b) Response under parameters of Scenario 2 using Thm. 6.1. (c) Response under parameters of Scenario 1 using Cor. 6.2. (d) Response under parameters of Scenario 2 using Cor. 6.2.

6.3.3 Wind Speed Dependent Control Reconfiguration and Inertia Scheduling

Due to the varying loading condition, different DSGs are needed to switch on and off from time to time. So, the control system should have multiple configurations and switch between them based on different scenarios. Three configurations are illustrated in Fig. 6.4. The rectangles represent the MRC system formed by the included diesel and wind units. Meanwhile, it is also desired to have the frequency deviation in all scenarios within 0.5 Hz under a worst-case disturbance so as to minimize the possibility of unnecessary load shedding [85]. This objective in most cases is difficult to achieve but can be easily realized

with the proposed control. As physical plants are guaranteed to track the reference model, the dynamics of the wind diesel mixed network are equivalent to the systems shown in Fig. 6.8. Thus, verifying the frequency response and scheduling the inertia of the reference model will be sufficient to achieve the objective.

Under Condition A, one MRC system can be activated with larger synthetic inertia or two MRC systems can be activated separately (Config. 2). The first case has been presented in section 6.3.1. In the latter case, each of the reference models only needs to emulate one more second inertia so that the frequency response under the given disturbance is above 59.5 Hz as shown in Fig. 6.9 (a). The corresponding power output is given in Fig. 6.9 (c). Under Condition B, DSG 2 is chosen to be shut down and the total inertia decreases. The droop of DSG 1 is adjusted so that the steady-state response meets the requirement. The inertia of Reference Model 1 is set to be four seconds. The variational active power for three seconds inertia cannot be achieved by one wind unit. Two different configurations are constructed by incorporating different numbers of WTGs as shown in Fig. 6.4 (Config. 3 and 4). Their frequency responses and power variations are illustrated in Fig. 6.10 (a) and Fig. 6.10 (c), respectively. The capability of coordinating multiple DERs to provide the required inertia under the proposed control is verified. The scheduled parameters are presented in Table 6.1.

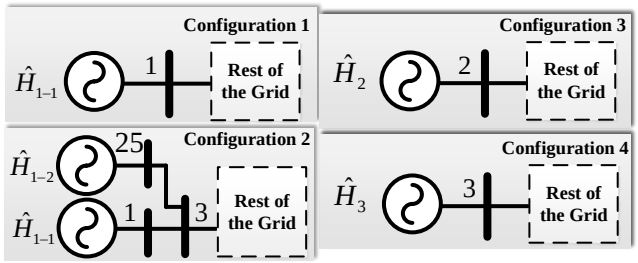

Figure 6.8: Equivalent networks under different configurations.

Since the control design is based on the terminal condition (6.7), any incident that violates (6.7) impairs the function of MRC. One factor is to choose POMs correctly for varying configurations. Buses 1 and 25 are the POMs for MRC system 1-1 and 1-2, respectively. Bus 2 and 3 are the POMs for MRC system 2 and 3. If the POMs are not chosen correctly, then the terminal power flow condition will not be satisfied and the plants are not able to

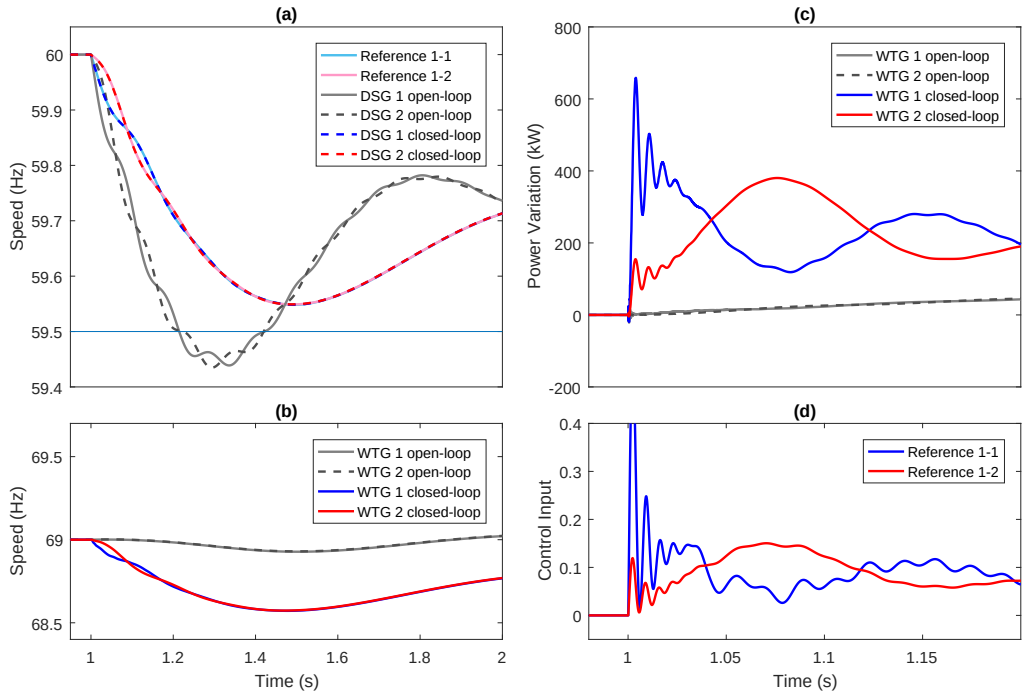

Figure 6.9: Performance under conventional and MRC-based inertia emulation with Config. 2. (a) Speeds of DSG and reference model. (b) WTG speed. (c) WTG active power variation. (d) Control input.

track the reference models. In Configurations 3 and 4, any disturbances between the POMs and generators will change (6.7) and impact the function of MRC systems. Now, consider the same disturbance applied to Bus 18 and Bus 3 at 1 s and 1.3 s, respectively. Since the terminal condition for Config. 4 cannot hold, the plant fails to track the reference as shown in Fig. 6.11, while Config. 3 is functioning well. Fortunately, these scenarios are rare due to the radial structure of the distribution systems.

6.3.4 Discussion

Compared with the traditional inertia emulation approach, two more states from the DSG (speed of DSG and frequency in the microgrid are assumed to be equivalent) are measured. Although it requires inter-device communication, the value of this is two-fold. First, the states provide information on the amount of inertial response generated by the DSG such that the WTG can make up the rest to meet the requirement. Second, it provides robustness against parameter uncertainty of DSGs.

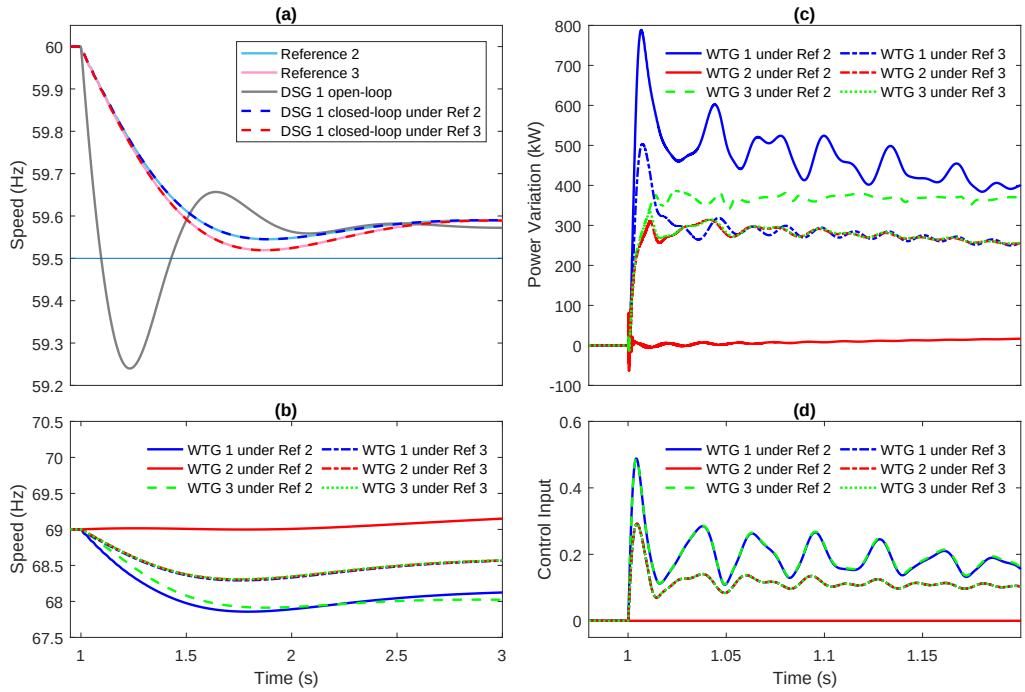

Figure 6.10: Performance under conventional and MRC-based inertia emulation with Config. 3 and 4. (a) Speeds of DSG and reference model. (b) WTG speed. (c) WTG active power variation. (d) Control input.

Note that even though type-3 WTGs are chosen to represent the renewable energy sources, the proposed method is applicable on other types of WTGs as well as other converter-interfaced sources, including but not limited to battery storages photovoltaics and microturbines. One disadvantage is that at each time when the control is activated, the WTG operates off of MPPT, which in long term will decrease the averaged efficiency of energy harvesting.

6.4 Experimental Implementation in HTB

The proposed control is implemented on an aggregated WECC system modeled in the HTB of CURENT. The emulated WECC model has been already introduced in chapter 4.4.3. It is a four-area system with a multi-terminal HVDC overlay, the one-line diagram of which is shown in Fig. 6.12. Area 2 is selected to configure the MRC structure. The experimental implementation is illustrated in Fig. 6.13. The necessary states of BC Hydro (Bus 1), Grand

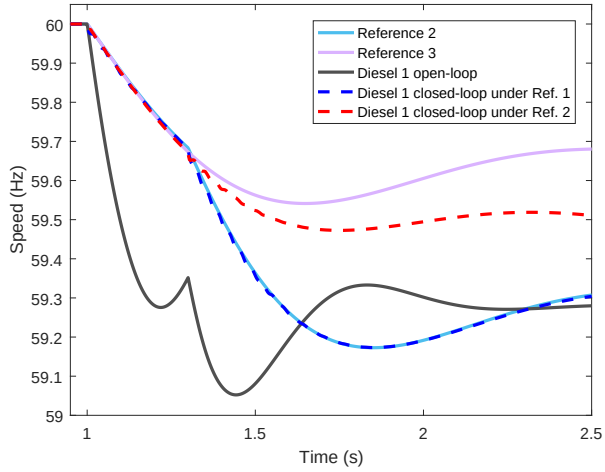

Figure 6.11: DSG speed under MRC-based inertia emulation with two successive disturbances at Bus 18 and Bus 3. Tracking in Config. 4 fails since disturbance at Bus 3 violates the terminal condition.

Coulee (Bus 2) and their terminal active power at POM are measured and passed to the area controller in Labview. The deviation of these variables are calculated by subtracting the current measurement from their averaged values over a period, which is considered as the operating point. The terminal active power deviation is sent to the reference model solved by an ODE solver. The obtained states together with the measured states are sent to the feedback gain to obtain the enhanced inertia emulation signal for near-ideal inertial response.

In the experimental demonstration, a 0.3 p.u generation loss is applied at Colstrip (Bus 3). The tracking performance of MRC is shown in 6.14. The frequency response at BC Hydro (Bus 1) (red full line) tracks the frequency of the reference model (blue dash line) driven by the active power variation at POM. The frequency responses with and without MRC-based IE are compared in Fig. 6.15.

6.5 Summary

In this chapter, a novel MRC-based synthetic inertia emulation strategy is proposed. The reference model is designed to have a similar structure to the frequency response model with desired inertia. Through active power measurement and state feedback, the WTG generates

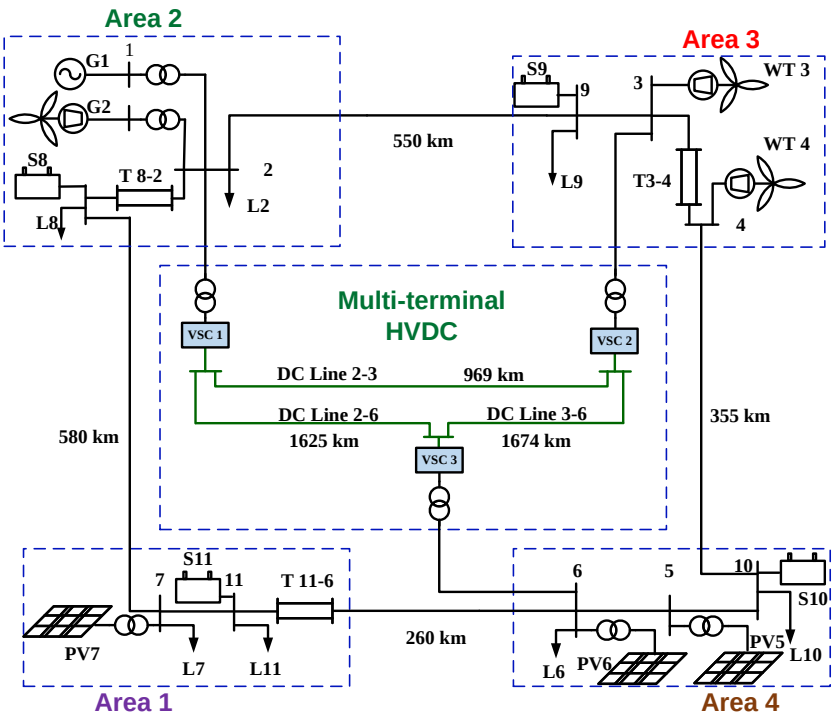

Figure 6.12: One-line diagram of the aggregated WECC system modeled in the HTB of CURENT, which is a four-area system with a multi-terminal HVDC overlay.

additional active power to guarantee that the diesel generator speed follows the frequency from the reference model. This novel control strategy ensures precise emulated inertia by the WTG as opposed to the trial and error procedure of conventional methods. This controller is also robust against parameter uncertainty. By guaranteeing performance, safety bounds can be easily derived based on the reference model under the worst-case scenario. Then, adequate response can be achieved by scheduling the inertia according to the operating point of the network. Moreover, the capability of coordinating multiple WTGs to provide required inertia under the proposed control is verified. Finally, the proposed controller is implemented in real-time experimental environment in HTB at CURENT.

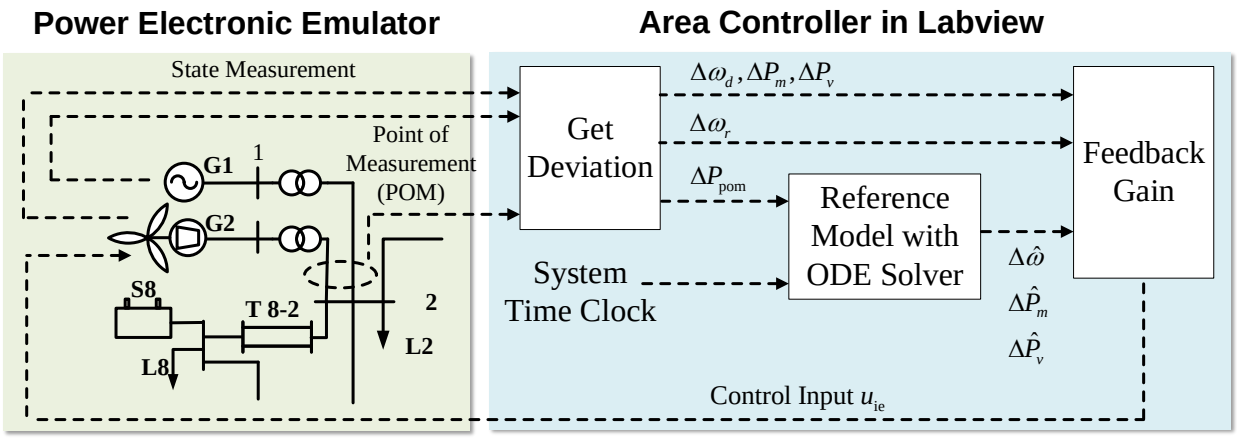

Figure 6.13: Experimental implementation of MRC-based inertia emulation in HTB at CURENT.

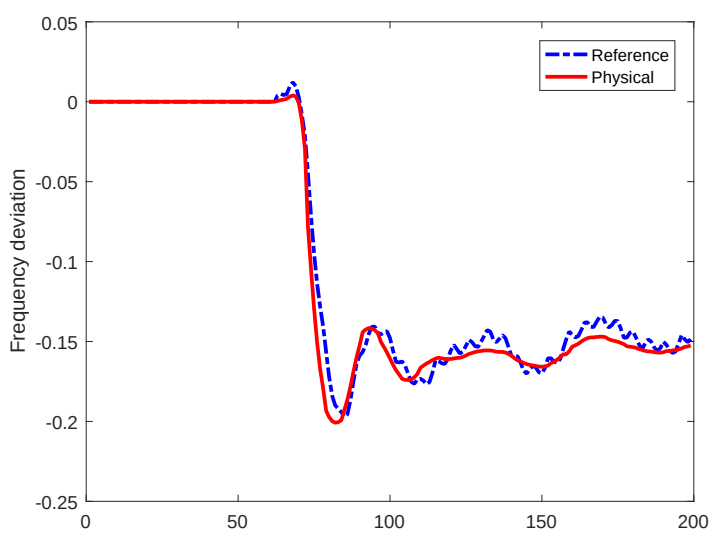

Figure 6.14: MRC tracking performance of frequency response at BC Hydro (Bus 1).

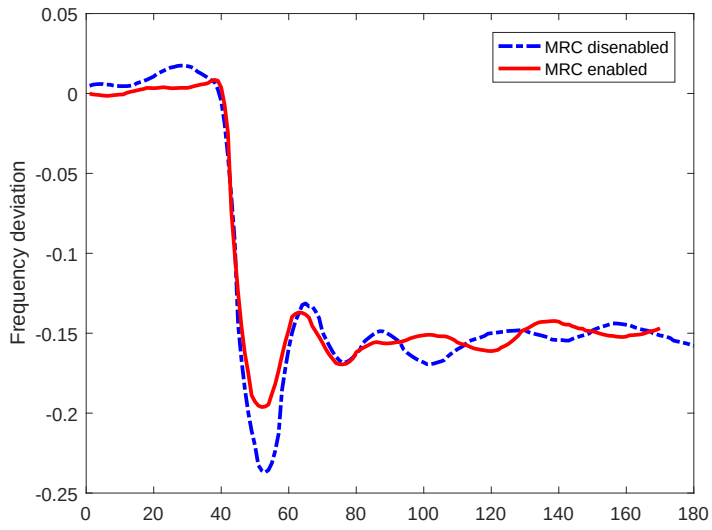

Figure 6.15: Frequency response at BC Hydro (Bus 1) with and without MRC-based IE.

Chapter 7

Conclusions and Future Works

7.1 Conclusions

Nowadays, the increasing penetration of renewable sources has degraded the grid frequency response. It is because most renewable sources are converter-interfaced and do not inherently respond to frequency events. On the other hand, the potentials of such highly controllable converters are far from fully developed under current control approaches. With properly designed controls the CISs can not only eliminate the negative impacts on the grid, but also provide performance guarantees, which becomes increasingly important for power system operations under high renewable penetration.

Power system models for frequency control problem is derived in Chapter 2. To study the systemic frequency response, the SFR model is discussed in Section 2.1. As a widely-deployed CIS, the WTG is selected as a representative actuator. The WTG model is given in Section 2.2, where the SMA-based model reduction technique is introduced to derive a first-order model representing the supportive power variations associated with the supplementary signals. Combining the interaction between these two models leads to the ASFR model in Section 2.3. The emulated inertial and primary control responses are approximately evaluated as the corresponding coefficients in the swing equation. As a result, the equivalent inertia and load-damping constants become time-varying.

The set theoretic framework for formal safety verification is reviewed in Chapter 3. Three different approaches for verification is described in Section 3.1. Among these approaches,

the passivity-based method is employed. The different computation methods for positivity are described and compared in Section 3.2.

The hybrid controller synthesis of the WTG is studied in Chapter 4. In Section 4.1, a new concept, ROS, is proposed, and the safe switching principle is interpreted. Also the largest ROS is explained in the sense of the backward reachable sets. In Section 4.2, two methods are proposed to estimate the largest ROS. First, on the barrier certificate theory an iterative algorithm is proposed. Second, a mathematically intuitive formulation in the functional space is established, which can provide convergent information. Geometry interpretation of this formulation is given. Two approaches are verified on a simple case and compared with other formal verification methods. Pros and cons of the two approaches are discussed. In Section 4.3, the critical switching instants or the largest equivalent deadbands for adequate frequency response are obtained through the study of the ASFR model of a single-area system. The simulation results indicate that the estimated largest ROSs are not conservative. In addition, a safe switching window is discovered and a safe speed recovery strategy is proposed, which successfully ensures the safety of the second frequency dip due to the WTG speed recovery. In Section 4.4, an adaptive SSC is proposed with a two-loop configuration, where the supervisor is scheduled with respect to the renewable penetration level. The proposed controller can not only ensure the adequacy of the diesel generator speed in a single-machine three-phase nonlinear microgrid, but also guarantee that of the COI frequency in IEEE 39-bus system with varying renewable penetration. The scheduling of the SSC under different penetration level is demonstrated as well. Finally, the controller is experimentally implemented on an aggregated WECC system emulated by the HTB at CURENT. In this case, the wide-area measurement signals are used to calculate the COI frequency, which is the input of the state observer. The experiment was performed under the real measurement and data acquisition. The adequacy of the COI frequency was ensured by the proposed SSC.

A NOC-based control synthesis methodology is proposed in Chapter 4 that enables the realization of the TLSs. The preliminaries on TLSs as well as its conversion to programming methods are described in Section 5.1. The control diagram for control synthesis is introduced in Section 5.2. The controller schedules ahead a series of Boolean control signals to synthesize

the GS mode of WTGs by solving the NOC problem, where the frequency response predicted by the AFR model satisfies the defined specifications under a worst-case contingency. The proposed control is verified on the full nonlinear model in Simulink. A robust factor is introduced to compensate the model reduction error such that the nonlinear response satisfies the TLS.

A novel MRC-based synthetic inertia emulation strategy is proposed in Chapter 6. The motivation and problem is stated in Section 6.1. The control configuration is introduced in Section 6.2. The reference model is designed to have a similar structure to the frequency response model with desired inertia. Through active power measurement and state feedback, the WTG generates additional active power to guarantee that the diesel generator speed follows the frequency from the reference model. This novel control strategy ensures precise emulated inertia by the WTG as opposed to the trial and error procedure of conventional methods. This controller is also robust against parameter uncertainty. By guaranteeing performance, safety bounds can be easily derived based on the reference model under the worst-case scenario. Then, adequate response can be achieved by scheduling the inertia according to the operating point of the network. The control method is verified on 33-node based microgrid in Section 6.3. The capability of coordinating multiple WTGs to provide required inertia under the proposed control is illustrated. Finally, the proposed controller is implemented in real-time experimental environment in HTB at CURENT in Section 6.4.

7.2 Future Work

Based on the work to date, continuing research in the following direction is needed.

- Alternative computation techniques for positivity certificate are pressing. The computational complex of SOS decomposition is increasing exponentially with the system dimension. To scale the technique to higher dimensional systems, alternative representations should be applied.

- Heuristic encoding algorithms for TLSs are required. Model checking using the approach presented in this dissertation will result in large-scale mixed integer

programming. It takes considerable time to solve the problem and prevents its online deployment. The heuristic algorithm in [92] will be investigated so that the controller can run in real time.

- Schedulable and decentralized MRC-based IE configuration will be designed. MRC-based IE is configured in a centralized fashion. The advantages of it is the capability to compensate parameter uncertainty of the synchronous generators. The cost is the communication and its induced delay. A decentralized MRC-based IE only within the WTG will be designed as well as a scheduling algorithm to ensure systemic performance.

Bibliography

[1] Abad, G., Lopez, J., Rodríguez, M., Marroyo, L., and Iwanski, G. (2011). *Doubly fed induction machine: modeling and control for wind energy generation*. John Wiley & Sons, Hoboken, New Jersey. 17, 18

[2] Al-Digs, A., Dhople, S. V., and Chen, Y. C. (2016). Estimating feasible nodal power injections in distribution networks. *2016 IEEE Power and Energy Society Innovative Smart Grid Technologies Conference, ISGT 2016*. 32

[3] Althoff, M. (2014). Formal and compositional analysis of power systems using reachable sets. *IEEE Transactions on Power Systems*, 29(5):2270–2280. 32

[4] Althoff, M. and Krogh, B. H. (2014). Reachability analysis of non-linear systems differential-algebraic systems. *IEEE Transactions on Automatic Control*, 59(2):371–383. 32, 33

[5] Anderson, P. M. and Mirheydar, M. (1990). A low-order system frequency response model. *IEEE Transactions on Power Systems*, 5(3):720–729. 15, 64

[6] Apostolopoulou, D., Sauer, P. W., and Domínguez-García, A. D. (2016). Balancing authority area model and its application to the design of adaptive agc systems. *IEEE Transactions on Power Systems*, 31(5):3756–3764. 16

[7] ApS, M. (2015). *The MOSEK optimization toolbox for MATLAB manual. Version 7.1 (Revision 28)*. 37, 62, 89

[8] Baran, M. E. and Wu, F. F. (1989). Network reconfiguration in distribution systems for loss reduction and load balancing. *IEEE Transactions on Power Systems*, 4(2):1401–1407. 106

[9] Ben Sassi, M. A., Sankaranarayanan, S., Chen, X., and Ábrahám, E. (2016). Linear relaxations of polynomial positivity for polynomial Lyapunov function synthesis. *IMA Journal of Mathematical Control and Information*, 33(3):723–756. 35, 37, 38

[10] Bhana, R. and Overbye, T. J. (2016a). The commitment of interruptible load to ensure adequate system primary frequency response. *IEEE Transactions on Power Systems*, 31(3):2055–2063. 3, 6

[11] Bhana, R. and Overbye, T. J. (2016b). The commitment of interruptible load to ensure adequate system primary frequency response. *IEEE Transactions on Power Systems*, 31(3):2055–2063. 79

[12] Bhana, R. and Overbye, T. J. (2016c). The commitment of interruptible load to ensure adequate system primary frequency response. *IEEE Transactions on Power Systems*, 31(3):2055–2063. 31

[13] Bhatia, A. and Frazzoli, E. (2004). Incremental search methods for reachability analysis of continuous and hybrid systems. *Hybrid Systems: Computation and Control*, 0208891:142–156. 31

[14] Brisebois, J. and Aubut, N. (2011). Wind farm inertia emulation to fulfill hydro-qubec's specific need. In *Proceeding of IEEE Power and Energy Society General Meeting (PESMG)*, pages 1–7. 6

[15] Chen, Y. C. (2012). A Method to Study the Effect of Renewable Resource Variability on Power System Dynamics. *IEEE Transactions on Power Systems*, 27(4):1978–1989. 32

[16] Chvez, H. and Hezamsadeh, M. R. (2013). The need for market-based provision of inertia and frequency response to integrate wind power in nordel. Technical report, Royal Institute of Technology, Stockholm, Sweden. 4, 6

[17] Clark, K., Miller, N. W., and Sanchez-Gasca, J. J. (2010). Modeling of GE wind turbine-generators for grid studies, version 4.5. Technical report, General Electric International, Inc., Schenectady, NY, USA. xv, 5, 65

[18] Conroy, J. F. and Watson, R. (2008). Frequency response capability of full converter wind turbine generators in comparison to conventional generation. *IEEE Transactions on Power Systems*, 23(2):649–656. 5

[19] D'Arco, S. and Suul, J. A. (2014). Equivalence of virtual synchronous machines and frequency-droops for converter-based microgrids. *IEEE Transactions on Smart Grid*, 5(1):394–395. 95

[20] Donzé, A., Raman, V., Frehse, G., and Althoff, M. (2015). Blustl: Controller synthesis from signal temporal logic specifications. In *ARCH@ CPSWeek*, pages 160–168. 82, 89

[21] El-Guindy, A., Chen, Y. C., and Althoff, M. (2017). Compositional transient stability analysis of power systems via the computation of reachable sets. *Proceedings of the American Control Conference*, pages 2536–2543. 32

[22] El-Guindy, A., Han, D., and Althoff, M. (2016). Formal Analysis of Drum-Boiler Units to Maximize the Load-Following Capabilities of Power Plants. *IEEE Transactions on Power Systems*, 31(6):4691–4702. 32

[23] Feng, L., Liu, W., Mei, S., Wei, W., and Yao, Y. (2017). Eso-based inertia emulation and rotor speed recovery for dfigs. *IEEE Transactions on Energy Conversion*, PP(99):1–1. 5

[24] Gao, H. and Chen, T. (2008). Network-based $\mathcal{H}_\infty$ output tracking control. *IEEE Transactions on Automatic Control*, 53(3):655–667. 95, 103, 104

[25] Gevorgian, V., Zhang, Y., and Ela, E. (2015). Investigating the impacts of wind generation participation in interconnection frequency response. *IEEE transactions on Sustainable Energy*, 6(3):1004–1012. 16, 64

[26] Girard, A. (2005). Reachability of uncertain linear systems using zonotopes. *Hybrid systems: computation and control*, pages 291–305. 32

[27] Girard, A. and Pappas, G. J. (2007). Approximate bisimulation relations for constrained linear systems. *Automatica*, 43(8):1307–1317. 31

[28] Guernic, C. L. (2009). Reachability Analysis of Hybrid Systems with Linear Continuous Dynamics. 31

[29] Handelman, D. (1988). Representing polynomials by positive linear functions on compact convex polyhedra. *Pacific Journal of Mathematics*. 38

[30] He, W., Yuan, X., and Hu, J. (2017). Inertia provision and estimation of PLL-based dfig wind turbines. *IEEE Transactions on Power Systems*, 32(1):510–521. 5

[31] Henrion, D. and Korda, M. (2014). Convex computation of the region of attraction of polynomial control systems. *IEEE Transactions on Automatic Control*, 59(2):297–312. 33, 47

[32] Hiskens, I. A. (2012). Dynamics of type-3 wind turbine generator models. *IEEE Transactions on Power Systems*, 27(1):465–474. xv, 65

[33] Hooker, J. N. and Fedjki, C. (1990). Branch-and-cut solution of inference problems in propositional logic. *Annals of Mathematics and Artificial Intelligence*, 1(1-4):123–139. 81

[34] Hope, E. M., Jiang, X., and Dominguez-Garcia, A. D. (2011). A Reachability-Based Method for Large-Signal Behavior Verification of DC-DC Converters. *IEEE Transactions on Circuits and Systems I: Regular Papers*, 58(12):2944–2955. 32

[35] Hu, J., Wang, S., Tang, W., and Xiong, X. (2016). Full-capacity wind turbine with inertial support by adjusting phase-locked loop response. *IET Renewable Power Generation*, 11(1):44–53. 5

[36] Jiang, X., Chen, and Dominguez-Garcia, A. D. (2013). A set-theoretic framework to assess the impact of variable generation on the power flow. *IEEE Transactions on Power Systems*, 28(2):855–867. 32

[37] Jiang, X. and Dominguez-Garcia, A. D. (2014). A zonotope-based method for capturing the effect of variable generation on the power flow. In *2014 North American Power Symposium (NAPS)*, pages 1–6. IEEE. 32

[38] Jin, L., Kumar, R., and Elia, N. (2010). Reachability analysis based transient stability design in power systems. *International Journal of Electrical Power & Energy Systems*, 32(7):782–787. 33

[39] Junyent-Ferré, A., Pipelzadeh, Y., and Green, T. C. (2015). Blending HVDC-link energy storage and offshore wind turbine inertia for fast frequency response. *IEEE Transactions on Sustainable Energy*, 6(3):1059–1066. 5

[40] Kamyar, R. and Peet, M. M. (2015). Polynomial optimization with applications to stability analysis and control-alternatives to sum of squares. *Discrete and Continuous Dynamical Systems-Series B*, 20(8):2383–2417. 37

[41] Karaman, S. and Frazzoli, E. (2008a). Complex mission optimization for multiple-UAVs using linear temporal logic. In *Proceedings of American Control Conference (ACC)*, pages 2003–2009. 82

[42] Karaman, S. and Frazzoli, E. (2008b). Linear temporal logic vehicle routing with applications to multi-UAV mission planning. *International Journal of Robust and Nonlinear Control*, 21(12):557–569. 82

[43] Karaman, S. and Frazzoli, E. (2008c). Vehicle routing problem with metric temporal logic specifications. In *Proceedings of IEEE Conference on Decision and Control (CDC)*, pages 3953–3958. 82

[44] Karaman, S., Sanfelice, R. G., and Frazzoli, E. (2008a). Optimal control of mixed logical dynamical systems with linear temporal logic specifications. In *Proceedings of IEEE Conference on Decision and Control (CDC)*, pages 2117–2122, Cancun, Mexico. 80

[45] Karaman, S., Sanfelice, R. G., and Frazzoli, E. (2008b). Optimal control of mixed logical dynamical systems with linear temporal logic specifications. In *Proceedings of IEEE Conference on Decision and Control (CDC)*, pages 2117–2122. 82

[46] Kayikçi, M. and Milanovic, J. V. (2009). Dynamic contribution of DFIG-based wind plants to system frequency disturbances. *IEEE Transactions on Power Systems*, 24(2):859–867. 5, 95

[47] Keung, P.-K., Li, P., Banakar, H., and Ooi, B. T. (2009). Kinetic energy of wind-turbine generators for system frequency support. *IEEE Transactions on Power Systems*, 24(1):279–287. 5, 95

[48] Korda, M., Henrion, D., and Jones, C. N. (2013). Inner approximations of the region of attraction for polynomial dynamical systems. In *IFAC Proceedings Volumes (IFAC-PapersOnline)*, volume 9, pages 534–539. 47

[49] Kurzhanskiy, A. A. and Varaiya, P. (2007). Ellipsoidal techniques for reachability analysis of discrete-time linear systems. *IEEE Transactions on Automatic Control*, 52(1):26–38. 32

[50] Lalor, G., Mullane, A., and O'Malley, M. (2005a). Frequency control and wind turbine technologies. *IEEE Transactions on Power Systems*, 20(4):1905–1913. 5

[51] Lalor, G., Mullane, A., and O'Malley, M. (2005b). Frequency control and wind turbine technologies. *IEEE Transactions on Power Systems*, 20(4):1905–1913. 19

[52] Laurijsse, M., Wisniewski, R., and Weiland, S. (2014). Optimizing safety supervisors for wind turbines using barrier certificates. *IFAC Proceedings Volumes*. 35

[53] Li, Y., Xu, Z., and Wong, K. P. (2017). Advanced control strategies of PMSG-based wind turbines for system inertia support. *IEEE Transactions on Power Systems*, 32(4):3027–3037. 5

[54] Löfberg, J. (2004). YALMIP: A toolbox for modeling and optimization in MATLAB. In *Proc. IEEE CCA/ISIC/CACSD Conf.*, Taipei, Taiwan. 37, 62, 89

[55] Löfberg, J. (2009). Pre-and post-processing sum-of-squares programs in practice. *IEEE Transactions on Automatic Control*, 54(5):1007–1011. 37

[56] Ma, Y., Cao, W., Yang, L., Wang, F., and Tolbert, L. M. (2017a). Virtual synchronous generator control of full converter wind turbines with short term energy storage. *IEEE Transactions on Industrial Electronics*, PP(99):1–1. 2

[57] Ma, Y., Cao, W., Yang, L., Wang, F. F., and Tolbert, L. M. (2017b). Virtual Synchronous Generator Control of Full Converter Wind Turbines with Short-Term Energy Storage. *IEEE Transactions on Industrial Electronics*, 64(11):8821–8831. xvi, 74, 75

[58] Ma, Y., Yang, L., Wang, J., and Wang, F. (2014). Emulating full-converter wind turbine by a single converter in a multiple converter based emulation system. In *Proceeding of*

IEEE Applied Power Electronics Conference and Exposition (APEC), pages 3042–3047. 3

[59] Mackin, P., Daschmans, R., Williams, B., Haney, B., Hunt, R., and Ellis, J. (2010). Dynamic simulations studies of the frequency response of the three u.s. interconnections with increased wind generation. Technical Report LBNL-4146E, Lawrence Berkely National Laboratory, Berkeley, CA, USA. 16, 64

[60] Maidens, J. N., Kaynama, S., Mitchell, I. M., Oishi, M. M., and Dumont, G. A. (2013). Lagrangian methods for approximating the viability kernel in high-dimensional systems. *Automatica*, 49(7):2017–2029. 31

[61] Maram, M. D. and Amjady, N. (2014). Event-based remedial action scheme against super-component contingencies to avert frequency and voltage instabilities. *IET Generation, Transmission & Distribution*, 8(9):1591–1603. 85

[62] Mauricio, J. M., Marano, A., Gómez-Expósito, A., and Ramos, J. L. M. (2009). Frequency regulation contribution through variable-speed wind energy conversion systems. *IEEE Transactions on Power Systems*, 24(1):173–180. 95

[63] Miller, N. W., Shao, M., Pajic, S., and D'Aquila, R. (2013). Eastern frequency response study. Technical Report NREL/SR-5500-58077, National Renewable Energy Laboratory, Denver, CO, USA. 15, 16, 64

[64] Miller, N. W., Shao, M., and Venkataraman, S. (2011). California ISO CAISO frequency response study. Technical report, General Electric International, Inc., Schenectady, NY, USA. 15, 16, 64

[65] Morren, J., De Haan, S. W., Kling, W. L., and Ferreira, J. (2006). Wind turbines emulating inertia and supporting primary frequency control. *IEEE Transactions on Power Systems*, 21(1):433–434. 2, 5, 95

[66] Mullane, A. and O'Malley (2005a). The inertial response of induction-machine-based wind turbines. *IEEE Transactions on Power Systems*, 20(3):1496–1503. 19

[67] Mullane, A. and O'Malley, M. (2005b). The inertial response of induction-machine-based wind turbines. *IEEE Transactions on Power Systems*, 20(3):1496–1503. 3

[68] Mullane, A. and O'Malley, M. (2005c). The inertial response of induction-machine-based wind turbines. *IEEE Transactions on Power Systems*, 20(3):1496–1503. 108

[69] NERC (2012). Frequency response initiative report. Technical report, North American Electric Reliability Council, Atlanta, GA, USA. 53

[70] NERC (2016). Balancing and frequency control. Technical report, North American Electric Reliability Council, Princeton, NJ, USA. 4

[71] Ni, N. M., McCalley, J. D., Vittal, V., and Tayyib, T. (2002). Online Risk-Based Security Assessment. *IEEE Power Engineering Review*, 22(11):59. 31

[72] Nimpitiwan, N., Heydt, G. T., Ayyanar, R., and Suryanarayanan, S. (2007). Fault current contribution from synchronous machine and inverter based distributed generators. *IEEE Transactions on Power Systems*, 22(1):634–641. 106

[73] Papachristodoulou, A., Anderson, J., Valmorbida, G., Prajna, S., Seiler, P., and Parrilo, P. A. (2013). *SOSTOOLS: Sum of squares optimization toolbox for MATLAB*. http://arxiv.org/abs/1310.4716. Available from http://www.eng.ox.ac.uk/control/sostools, http://www.cds.caltech.edu/sostools and http://www.mit.edu/˜parrilo/sostools. 37

[74] Parrilo, P. a. (2000). Structured Semidefinite Programs and Semialgebraic Geometry Methods in Robustness and Optimization. 2000:117. 35, 36

[75] Parrilo, P. A. (2003). Semidefinite programming relaxations for semialgebraic problems. *Mathematical Programming, Series B*, 96(2):293–320. 36

[76] Pedersen, R., Sloth, C., and Wisniewski, R. (2016). Verification of power grid voltage constraint satisfaction A barrier certificate approach. In *2016 European Control Conference (ECC)*, pages 447–452. IEEE. 35

[77] Pico, H. N. and Aliprantis, D. C. (2016). Voltage Ride-Through Capability Verification of DFIG-Based Wind Turbines Using Reachability Analysis. *IEEE Transactions on Energy Conversion*, 31(4):1387–1398. 32

[78] Pico, H. N. V. and Aliprantis, D. C. (2014). Voltage ride-through capability verification of wind turbines with fully-rated converters using reachability analysis. *IEEE Transactions on Energy Conversion*, 29(2):392–405. 32

[79] Pico, H. N. V., Aliprantis, D. C., and Hoff, E. C. (2013). Reachability Analysis of Power System Frequency Dynamics with New High-Capacity HVAC and HVDC Transmission Lines Zonotope-Based Reachability Analysis of Linear. In *2013 IREP Symposium-Bulk Power System Dynamics and Control -IX (IREP)*, number 1, pages 1–9. 32

[80] Powers, V. (2011). Positive polynomials and sums of squares: Theory and practice. *Real Algebraic Geometry*, page 77. 36

[81] PowerTech (2012a). *DSATools User-Defined Model (UDM) User Manual.* Powertech Labs Inc., Surrey, BC, Canada. xv, 65, 66, 68, 142

[82] PowerTech (2012b). *Transient Security Assessment Tool (TSAT) User Manual.* Powertech Labs Inc., Surrey, BC, Canada. 14, 65, 68

[83] Prajna, S., Jadbabaie, A., and Pappas, G. J. (2007). A Framework for Worst-Case and Stochastic Safety Verification Using Barrier Certificates. *IEEE Transactions on Automatic Control*, 52(8):1415–1428. 34, 37, 39

[84] Pulendran, S. and Tate, J. E. (2017a). Energy storage system control for prevention of transient under-frequency load shedding. *IEEE Transactions on Smart Grid*, 8(2):927–936. 4, 6

[85] Pulendran, S. and Tate, J. E. (2017b). Energy storage system control for prevention of transient under-frequency load shedding. *IEEE Transactions on Smart Grid*, 8(2):927–936. 109

[86] Pulgar-Painemal, H. A. (2010). *Wind Farm Model for Power System Stability Analysis*. PhD thesis, Univ. of Illinois at Urbana-Champaign, Champaign, IL. 18, 20, 23, 68, 106, 140

[87] Raman, V., Donze, A., Maasoumy, M., Murray, R. M., Sangiovanni-Vincentelli, A., and Seshia, S. A. (2014). Model predictive control with signal temporal logic specifications. In *Proc. IEEE Conf. Decis. Control (CDC)*, pages 81–87. 81, 82

[88] Raoufat, M. E., Tomsovic, K., and Djouadi, S. M. (2017). Dynamic control allocation for damping of inter-area oscillations. 68

[89] Reznick, B. (2000). Some concrete aspects of hilbert's 17th problem. *Contemporary mathematics*, 253:251–272. 35, 36

[90] Rocabert, J., Luna, A., Blaabjerg, F., and Rodriguez, P. (2012). Control of power converters in AC microgrids. *IEEE Transactions on Power Electronics*, 27(11):4734–4749. 2

[91] Saadat, H. (1999). *Power system analysis*, page 530. McGraw-Hill New York, New York, NY. 14

[92] Saha, S. and Julius, A. A. (2016). An MILP approach for real-time optimal controller synthesis with Metric Temporal Logic specifications. In *Proceedings of American Control Conference (ACC)*, volume 2016-July, pages 1105–1110. 81, 120

[93] Sauer, P. W. and Pai, M. (1997). *Power system dynamics and stability*. Prentice Hall, New Jersey, USA. 106

[94] Sauer, P. W. and Pai, M. A. (1998). *Power system stability and control*, pages 23–87. Prentice Hall, Upper Saddle River, NJ. 14

[95] Shu, Y. H., Chi, K. L., and Wu, F. F. (2012). Electric springsa new smart grid technology. *IEEE Transactions on Smart Grid*, 3(3):1552–1561. 2

[96] Siemens (2013). *PSS/E 33.5 Model Library*. Siemens Industry, Inc., Schenectady, NY, USA. 68

[97] Slootweg, J., de Haan, S., Polinder, H., and Kling, W. (2003). General model for representing variable speed wind turbines in power system dynamics simulations. *IEEE Transactions on Power Systems*, 18(1):144–151. 65

[98] Sloth, C., Pappas, G. J., and Wisniewski, R. (2012a). Compositional safety analysis using barrier certificates. *Proceedings of the 15th ACM international conference on Hybrid Systems: Computation and Control - HSCC '12*, page 15. 35

[99] Sloth, C., Wisniewski, R., and Pappas, G. J. (2012b). On the existence of compositional barrier certificates. *Proceedings of the IEEE Conference on Decision and Control*, pages 4580–4585. 35

[100] Susuki, Y. and Hikihara, T. (2007). Predicting voltage instability of power system via hybrid system reachability analysis. In *Proceedings of American Control Conference (ACC)*, pages 4166–4171. 33

[101] Susuki, Y., Koo, T. J., Ebina, H., Yamazaki, T., Ochi, T., Uemura, T., and Hikihara, T. (2012). A hybrid system approach to the analysis and design of power grid dynamic performance. *Proceedings of the IEEE*, 100(1):225–239. 33

[102] Tang, W., Hu, J., Chang, Y., Yuan, X., and Liu, F. (2018). Modeling of DFIG-based WT for system transient response analysis in rotor speed control timescale. *IEEE Transactions on Power Systems*. early access. 97

[103] Tayab, U. B., Roslan, M. A. B., Hwai, L. J., and Kashif, M. (2017). A review of droop control techniques for microgrid. *Renewable & Sustainable Energy Reviews*, 76:717–727. 2

[104] Terzija, V. V. (2006). Adaptive underfrequency load shedding based on the magnitude of the disturbance estimation. *IEEE Transactions on Power Systems*, 21(3):1260–1266. 15

[105] Tomlin, C., Mitchell, I., Bayen, A., and Oishi, M. (2003). Computational Techniques for the Verification and Control of Hybrid Systems. *IEEE Proceedings*, 91(7):1–29. 33

[106] Ulbig, A., Borsche, T. S., and Andersson, G. (2014). Impact of low rotational inertia on power system stability and operation. *IFAC Proceedings Volumes*, 47(3):7290–7297. 4, 6, 60

[107] Ullah, N. R., Thiringer, T., and Karlsson, D. (2008). Temporary primary frequency control support by variable speed wind turbinespotential and applications. *IEEE Transactions on Power Systems*, 23(2):601–612. 139

[108] Uriarte, F. M., Smith, C., VanBroekhoven, S., and Hebner, R. E. (2015a). Microgrid ramp rates and the inertial stability margin. *IEEE Transactions on Power Systems*, 30(6):3209–3216. 6

[109] Uriarte, F. M., Smith, C., Vanbroekhoven, S., and Hebner, R. E. (2015b). Microgrid Ramp Rates and the Inertial Stability Margin. *IEEE Transactions on Power Systems*, 30(6):3209–3216. 41

[110] Wang, B., Zhang, Y., Sun, K., and Tomsovic, K. (2018). Quantifying the synthetic inertia and load-damping effect of a converter-interfaced power source. In *Proceedings of IEEE International Energy Conference (ENERGYCON)*, pages 1–5, Limassol, Cyprus. 13, 95

[111] Weaver, W. W. and Krein, P. T. (2009). Optimal geometric control of power buffers. *IEEE Transactions on Power Electronics*, 24(5):1248–1258. 2

[112] Wilches-Bernal, F., Chow, J. H., and Sanchez-Gasca, J. J. (2016). A fundamental study of applying wind turbines for power system frequency control. *IEEE Transactions on Power Systems*, 31(2):1496–1505. 41

[113] Winn, A. and Julius, A. A. (2015). Safety controller synthesis using human generated trajectories. *IEEE Transactions on Automatic Control*, 60(6):1597–1610. 81

[114] Wisniewski, R., Svenstrup, M., Pedersen, A. S., and Steiniche, C. S. (2013). Certificate for Safe Emergency Shutdown of Wind Turbines *. In *American Control Conference (ACC)*, pages 3673–3678, Washington DC. 35

[115] Xu, T., Jang, W., and Overbye, T. (2016). Application of set-theoretic method to assess the locational impacts of virtual inertia services on the primary frequency responses. In *2016 IEEE Power and Energy Conference at Illinois, PECI 2016*. 32

[116] Xu, Z., Julius, A., and Chow, J. H. (2017). Energy storage controller synthesis for power systems with temporal logic specifications. *IEEE Systems Journal*. early access. 79, 81

[117] Xyngi, I. and Popov, M. (2010). Smart protection in dutch medium voltage distributed generation systems. In *Proceeding of IEEE Power and Energy Society Innovative Smart Grid Technologies Conference (ISGT)*, pages 1–8, Gothenberg, Sweden. 79

[118] Yang, Z., Huang, C., Chen, X., Lin, W., and Liu, Z. (2016). A linear programming relaxation based approach for generating barrier certificates of hybrid systems. In *Lecture Notes in Computer Science (including subseries Lecture Notes in Artificial Intelligence and Lecture Notes in Bioinformatics)*, volume 9995 LNCS, pages 721–738. Springer, Cham. 39

[119] Yu Christine Chen, Xichen Jiang, and Dominguez-Garcia, A. D. (2011). Impact of power generation uncertainty on power system static performance. In *2011 North American Power Symposium*, pages 1–5. IEEE. 32

[120] Zhang, L., Harnefors, L., and Nee, H. P. (2011). Power-synchronization control of grid-connected voltage-source converters. *IEEE Transactions on Power Systems*, 25(2):809–820. 5, 7

[121] Zhang, W., Cantarellas, A. M., Rocabert, J., Luna, A., and Rodriguez, P. (2016). Synchronous power controller with flexible droop characteristics for renewable power generation systems. *IEEE Transactions on Sustainable Energy*, 7(4):1572–1582. 5, 6, 7

[122] Zhang, Y., Melin, A., Djouadi, S., and Olama, M. (2017a). Performance guaranteed inertia emulation for diesel-wind system feed microgrid via model reference control. In *Proceeding of IEEE Power and Energy Society Innovative Smart Grid Technologies Conference (ISGT)*, pages 1–5. 62, 64, 96

[123] Zhang, Y., Melin, A., Djouadi, S. M., Olama, M. M., and Tomsovic, K. (2018a). Provision for guaranteed inertial response in diesel-wind systems via model reference control. *IEEE Transactions on Power Systems*. in press. 96

[124] Zhang, Y., Olama, M., Melin, A., Xue, Y., Djouadi, S., and Tomsovic, K. (2018b). Synthesizing distributed energy resources in microgrids with temporal logic specifications. In *Proceedings of IEEE International Symposium on Power Electronics for Distributed Generation Systems (PEDG)*, pages 1–7, Charlotte, USA. 80

[125] Zhang, Y., Raoufat, M. E., Tomsovic, K., and Djouadi, S. M. (2018c). Set theory-based safety supervisory control for wind turbines to ensure adequate frequency response. *IEEE Transactions on Power Systems*. in press. 40

[126] Zhang, Y., Tomsovic, K., Djouadi, S., and Pulgar-Painemal, H. (2017b). Hybrid controller for wind turbine generators to ensure adequate frequency response in power networks. *IEEE Journal on Emerging & Selected Topics in Circuits & Systems*, 7(3):359–370. 7, 13, 40, 43, 66, 79, 95

Appendices

A Summary of Parameters

A.1 SFR Model Parameters

$H_c = 4$ [s], $\overline{\tau}_{\text{ch}} = 0.3$ [s], $\overline{\tau}_{\text{gv}} = 0.1$ [s], $\overline{D} = 1$, $\overline{R} = 0.05$.

A.2 33-Node Based Microgrid

Variables are in per unit unless specified otherwise.

Base: $S_{\text{base}} = 1.1$ MVA, $V_{\text{base}} = 575$ V, $\overline{\omega} = 377$ rad/s.

Operating condition: Wind speed: 10 m/s. $P_g = 0.8$, $Q_g = 0$, $v_{ds} = 0$, $v_{qs} = 1$.

Equilibrium point of state variables: $\psi_{qs} = 0.002$, $\psi_{ds} = 1.015$, $\psi_{qr} = 0.223$, $\psi_{dr} = 1.041$, $\omega_r = 1.150$, $x_1 = -0.641$, $x_2 = 0.261$, $x_3 = 0.011$, $x_4 = 0.005$.

Equilibrium point of algebraic variables: $i_{qs} = -0.631$, $i_{ds}0.084$, $i_{qr} = 0.671$, $i_{dr} = 0.261$, $v_{qr} = -0.196$, $v_{dr} = 0.048$.

Reduced-order model: $A_{\text{rd}} = -0.27$, $B_{\text{rd}} = 2.52$, $C_{\text{rd}} = 0.26$, $D_{\text{rd}} = -2.41$.

Diesel generator: Rated power: 2 [MW], $H_{D,i} = 1$ [s], $\tau_{d,i} = 0.2$ [s], $\tau_{sm,i} = 0.1$ [s] for $i = 1, 2$.

Wind turbine generator: Rated power: 1 [MW], $H_{T,i} = 4$ [s], $K^T_{P,i} = 2$, $K^T_{I,i} = 0.1$, $K^Q_{P,i} = 1$, $K^Q_{I,i} = 5$, $K^C_{P,i} = 0.6$, $K^C_{I,i} = 8$ for $i = 1, 2, 3$.

MRC system: $\hat{\tau}_d = 0.2$ [s], $\hat{\tau}_{sm} = 0.1$ [s], $\hat{D} = 0$, $\eta_m = 0.05$ [s], $\kappa = 0.1$ [s].

B Wind Turbine Generators

B.1 Fifth-Order DFIM-Based WTG Data Set

Variables are in per unit unless specified otherwise.

- Rotor-side controller

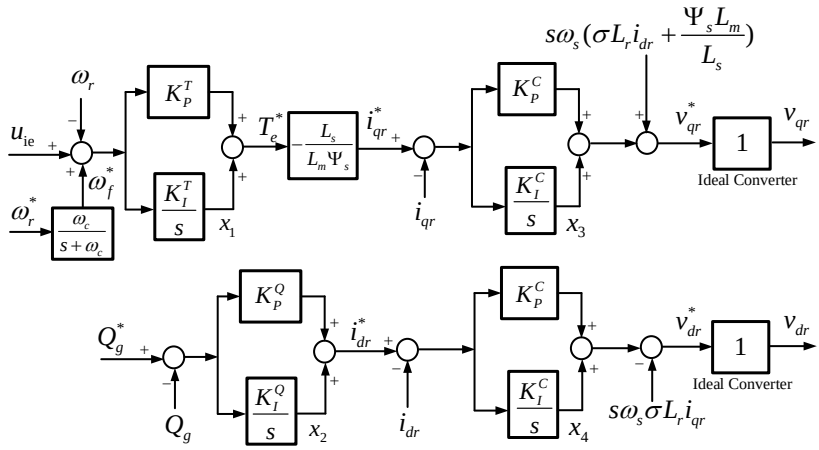

- Differential equations

$$\dot{\psi}_{qs} = \overline{\omega}(v_{qs} - R_s i_{qs} - \omega_s \psi_{ds}) \tag{1}$$

$$\dot{\psi}_{ds} = \overline{\omega}(v_{ds} - R_s i_{ds} + \omega_s \psi_{qs}) \tag{2}$$

$$\dot{\psi}_{qr} = \overline{\omega}[v_{qr} - R_r i_{qr} - (\omega_s - \omega_r)\psi_{dr}] \tag{3}$$

$$\dot{\psi}_{dr} = \overline{\omega}[v_{dr} - R_r i_{dr} + (\omega_s - \omega_r)\psi_{qr}] \tag{4}$$

$$\dot{\omega}_r = 1/(2H_T)(T_m - T_e) \tag{5}$$

$$\dot{\omega}_f^* = \omega_c(\omega_r^* - \omega_f^*) \tag{6}$$

$$\dot{x}_1 = K_I^T(\omega_f^* - \omega_r + u_{\text{ie}}) \tag{7}$$

$$\dot{x}_2 = K_I^Q(Q_g^* - Q_g) \tag{8}$$

$$\dot{x}_3 = K_I^C(i_{qr}^* - i_{qr}) \tag{9}$$

$$\dot{x}_4 = K_I^C(i_{dr}^* - i_{dr}) \tag{10}$$

The terms ψ_{ds}, ψ_{qs} (ψ_{dr},ψ_{qr}) are the stator (rotor) flux linkages [p.u.] in d, q-axis, respectively. v_{ds}, v_{qs} (v_{dr}, v_{qr}) are the instantaneous stator (rotor) voltages [p.u.] in d, q-axis, respectively. i_{ds}, i_{qs} (i_{dr}, i_{qr}) are the instantaneous stator (rotor) currents [p.u.] in d, q-axis, respectively. R_s and R_r are the stator and rotor resistance [p.u.], respectively. H_T is the combined inertia constant [s] of the wind turbine and induction machine. ω_s and $\overline{\omega}$ are the synchronous angular speed [p.u.] and speed base of the WTG [rad/s], respectively.

- Algebraic equations

$$0 = -\psi_{qs} + L_s i_{qs} + L_m i_{qr} \tag{11}$$

$$0 = -\psi_{ds} + L_s i_{ds} + L_m i_{dr} \tag{12}$$

$$0 = -\psi_{qr} + L_r i_{qr} + L_m i_{qs} \tag{13}$$

$$0 = -\psi_{dr} + L_r i_{dr} + L_m i_{ds} \tag{14}$$

$$0 = P_g + (v_{ds} i_{ds} + v_{qs} i_{qs}) + (v_{dr} i_{dr} + v_{qr} i_{qr}) \tag{15}$$

$$0 = Q_g + (v_{qs} i_{ds} - v_{ds} i_{qs}) + (v_{qr} i_{dr} - v_{dr} i_{qr}) \tag{16}$$

$$\begin{aligned} 0 = -v_{qr} + x_3 + K_P^C (i_{qr}^* - i_{qr}) \\ + (\omega_s - \omega_r)(\sigma L_r i_{dr} + \frac{\Psi_s L_m}{L_s}) \end{aligned} \tag{17}$$

$$\begin{aligned} 0 = -v_{dr} + x_4 + K_P^C (i_{dr}^* - i_{dr}) \\ - (\omega_s - \omega_r) \sigma L_r i_{qr} \end{aligned} \tag{18}$$

where L_{ls} and L_{lr} are the stator and rotor leakage inductance [p.u.], L_m is the mutual inductance [p.u.]., and $L_s = L_{ls} + L_m$, $L_r = L_{lr} + L_m$.

- Electromagnetic torque

$$T_e = \frac{L_m}{L_s}(\psi_{qs} i_{dr} - \psi_{ds} i_{qr}) \tag{19}$$

- Optimal speed [107]

$$\omega_r^* = -0.67 \times (\eta P_g)^2 + 1.42 \times (\eta P_g) + 0.51 \tag{20}$$

for $\omega_r \in [0.8, 1.2]$. The variable η is the ratio between the base of the induction machine and wind turbine.

- Converter regulation model $v_{qr} = v_{qr}^*$ and $v_{dr} = v_{dr}^*$

- Other intermediate variables

$$\begin{aligned} i_{qr}^* &= \frac{-L_s T_e^*}{L_m \Psi_s} = \frac{-L_s}{L_m \Psi_s}[x_1 + K_P^T(\omega_f^* - \omega_r + u_{\text{ie}})] \\ i_{dr}^* &= x_2 + K_P^Q(Q_g^* - Q_g) \end{aligned} \tag{21}$$

- Wind turbine parameters
  $p = 4$, $\rho = 1.225$ [kg/m^3], $R_t = 38.5$ [m], $k = 1/45$, $\theta_t = 0$ [degree], $\overline{P}_M = 1.5$ [MVA].

- Induction machine and control parameters
  $L_m = 2.9$, $L_{ls} = 0.18$, $L_{lr} = 0.16$, $R_s = 0.023$, $R_r = 0.016$, $\overline{S}_E = 1.1$ [MVA], $V_{\text{base}} = 575$ [V], $\overline{\omega} = 377$ [rad/s], $H_{T,i} = 4$ [s], $K_P^T = 2$, $K_I^T = 0.1$, $K_P^Q = 1$, $K_I^Q = 5$, $K_P^C = 0.6$, $K_I^C = 8$

- Base: $S_{\text{base}} = 1.1$ [MVA], .

- Operating condition: Wind speed: 10 m/s. $P_g = 0.8$, $Q_g = 0$, $v_{ds} = 0$, $v_{qs} = 1$.

- Equilibrium point of state variables: $\psi_{qs} = 0.002$, $\psi_{ds} = 1.015$, $\psi_{qr} = 0.223$, $\psi_{dr} = 1.041$, $\omega_r = 1.150$, $x_1 = -0.641$, $x_2 = 0.261$, $x_3 = 0.011$, $x_4 = 0.005$.

- Equilibrium point of algebraic variables: $i_{qs} = -0.631$, $i_{ds} = 0.084$, $i_{qr} = 0.671$, $i_{dr} = 0.261$, $v_{qr} = -0.196$, $v_{dr} = 0.048$.

B.2 Third-Order DFIM-Based WTG Data Set

This two-axis WTG model and is adopted from [86]. Variables are in per unit unless specified otherwise.

- Differential equations

$$
\begin{aligned}
\dot{E}'_{qD} =& -\frac{1}{T'_0}[E'_{qD} + (X_s - X'_s)I_{ds}] + \omega_s \frac{X_m}{X_r} V_{dr} - (\omega_s - \omega_r)E'_{dD} \\
\dot{E}'_{dD} =& -\frac{1}{T'_0}[E'_{dD} + (X_s - X'_s)I_{qs}] + \omega_s \frac{X_m}{X_r} V_{qr} - (\omega_s - \omega_r)E'_{qD} \\
\dot{\omega}_r =& \frac{\omega_s}{2H_D}(T_m - E'_{dD}I_{ds} - E'_{qD}I_{qs}) \\
\dot{x}_1 =& K_{I1}(P_{\text{ref}} - P_{\text{gen}}) \\
\dot{x}_2 =& K_{I2}[K_{P1}(P_{\text{ref}} - P_{\text{gen}}) + x_1 - I_{qr}] \\
\dot{x}_3 =& K_{I3}(Q_{\text{ref}} - Q_{\text{gen}}) \\
\dot{x}_4 =& K_{I4}[K_{P3}(Q_{\text{ref}} - Q_{\text{gen}}) + x_3 - I_{dr}]
\end{aligned}
\tag{22}
$$

where E'_{dD}, E'_{qD} and ω_r are the d and q axis voltage and rotor speed of the WTG, respectively. x_1 to x_4 are proportional-integral regulator induced states. And $P_{\text{ref}} = C_{\text{opt}}\omega_r^3$, $Q_{\text{ref}} = Q_{\text{set}}$, $T'_0 = \frac{X_r}{\omega_s R_r}$ and $X'_s = X_s - \frac{X_m^2}{X_r}$.

- Algebraic equations

$$
\begin{aligned}
0 =& K_{P2}[K_{P1}(P_{\text{ref}} - P_{\text{gen}}) + x_1 - I_{qr}] + x_2 - V_{qr} \\
0 =& K_{P4}[K_{P3}(Q_{\text{ref}} - Q_{\text{gen}}) + x_3 - I_{dr}] + x_4 - V_{dr} \\
0 =& -P_{\text{gen}} + E'_{dD}I_{ds} + E'_{qD}I_{qs} - R_s(I_{ds}^2 + I_{qs}^2) - (V_{qr}I_{qr} + V_{dr}I_{dr}) \\
0 =& -Q_{\text{gen}} + E'_{qD}I_{ds} + E'_{dD}I_{qs} - X'_s(I_{ds}^2 + I_{qs}^2) \\
0 =& -I_{dr} + \frac{E'_{qD}}{X_m} + \frac{X_m}{X_r}I_{ds} \\
0 =& -I_{qr} - \frac{E'_{dD}}{X_m} + \frac{X_m}{X_r}I_{qs}
\end{aligned}
\tag{23}
$$

where V_{dr}, V_{qr}, I_{dr}, I_{qr} are rotor d q axis voltage and current, respectively. V_{ds}, V_{qs}, I_{ds}, I_{qs} are stator d q axis voltage and current. P_{gen} and Q_{gen} are WTG active and reactive power output. V_D and θ_D are voltage magnitude and angle of the bus which WTGs are connected to.

- Network algebraic equations

$$E'_{qD} - jE'_{dD} = (R_s + jX'_s)(I_{qs} - jI_{ds}) + V_D \tag{24a}$$

$$V_D e^{j\theta_D} = jX_t(I_{qs} - jI_{ds} - I_{GC})e^{j\theta_D} + Ve^{j\theta} \tag{24b}$$

where

$$I_{GC} = \frac{V_{dr}I_{qr} + V_{dr}I_{dr}}{V_D}$$

- Wind turbine parameters

  $p = 4$, $\rho = 1.225$ [kg/m^3], $R_t = 38.5$ [m], $k = 1/45$, $\theta_t = 0$ [degree], $\overline{P}_M = 1.5$ [MVA].

- Induction machine and control parameters

  $X_m = 3.5092$, $X_s = 3.5547$, $X_r = 3.5859$, $R_s = 0.01015$, $R_r = 0.0088$, $H_D = 4$ [s], $\overline{S}_E = 1000$ [MVA], $K_{P1} = K_{P2} = K_{P3} = K_{P4} = 1$, $K_{I1} = K_{I2} = K_{I3} = K_{I4} = 5$, $C_{\text{opt}} = 3.2397 \times 10^{-7}$ [s^3/Hz^3].

- Network parameters and operating condition

  $X_t = 0.07$, $\bar{V} = 1$, $\bar{\theta} = 0$ [rad], $\bar{\theta}_t = 0$ [rad], $\bar{v}_{\text{wind}} = 12$ [m/s], $\bar{\omega}_r = 72$ [Hz], $\bar{P}_{\text{gen}} = 0.3$, $N_t = 200$, $\bar{Q}_{\text{set}} = 0$, $S_b = 1000$ [MVA].

B.3 WECC Generic WTG Data Set

- Wind turbine parameters

  Given in Page 213-214 in [81].

- WTG parameters

  T_{sp}=60 [s], T_{pc}=0.05 [s], K_{ptrq}=3, K_{itrq}=0.6

- Linearized WTG at the rated operating condition

  Model for SSC design

$$\begin{aligned} \begin{bmatrix} \Delta\dot{\overline{x}} \\ \Delta\dot{\overline{\omega}}_r \end{bmatrix} &= \begin{bmatrix} 0 & 0.600 \\ -0.125 & -0.435 \end{bmatrix} \begin{bmatrix} \Delta\overline{x} \\ \Delta\overline{\omega}_r \end{bmatrix} + \begin{bmatrix} 0.600 \\ -0.375 \end{bmatrix} \overline{u}_{\mathrm{ie}} \\ \Delta\overline{P}_G &= \begin{bmatrix} 1.056 & 3.644 \end{bmatrix} \begin{bmatrix} \Delta\overline{x} \\ \Delta\overline{\omega}_r \end{bmatrix} + 3.167\overline{u}_{\mathrm{ie}} \end{aligned} \tag{25}$$

  Model for observer

$$\begin{aligned} \begin{bmatrix} \Delta\dot{\overline{x}} \\ \Delta\dot{\overline{\omega}}_r \end{bmatrix} &= \begin{bmatrix} 0 & 0.600 \\ -0.125 & -0.435 \end{bmatrix} \begin{bmatrix} \Delta\overline{x} \\ \Delta\overline{\omega}_r \end{bmatrix} + \begin{bmatrix} 0.600 \\ -0.375 \end{bmatrix} \overline{u}_{\mathrm{ie}} \\ \overline{y} &= \begin{bmatrix} 1 & 0 \\ 0 & 1 \end{bmatrix} \begin{bmatrix} \Delta\overline{x} \\ \Delta\overline{\omega}_r \end{bmatrix} \end{aligned} \tag{26}$$

Vita

Yichen Zhang received B.S. degree from Northwestern Polytechnical University, Xi'an, China, in 2010, and M.S. degree from Xi'an Jiaotong University, Xi'an, China, in 2012. Now he is currently pursuing the Ph.D. degree in the Department of Electrical Engineering and Computer Science (EECS) at the University of Tennessee, Knoxville, TN, USA.

His main research interests include power system dynamics and control, power electronics applications in power systems, renewable energy, formal verifications of cyber-physical systems and their applications into power systems.